A MEASUREMENT OF $Z(\nu\bar{\nu})\gamma$ CROSS SECTION AND LIMITS ON ANOMALOUS TRIPLE GAUGE COUPLINGS AT $\sqrt{s} = 7$ TeV USING CMS

by

SHRUTI SHRESTHA

M.S., Tribhuvan University, Nepal, 2001

AN ABSTRACT OF A DISSERTATION

submitted in partial fulfillment of the
requirements for the degree

DOCTOR OF PHILOSOPHY

Department of Physics
College of Art and Sciences

KANSAS STATE UNIVERSITY
Manhattan, Kansas
2013

Abstract

In this thesis, the first measurement of $Z\gamma \to \nu\bar{\nu}\gamma$ cross section in pp collisions at $\sqrt{s} =$ 7 TeV has been done using data collected by the CMS detector. The measured cross section is 21.3 $\pm$ 4.2 (stat.) $\pm$ 4.3 (syst.) $\pm$ 0.5 (lumi.) fb. This measurement is based on the observations of events with missing transverse energy in excess of 130 GeV and photon in the rapidity range $|\eta| < 1.44$ of transverse momentum in excess of 145 GeV in a data sample corresponding to an integrated luminosity of 5 fb^{-1}. This measured cross section is in good agreement with the theoretical prediction of 21.9 $\pm$ 1.1 fb from BAUR. Further, neutral triple gauge couplings involving Z bosons and photons have been studied. No evidence for the presence of such couplings is observed and is in agreement with the predictions of the standard model. We set the most stringent limits to date on these triple gauge couplings.

A MEASUREMENT OF $Z(\nu\bar{\nu})\gamma$ CROSS SECTION AND LIMITS ON ANOMALOUS TRIPLE GAUGE COUPLINGS AT $\sqrt{s} = 7$ TeV USING CMS

by

SHRUTI SHRESTHA

M.S., Tribhuvan University, Nepal, 2001

A DISSERTATION

submitted in partial fulfillment of the
requirements for the degree

DOCTOR OF PHILOSOPHY

Department of Physics
College of Art and Sciences

KANSAS STATE UNIVERSITY
Manhattan, Kansas
2013

Approved by:

Major Professor
Professor Yurii Maravin

Copyright

Abstract

In this thesis, the first measurement of $Z\gamma \to \nu\bar{\nu}\gamma$ cross section in pp collisions at $\sqrt{s} =$ 7 TeV has been done using data collected by the CMS detector. The measured cross section is 21.3 $\pm$ 4.2 (stat.) $\pm$ 4.3 (syst.) $\pm$ 0.5 (lumi.) fb. This measurement is based on the observations of events with missing transverse energy in excess of 130 GeV and photon in the rapidity range $|\eta| < 1.44$ of transverse momentum in excess of 145 GeV in a data sample corresponding to an integrated luminosity of 5 fb^{-1}. This measured cross section is in good agreement with the theoretical prediction of 21.9 $\pm$ 1.1 fb from BAUR. Further, neutral triple gauge couplings involving Z bosons and photons have been studied. No evidence for the presence of such couplings is observed and is in agreement with the predictions of the standard model. We set the most stringent limits to date on these triple gauge couplings.

Table of Contents

List of Figures

List of Tables

Acknowledgments

I would like to thank my advisor Professor Yurii Maravin and postdoctoral associate Dr. Jordan Damgov for their guidance in helping me investigate photon and missing energy analysis. I would also like to extend my gratitude to UCDAVIS group (Professor Mani Tripathi, Tia Miceli, Carley Kopecky, Sushil Chauhan) as well as Professor Andrew Askew from Florida State University for providing me the feedback and invaluable suggestions. Lastly, I would like to thank to Professor Alice Bean, Professor Tim Bolton, Professor Andrew Ivanov, Professor Sung Won Lee, and Dr. Jose Lazoflores for their encouargement.

Chapter 1

Introduction

> Any new fact or insight that I may have found has not seemed to me as a "discovery" of mine, but rather something that has always been there and that I had chanced to pick up. - P. V. Subrahmanyan Chandrasekhar

The standard model (SM) of elementary particle physics provides a remarkably accurate picture of the fundamental structure of matter. It was introduced by Sheldon Glashow [1], Steven Weinberg [2] and Abdus Salam [3] in the early 1970's and has accomplished a wide range of experimental results. The SM describes the fundamental interaction of particles based on relativistic quantum field theory. In the SM, there are 12 spin- $\frac{1}{2}$ fermions and 4 spin-1 gauge bosons which are the fundamental force carriers. Three of four fundamental forces (i.e., electromagnetism, the weak interaction, and the strong interactions) are included in the SM. The fourth fundamental force (i.e., the effect of gravitational force) is dominant at macroscopic distances, but is negligible on the microscopic scale, and therefore, not incorporated in the SM. The 12 fermions are divided into 6 quarks (u, d, s, c, b, t) and 6 leptons $(e, \mu, \tau, \nu_e, \nu_\mu, \nu_\tau)$, all of which possess charge conjugate states called anti-particles. The quarks are classified into three generations with very different mass scales ranging from a few MeV for up and down quarks to about 171 GeV for the top quark. Even though both quarks and leptons are subjected to the weak force, only quarks and charge leptons (e, μ, τ) undergo electromagnetic interactions. A major achievement of the SM is the

unification of the electromagnetic and the weak force into an electroweak force embedded in the theory of Quantum Electrodynamics (QED). Therein, a photon is considered as a gauge boson of the electromagnetism and the mediators of the weak interactions are the W and Z bosons. The SM predicted seven (c, b, t, ν_t, W, Z, gluon) out of 16 particles before they were experimentally observed. Furthermore, the SM has predicted the finding of the Higgs boson. The Higgs boson plays a major role in the SM as its observation would be a major step towards to understand how elementary particles acquire mass and give rise to the phenomenon of electroweak symmetry breaking.

The Large Hadron Collider (LHC) is a proton-proton collider which has been constructed to operate at a center-of-mass energy of $\sqrt{s} = 14$ TeV. On March 30, 2010, the first collisions were performed at a center-of-mass energy of $\sqrt{s} = 7$ TeV. In the beginning of 2012, it was operated with center-of-mass energy of $\sqrt{s} = 8$ TeV to collect a significant amount of data (15 fb^{-1}) which is 3 times more than that of 2011. After upgrade of the detector, collision energy will be further increased. The one of the major goals of the LHC is to discover the origin of the electroweak symmetry breaking and a recent discovery of a new boson at 125 GeV might be the first step in this endeavor. Indeed, more data will be required to measure the properties such as of the newly discovered boson couplings to fermions, its spin, and parity before the particle could be confirmed as the Higgs boson.

Despite the great success of the SM in describing various aspects of the physics within its domain, it is still an incomplete theory. There are several fundamental questions that are yet to be answered. For example, the nature of dark matter (DM) or the origin of the asymmetry between matter and antimatter in the universe. To provide explanations for these questions, many promising theories extending the SM have been developed. Supersymmetry theories and theories with extra-dimensions are the most prominent examples. Many of these theories predict physics, which should be accessible at the energy scale available at the LHC. Our hope is that the upcoming data from the LHC will ultimately help us answer many of these questions.

This thesis contains the study of the associated production of photons and Z bosons, aimed to test the electroweak sector of the SM and possibility to find the hints for physics beyond the SM. The outline of this thesis is as follows: Chapter 1 is a brief overview of the SM and its limitations. This is followed by introduction to LHC and the CMS detector which includes the main sub-detectors and their corresponding performances in Chapter 2. An introduction on photon reconstruction has also been mentioned in this Chapter. The Chapter 3 is about the theory of $Z\gamma$ production where it includes general overview of the SM, the electroweak theory and the anomalous Triple Gauge Couplings (TGCs). It also includes a summary of the results from the previous studies of D0, CDF, CMS, and from the recent studies of ATLAS collaboration. Chapter 4 covers the data sets, trigger, and event selection. Chapter 5 is dedicated to the description of the method to measure $\mathrm{Z}\gamma \to \nu\bar{\nu}\gamma$ cross section in at $\sqrt{s} = 7$ TeV, while measurement of aTGC are given in Chapter 6. I summarize the results in Chapter 7. The final signature of photon and missing transverse energy can be used in search for DM pair-production and search for large extra dimension, the former one is explained briefly in the Appendix section. The various parts of this thesis have been presented at conferences and under publication [4] and published in the journal [5] or CMS [6, 7] notes[1].

[1]CMS notes are internal committee and accessible for the public.

Chapter 2

The CMS Experiment at the LHC

The LHC [8] has been designed to collide proton beams at center of mass energy of $\sqrt{s} = 14$ TeV and an instantaneous luminosity of $\mathcal{L} = 10^{34}$ cm^{-2}s^{-1}. This center of mass energy corresponds to a seven-fold increase in energy and a hundred-fold increase in integrated luminosity with respect to the current hadron collider experiments at Tevatron. This design luminosity and beam energy of the LHC have been chosen in order to study physics at the TeV energy scale. The main goal of the LHC is to investigate the potential manifestation of new physics beyond the SM and reveal the nature of electroweak symmetry breaking.

This chapter is an overview of the LHC, followed by a detailed description of the CMS experiment with its main sub-detectors.

2.1 An Overview of the Large Hadron Collider

The LHC [9] is a two ring superconducting hadron accelerator and collider installed in the existing 26.7 km tunnel that was constructed to host the CERN LEP machine. It is located near Geneva, Switzerland and lies between 45 - 170 m below the ground on a plane inclined at 1.4% sloping towards the lake Leman. The overview of LEP tunnel is represented in Figure. 2.1. The four detectors are installed in the experimental caverns around the collision points. The first two detectors, ATLAS [10] and CMS [11] are for general purpose experiments. The third detector LHCb [12] is dedicated to B-physics and the last detector is ALICE [13], is optimized for heavy ion collisions.

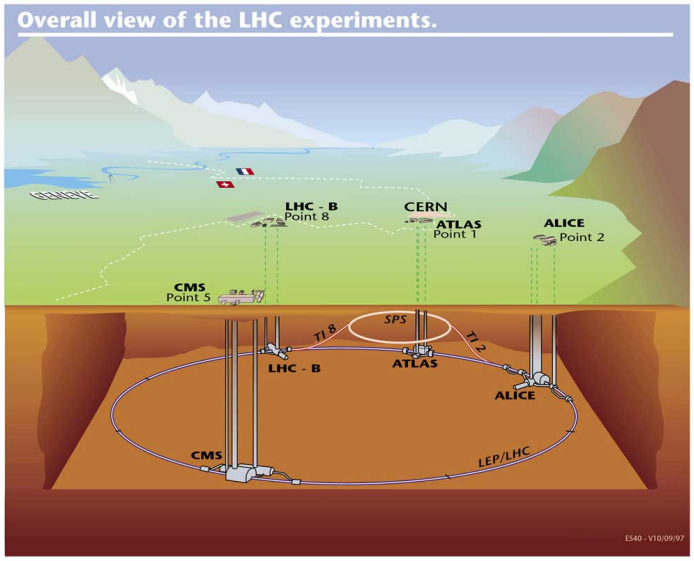

Figure 2.1: *Overall view of the LHC experiments*

The existing CERN facilities were upgraded to supply the LHC with pre-accelerated protons. A schematic view of the LHC accelerator with the injection chain is shown in Figure 2.2. The protons with energy of 450 GeV coming from the Super Proton Synchrotron (SPS) are injected into the LHC. In the LHC, they are accelerated to an energy up to a design energy of 14 TeV and currently running with 7 TeV (proton bunches with a nominal number of 1.15×10^{11} particles per bunch). Superconducting dipole magnets, which provide a magnetic field of 8.3 T, keep the accelerating protons in the orbit. These magnets are cooled by super-fluid helium to a temperature of 1.9 K.

The CMS experiment is located at one of the interaction points where collisions happen in every 25 ns, corresponding to a bunch crossing frequency of 40 MHz. The total proton-proton cross section at $\sqrt{s} = 14$ TeV is expected to be about 100 mb. At design luminosity, this general-purpose detector will observe an event rate of approximately 10^9 inelastic events per second. In the end of year of 2009, a commissioning run with the collisions at the center of mass energy of $\sqrt{s} = 900$ GeV and 2.36 TeV were performed while the operation of the

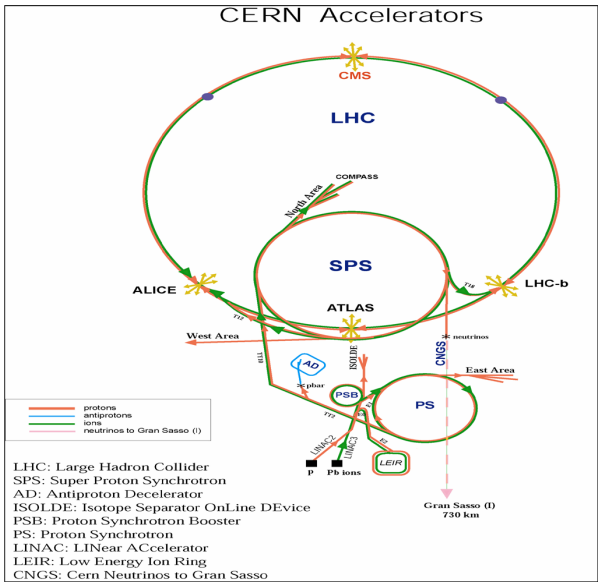

Figure 2.2: *The CERN accelerator complex. Schematic view of the LHC and the location of the four main experiments ATLAS, CMS, LHCb and ALICE*

LHC at the $\sqrt{s} = 7$ TeV began on March 30, 2010. In 2011, the recorded data (5.0 ± 2.2) fb^{-1} have good quality for physics analysis. The corresponding integrated luminosity recorded is shown in Figure 2.3. In 2012, its operation has been increased to $\sqrt{s} = 8$ TeV.

2.2 The CMS detector

The CMS detector is a general purpose particle detector designed for the physics environment provided by the LHC. It is installed 100 m underground at the LHC interaction point 5 (P5) near the village of Cessy in France. The LHC is designed to deliver approximately 10^9 inelastic pp collisions per second to the detector at designed energy and luminosity. The sampling frequency of the experiment is 40 MHz as the detector is read out once every bunch crossing which means about 23 pp inelastic interactions on average are superimposed on each event of interest of full design energy and luminosity. Hence, there is a non-negligible probability that one single bunch crossing may produce a number of separate inelastic interactions, which is referred as pileup interaction. The pileup effect can be reduced by requiring

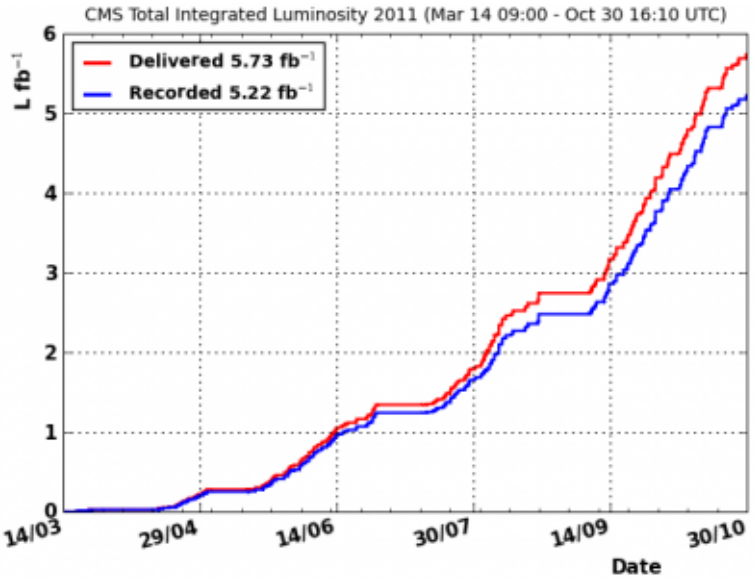

Figure 2.3: *Integrated luminosity recorded by the CMS experiment in 2011*

a large number of detector channels and an excellent synchronization among them.

The detector requirements for CMS to meet the goals of the LHC physics program can be summarized as follows [11]:

- Good muon identification and momentum resolution over a wide range of momenta and angles, good di-muon mass resolution (approximately 1% at 100 GeV), and the ability to determine the charge of muons with $p_T < 1$ TeV unambiguously.

- Good charged-particle momentum resolution and reconstruction efficiency in the inner tracker. Efficient triggering and offline tagging of τ's and b-jets, requiring pixel detectors close to the interaction region.

- Good electromagnetic energy resolution, good diphoton and dielectron mass resolution (approximately 1% at 100 GeV), wide geometric coverage($|\eta| < 2.5$), π_0 identification and eventually rejection, and efficient photon and lepton isolation at high luminosities.

- Good missing transverse energy (E_T^{miss}) and jet energy resolution, requiring hadron calorimeter with a large hermetic geometric coverage ($|\eta| < 2.5$) and with fine later

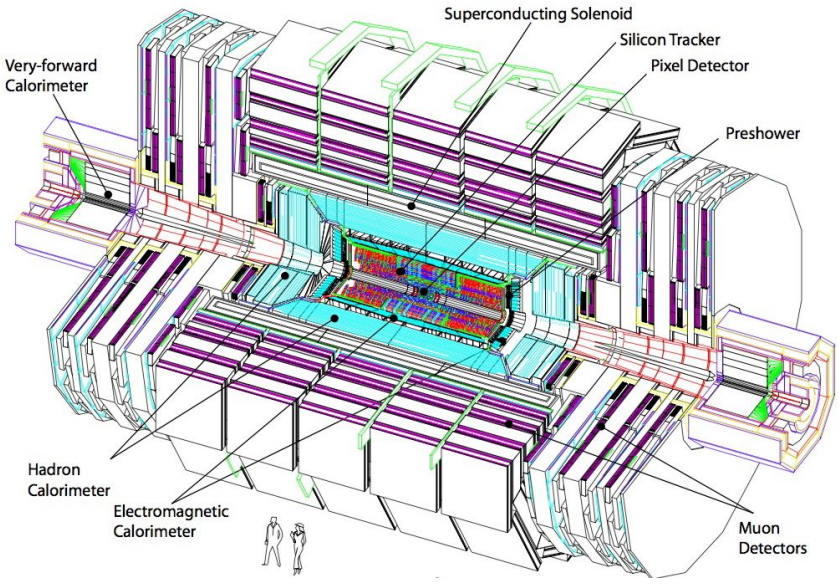

Figure 2.4: *Illustration of the CMS detector*

segmentation.

The CMS detector is subdivided into a silicon tracking system, an electromagnetic calorimeter, a hadronic calorimeter, and a muon system. A magnetic field of 3.8 T is provided by a super conducting solenoid magnet. The CMS detector is 22 m long, has a diameter of 15 m and an overall weight of 12.5 $\times 10^7$ kg. A schematic view of the CMS detector is shown in Figure 2.4.

2.2.1 Coordinate Conventions

The CMS detector is cylindrical with three major subdivisions which are a central barrel and two endcaps. This detector uses a right handed Cartesian coordinate system, with origin located at the assumed interaction point of the center of the detector. The orientation of CMS coordinate system is done in such a way that the $x-$axis pointing radially inward towards the center of the LHC and the $y-$axis pointing vertically upward and the $z-$axis is in the direction to the beam. The azimuthal angle ϕ is measured from the $x-$axis in the $x-y$ plane, and has the range $(-\pi, \pi)$. The polar angle θ is measured from the $z-$axis.

Pseudorapidity is defined as $\eta = -\ln(\tan\frac{\theta}{2})$. The momentum component transverse to the beam direction is denoted by p_T[1] which is computed from the x and y components. The transverse energy is defined as $E_T = E\ \sin\theta$. Both energy and momenta are expressed in units of eV.

2.2.2 Superconducting Magnet

The superconducting magnet provides 3.8 T of magnetic field which is 10^4 times stronger than that of the magnetic field of the Earth. The more momentum the particle possesses, the larger will be the curvature of the particle's trajectory due to the magnetic field. Hence, the strong magnetic field provides a large bending power for very high energetic charged particles. The magnet coil is 13 m long, 6 m inner diameter, and stores 2.6 GJ at full current. The magnet flux is returned through a 10^7 kg iron yoke in which the muon detector chambers are integrated.

2.2.3 The Silicon Tracker

The silicon tracker is the closest sub-detector to the beam-pipe. It is designed to obtain precise measurement of the momentum of charged particles using position of energy depositions. The tracker is also used to measure the vertices of hard interactions. The transverse momentum of particles can be calculated by measuring the radius of curvature as they travel through the detector. It has a total length of about 540 cm and extends to nearly 110 cm from the beam-pipe. A schematic of the tracker configuration has been shown in Figure 2.5.

The tracker can be subdivided into of two components: the pixel detector and the silicon strip detector. The pixel detector is closer to the interaction vertex, where the particle flux is the highest, because it provides high resolution information. It has 1440 pixel modules containing 66 million pixels and a silicon strip tracker with 15148 strip detector modules containing 9.6 million silicon strips. Each system is completed by endcaps extending the

[1] $p_T = \sqrt{p_x^2 + p_y^2}$

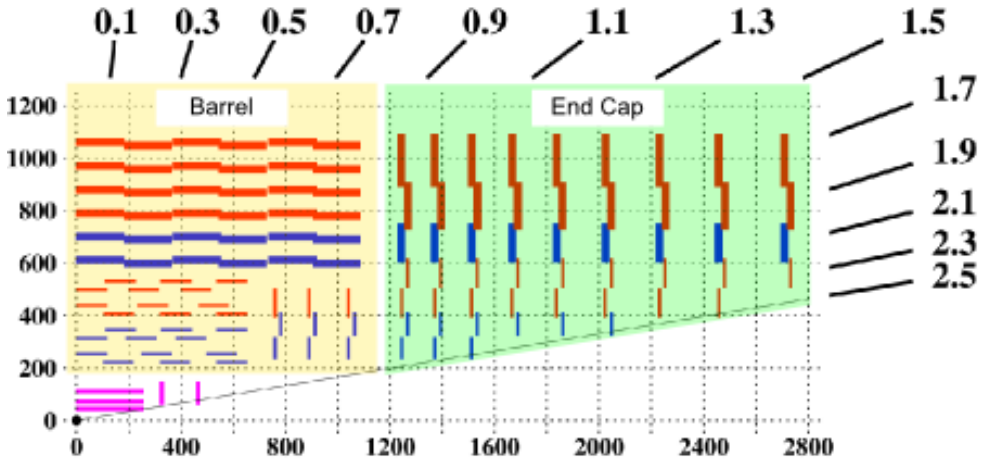

Figure 2.5: *The layout of the tracker.*

geometrical acceptance to a pseudorapidity of $|\eta| < 2.5$. The CMS tracking system provides a precise and efficient measurement of trajectories of charged particles, as well as precise reconstruction of primary and secondary vertices. It can also precisely measure track impact parameter variables such as the longitudinal and transverse distances from the vertex. In the barrel, the pixel detector has 3 layers that are 53 cm long and are located at a radial distance of 4.4 cm, 7.3 cm, and 10.2 cm from the beam. In the endcaps, the pixel detector has 2 pixel layers arranged in a fan-blade design with a radius of 6 cm and 15 cm from the beam and at position of $|z| = 34.5$ cm and $|z| = 46.5$ cm, respectively, from the interaction point, as shown in Figure 2.6. There are altogether 768 pixel modules in the barrel pixel (BPix) and 672 modules in the forward pixel (FPix). Each module is made up of pixel cell with a cell size of 100×150 μm^2. The resolution in the $r\phi$ plane is about 10 μm and $r - z$ plane is about 20 μm.

The silicon strip detector covers the region from about 20 cm to 116 cm from the beam. It is beyond the third pixel layer, at a distance of $r = 20$ cm from the beam pipe. The silicon strip detector provides coverage out to $r = 116$ cm from the barrel, $|z| = 280$ cm from the point of interaction, and $|\eta| < 2.4$. The different components of the silicon strip detector are shown in Figure 2.7. They are the four-layer Tracker Inner Barrel (TIB), the six-layer tracker outer barrel (TOB), on each side three-disk Tracker Inner Disks (TID), and

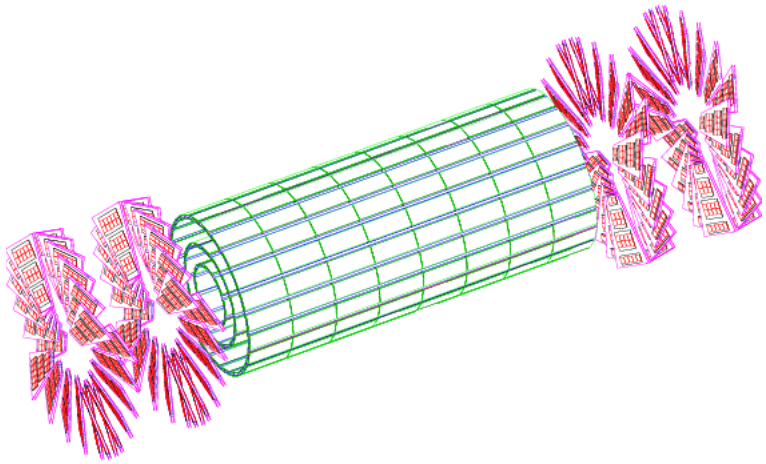

Figure 2.6: *The configuration of the pixel detector*

nine-disk Tracker Endcaps (TEC).

The overall design of the tracking system is a compromise between the desire to maximize the momentum measurement and vertex resolution and to minimize the amount of extra material present in the detector, such as detector electronics and cooling hardware, which might lead to photon conversion, bremsstrahlung, and other particle interactions unrelated to the collision that would reduce the resolution energy measurement in the calorimeters [11].

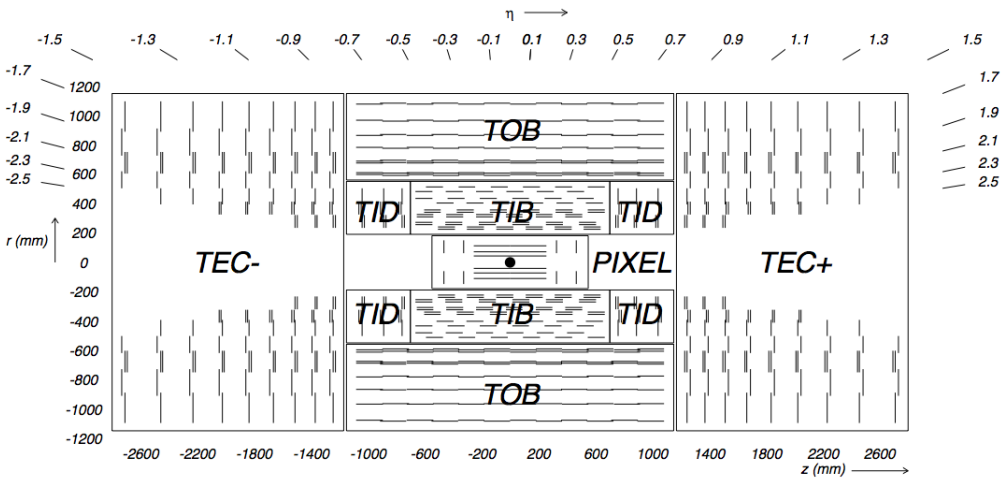

Figure 2.7: *The configuration of the silicon strip detector.*

Track Reconstruction

The charged particles travels in a helical path due to the presence of the magnetic field. The helix trajectory can be described in terms of 5 parameters: the curvature κ, the track azimuthal angle ϕ, polar angle η, the transverse impact parameter d_0 which is the defined as the distance of the closest approach of the track to the primary vertex and the longitudinal impact parameter z_0.

The Combinatorial Track Finder (CTF) algorithm is the standard algorithm used to reconstruct charged particle's trajectory in CMS. The CTF algorithm has three steps: track seeding, track finding, and track fitting. In the standard tracking, a seed is made out of a hit pair in the inner pixel layers plus the beam spot constraints or out of a hit triplet in the inner pixel layers. The track reconstruction is the pattern recognition, which is to identify a candidate trajectory based on the hits in the event. The track finding stage is based on a standard Kalman filter pattern recognition approach [14], which starts from the seed parameters. Each seed is propagated to the another surface of the tracker. Hits are searched in a window whose width is related to the precision of the track parameters. If a hit is found in the expected position, it is added to the candidate's trajectory and the track parameters are updated. As hits are added to the candidate trajectory, there is improvement of the track parameters. If a consecutive hit is not found in the predicted position, the trajectory is rejected and is not propagated any more as shown in Figure 2.8. Trajectory building continues until the trajectory reaches the end of the tracker. If two tracks share more than 50% of their hits, then the track with the highest χ^2 value is discarded [15]. Final fit uses all hits to obtain the best measurement of the track parameters at the point of the origin.

2.2.4 Electromagnetic Calorimeter

The electromagnetic calorimeter (ECAL) of CMS is a nearly hermetic homogeneous calorimeter made of 61200 lead tungsten ($PbWO_4$) crystals mounted in the central barrel, closed by 7324 crystals in each of the endcaps. A preshower detector is placed in front of the

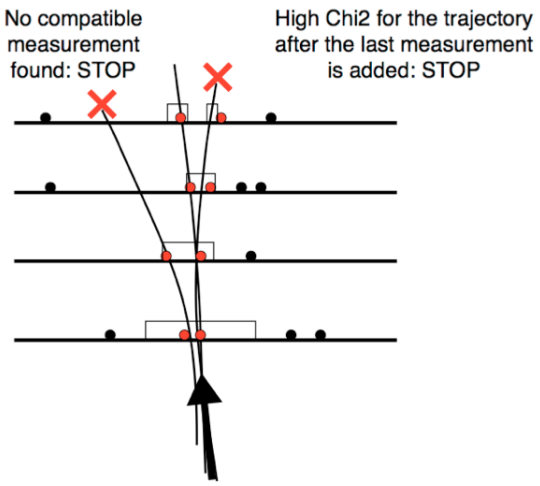

Figure 2.8: *Kalman Filter based pattern recognition.*

endcap crystals. Avalanche photo-diodes (APDs) are used as photo-detectors in the barrel and vacuum photo-triodes (VPTs) in the endcaps. The $PbWO_4$ crystals are an appropriate choice in LHC because they are used to measure the energy of electromagnetic interacting particles like photons and electrons. They do so by causing the particles to decay within the calorimeter, through electromagnetic showers in the case of the ECAL, and then measuring the deposited energy. The choice of $PbWO_4$ as the material for the scintillation crystal is due to its fast response time and high radiation resistance. The high density (8.28 g cm^{-3}), short radiation length (0.89 cm) and small Moliere radius (2.2 cm) results in a fine granularity and a compact calorimeter. The barrel part (EB) of the ECAL covers the pseudorapidity range $|\eta| < 1.479$ and within $1.479 < |\eta| < 3.0$ are the endcap regions (EE). Each crystal is 23 cm long and subtends 0.0174×0.0174 in $\eta \times \phi$ (22 cm $\times$ 22 cm) in the EB and 2.47 cm $\times$ 2.47 cm in the EE. The analysis, which is discussed in the next chapter, covers the barrel region which has 360 crystals in ϕ, and 170 in η direction. These crystals are mounted in a quasi-projective geometry so that their axes make a small angle (3^o) with respect to the vector from the nominal collision vertex, in both the ϕ and η. This is done to avoid trajectories of the particles to fall between boundary of crystals.

The centers of the front faces of the barrel crystals are at a radius of 1.29 m. The

crystals are contained in a thin-walled alveolar structure (sub-module). The sub-modules are assembled into modules of different types, based on the position in η each containing 400 or 500 crystals. There are four modules, which are separated by aluminum conical webs 4 mm thick, are assembled in a super-modules, which contains 1700 crystals.

In EE, the longitudinal distance between the interaction point and the endcap envelop is 315.4 cm, taking into account of the estimated shift toward the interaction point by 1.6 cm when the 4 T magnetic field has been switched on. The endcap consists of identical shaped crystals grouped in a mechanical units of 5 $\times$ 5 crystals (supercrystals).

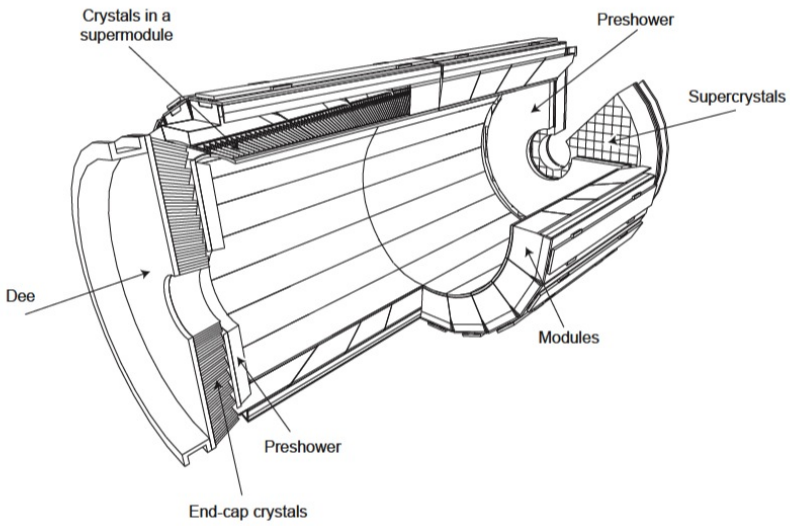

Figure 2.9: *Layout of the CMS electromagnetic calorimeter showing the arrangement of crystal modules, super-modules and endcaps, with the preshower in the front.*

Each endcap is divided into two halves called as "Dees". Each dee holds 3663 crystals. The crystals have a rear face cross section 30 $\times$ 30 mm^2, a front face cross section 28.62 $\times$ 28.62 mm^2 and a length of 220 mm which corresponds to 24.7 X_o. A preshower system is installed in the front of the endcap for π^0 rejection. The main goal of the CMS Preshower detector is to improve the photon identification by rejecting the two closely separated photons from neutral π^0 decay in the fiducial region $1.653 < |\eta| < 2.6$ of the endcaps.

The preshower is considered as a sampling calorimeter with two layers:

- the lead radiators initiate electromagnetic showers from incoming photons or electrons,
- the silicon strip sensors placed after each radiator measure the deposited energy and the transverse shower profiles.

The energy resolution of the ECAL can be parametrized by the following expression:

$$\left(\frac{\sigma}{E}\right)^2 = \left(\frac{S}{\sqrt{E}}\right)^2 + \left(\frac{N}{E}\right)^2 + C^2, \tag{2.1}$$

where S is the intrinsic stochastic term , N the noise term, and C the constant term. From test beam data, the parameters of energy resolution are measured to be N = 0.12 GeV, S = 2.8 %, and C = 0.3 % [11]. In Figure 2.10 shows the ECAL energy resolution as a function of electron energy is shown as measured from the test beam.

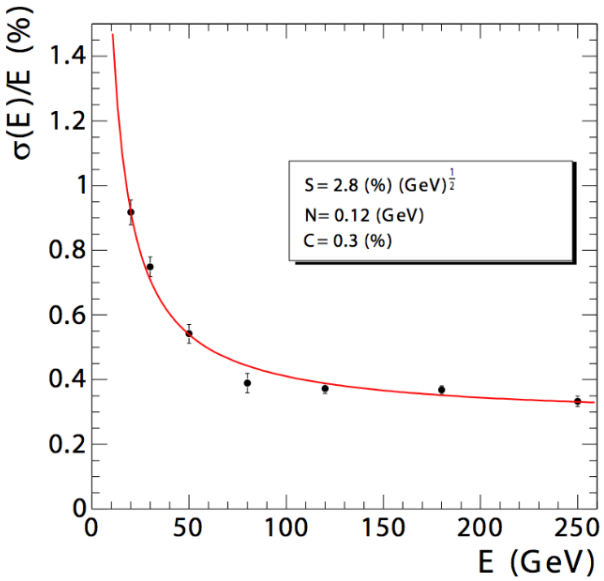

Figure 2.10: *ECAL energy resolution, $\frac{\sigma(E)}{E}$, as a function of electron energy as measured from a test beam.*

2.2.5 Hadronic Calorimeter

The measurement of energy in the ECAL is complemented by the hadronic calorimeter (HCAL). The HCAL is a sampling calorimeter consisting of the layers of brass interspersed with the plastic scintillator tiles which are arranged in trays. The plastic scintillator has been used for its stability and radiation hardness while the brass layers are chosen since it is dense, nonmagnetic, and structurally stable. The HCAL is to measure the energy of hadronic. The charged hadrons such as protons, π^+, π^- are bent by the magnetic field, while neutral hadrons (neutrons) are unaffected by this field and they travel straight through the ECAL leaving almost no signal. Upon reaching the HCAL, they pass through the dense materials, producing showers of secondary particles. The cascade particles then pass through the scintillator and interact, causing the scintillator to fluorescence. The signals collected in the different layers of scintillator are combined together to estimate the energy of the hadrons. As the scintillator fluoresces, it emits lights in the blue-violet range which goes through wavelength-shifting fibers embedded in the scintillator to hybrid photo-diodes which convert the signal to electrical pulses. There are about seventy thousand scintillator tiles which are sandwiched between brass absorber layers. The hadronic calorimeter has a barrel part (HB and HO) at $|\eta| < 1.3$, an endcap (HE) on each side at $1.3 < |\eta| < 3$, and a forward calorimeter (HF) extending up to $|\eta| < 5.2$ to achieve most of the hermetic detector coverage. The HCAL tower segmentation in the rz plane for one quarter of the HB, HO, and HE detectors is shown in Figure 2.11. Hadronic showers are long and require about a meter of material to be accurately measured. Hence, HCAL barrel component fills the space between the ECAL and the solenoid with an additional outer calorimeter (HO) which acts as additional absorbing material. Furthermore, the HF component of HCAL is at a longitudinal distance of 11.2 m from the interaction point. It is subjected to an unprecedented particle fluxes. An estimated energy of 760 GeV is deposited on average in proton-proton collision at $\sqrt{s} = 14$ TeV. The HF consists of the steel absorber plates composed of 5 mm in thickness grooved plates with quartz fibers inserted as an active

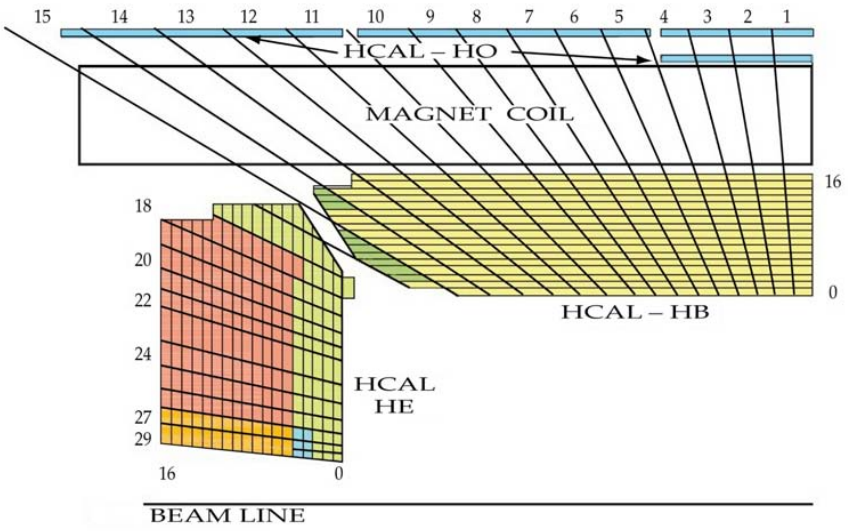

Figure 2.11: *Tower segmentation for one quarter of the HCAL displayed in the rz plane. The colors represent the optical grouping of scintillator layers into different longitudinal readouts.*

medium. HF detects the Cherenkov light emitted by charged particles in the shower and is, thus, mainly sensitive to the electromagnetic component of the shower. HF part of the detector is functionally subdivided into two longitudinal segments. This arrangement allows to distinguish signal generated by electrons and photons from signal generated by hadrons.

2.2.6 Muon system

The main role of the CMS muon detector is to provide muon identification, track reconstruction, and trigger of muons with momenta from a few GeV to a few TeV [16]. Good muon momentum resolution and trigger capability are enabled by the high field solenoid magnet and its flux-return yoke. The CMS muon system is designed with the capability to reconstruct the momentum and charge of the muons over the entire kinematic range of the momentum spectrum accessible in LHC collision event. The muon system is the outermost part of the CMS detector. Three different types of gaseous detectors are integrated into the CMS muon system depending on the requirements [11]. In the barrel part, drift tube (DT)

chambers are used. Also, in the barrel part, both the muon rate and the neutron induced background are small and the magnetic field is very low. While in the endcaps, the muon and the background flux is much higher. Hence, the muon detectors endcaps are made of from cathode strip chambers (CSCs) to provide a faster response, a higher granularity and a better resistance against radiation. Furthermore, resistive plate, (RPCs) form a redundant trigger system. Hence, the CMS muon system comprises of 250 DT chamber, 610 RPCs, and 540 CSCs. The arrangement of the detector chamber is shown in Figure 2.12.

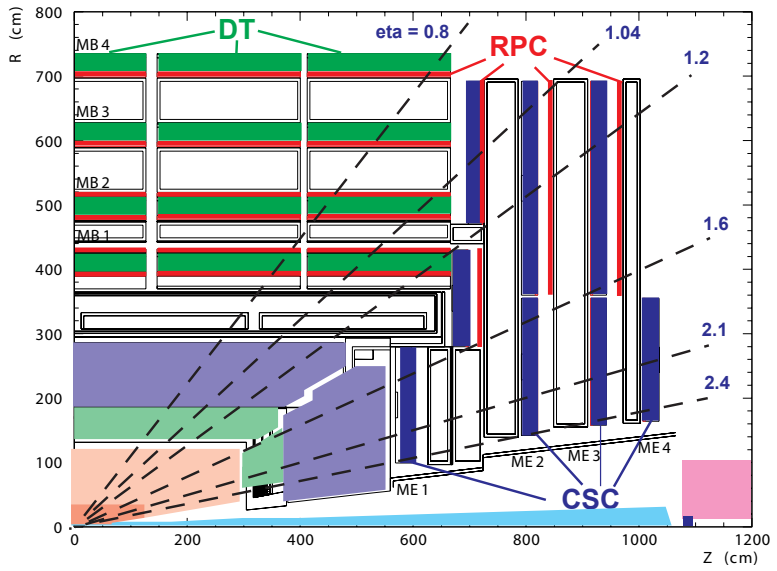

Figure 2.12: *Quarter-view of the CMS detector. Cathode strip chambers of the Endcap Muon system are highlighted.*

A DT cell is a gas tube with width of 4 cm and has a positively charged stretched wire inside it. Each DT chamber consists of 12 layers of DT cell and arranged in three groups of four. The middle group has been used to measure the z coordinate while the two outer groups to measure $r-\phi$ coordinate. The four DT chambers are interspersed with the layers of the flux return yoke in each ϕ section in the barrel. The outermost muon station has DT chambers with 8 layers of DT cells to determine the position of muon in the $r\phi$ plane. The barrel part of the muon system covers the region $|\eta| < 1.2$.

The CSCs are trapezoidal shaped multi-wire proportional chambers with 6 anode wire planes crossed with 7 copper strips cathode panel in a gas volume providing a two-dimensional position measurement. These copper strips and the anode wire represent r and ϕ coordinates. The 4 CSC stations are on each side of the muon detector endcaps to identify muons in the pseudorapidity range of $0.9 < |\eta| < 2.4$.

RPCs have two high resistive plastic plates with a voltage applied and separated by a gas volume. The signal generated by the muon when passing through the gas volume is detected by readout strips mounted on top of one of the plastic plates. Furthermore, the RPSs are used in the muon trigger system for a quick response with a time resolution of about 1 ns. Six layers of RPCs are installed in the barrel muon system, two layers in each of the first two stations and one layer in each of the last two stations. One layer of RPCs is built into each of the first three stations of the endcap.

Muon Reconstruction

Muon reconstruction has been done in two stages: stand-alone reconstruction which is based on information from the muon system only and for global reconstruction that combines standalone tracks and tracker tracks which is shown in Figure 2.13. The stand-alone reconstruction starts from track segments in the muon chamber, and muon trajectories are built from the inside to the outside using the Kalman filter method. Once the trajectory is built, a second Kalman filter, working from outside in, is applied to determine the track parameters. At the end, the track is extrapolated to the nominal interaction point and a vertex-constrained fit of the track parameters is performed.

In the global muon reconstruction, the muon trajectories are extended to include the hits measured by the tracker. The track parameters of a stand-alone reconstructed muon are compared to the track parameters of the tracker tracks by extrapolating the trajectories to a common plane of the inner surface of the muon detector. If a found tracker track is compatible in the momentum, position, and direction, the hit information of the tracker and the muon system are combined. Then it is refitted to form a global muon track. The

resulting global tracks are then checked for ambiguity and quality to choose at the most one global track per stand-alone muon.

The precision of the momentum of muon, in the muon system is determined by the measurement of the bending of angle in the transverse plane at the exit of the magnetic coil. This measurement is dominated by multiple scattering in the material before the first muon station up to transverse momentum values of 200 GeV. For low-momentum muons, the resolution is enhanced by considering the measurement of the silicon tracker. The inclusion of the information from the tracker by using global muons is the most valuable. A comparison of the momentum resolution of the muon system is shown in Figure 2.14.

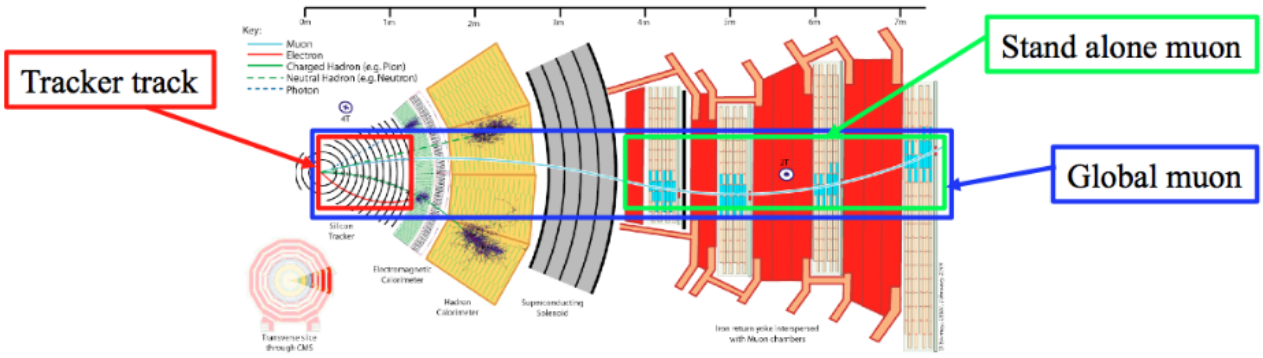

Figure 2.13: *Muon Reconstruction*

2.3 Trigger System

The amount of data needed to record all information of an event is on the order of 250 kB at 40 MHz. But to store the data for each *pp* collision would require writing several TB per second. The importance of the trigger system is to select the interesting events to reduce the recorded event rate to a more manageable rate which is 100 Hz for data storage. CMS employs a two-level trigger system to get rate reduction by a factor of 10^6. They are known as the Level-1 (L1) Trigger and the High Level Trigger (HLT). The L1 trigger reduces the input rate of 40 MHz to below kHz. L1 does not use full-resolution information from the various CMS sub-detectors, but uses coarsely segmented data to make a decision whether

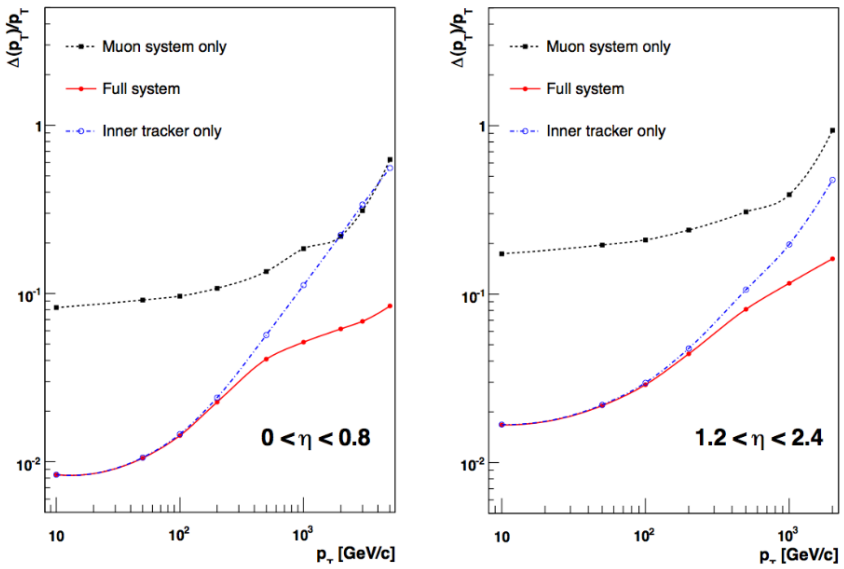

Figure 2.14: *The muon transverse-momentum resolution as a function of the transverse-momentum using the muon system only, the inner tracking only, and both.*

to discard the collision information or to pass pass it to HLT. A schematic of the flow of information through the Level 1 system is shown in Figure 2.15. The L1 trigger has two main systems, which are the calorimeter trigger and the muon trigger. Using the DT and RPC in the barrel and CSC in the endcap, the muon trigger system searches the top four highest energy muon candidates. Both the calorimeter and the muon trigger system provide this information to the global trigger to make the final decision keep or reject an event.

Once an event is selected by the L1 global trigger, it moves on to the HLT. The HLT is a software-based and runs on commercially available processors. It uses the full resolution information and so uses the similar algorithms as used offline for computations such as object isolation or momentum.

2.4 Supercluster reconstruction

The electromagnetic (EM) showers initiated by electrons or photons deposit their energy in several crystals of the ECAL. Approximately 94% (97%) of incident energy of a single

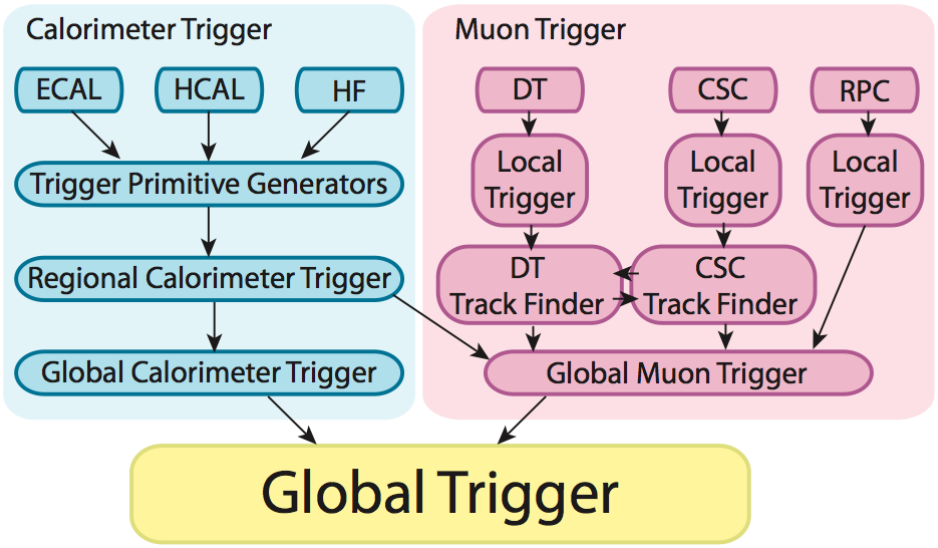

Figure 2.15: *Schematic showing the flow of information passes through the various system within the Level-1 Trigger.*

photon or electron is collected in 3×3 (5×5) crystal array. By summing the energy measured in such arrays provides the best performance for unconverted photons, or for the electrons. The presence of tracker material which is distributed in front of the ECAL and strong magnetic field result in bremsstrahlung and photon conversions as well as the energy of a photon or a electron reaches the ECAL with significant spread in ϕ direction. This spread of energy in ϕ direction is clustered by building a cluster of clusters which is known as a supercluster. Two clustering algorithms are implemented in CMS to accommodate geometry of the detector and grouping of crystals are summarized as follow. The "hybrid" and "multi5×5"algorithms are used for the barrel and the endcap, respectively [17]. The hybrid algorithm starts with finding the crystal with E_T to be above 100 MeV to reduce the noise contamination. If $E_T > 1$ GeV, this crystal can seed the clustering process. Otherwise the clustering process will be terminated. In general, a 3×1 domino of crystal is constructed in η-ϕ direction. A threshold value of 3×1 domino of crystal has been represented in terms of E_{wing} which is zero. If $E_{\text{domino}} > E_{\text{wing}}$, the domino has been extended to 5×1 symmetrically

around the seed crystal. Staying at the same η, begin stepping along ϕ and added these 5×1 dominoes as long as the energy within the domino is above a minimum threshold 0.1 GeV. This step is repeated for all crystals with the same η as the seed crystal and within a searching road in ϕ till 17 crystals in both directions from original seed crystal.

In multi5×5 algorithm, the crystal with the highest E_T should be above 180 MeV. A cluster has been constructed from array of crystal 5×5 centered on the seed crystal joined together. Crystals along the edge of this 5×5 array are allowed to be the seeds of new 5×5 cluster if they are a local maximum when compared to neighboring crystals. Then the overlapping arrays of 5×5 crystals are joined together into one supercluster.

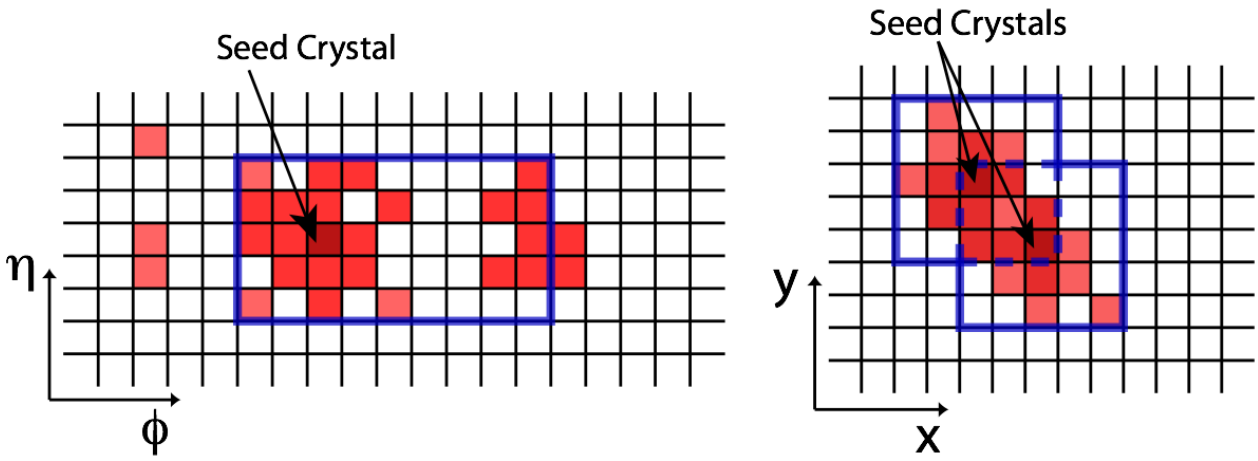

Figure 2.16: *Hybrid Supercluster Algorithm (left) and Multi5×5 Algorithm (right).*

For both the algorithms are shown in Figure 2.16, the location of a supercluster is determined by a weighted average of all the positions in the supercluster. Each ith crystal in the supercluster is given a weight which is represented by the equation as 2.2:

$$w_i = max(0, 4.7 + log\left(\frac{E_i}{E_{sc}}\right)) \tag{2.2}$$

2.4.1 Photon reconstruction

Photon objects are reconstructed from corrected superclusters, by assigning the candidate momentum to the location of the reconstructed primary vertex [18].

The energy corresponding to each photon candidate is estimated based on the observable R9 which is defined as the ratio of the energy contained within the 3×3 array of the crystals centered on the seed crystal of the photon candidate's supercluster to the total energy contained in the supercluster. If R9 < 0.94, EM shower is from a photon converted before reaching to the ECAL. If R9 > 0.94, the EM shower is assumed to be from the unconverted photons. Hence, if R9 of the photon candidate is above 0.94 (0.95) in the barrel (endcap), the energy of the 5×5 crystal around the highest energy crystal is used. Since the crystals in the endcap are larger than in the barrel, R9 threshold is higher in the endcap than in the barrel.

The position of the photon is taken as the log energy weighted average position of the crystals used for energy determination as mentioned in section 2.4 for clustering algorithm. The photon arrival time is consistent with time of the seed crystal [19].

2.5 Particle flow Algorithm

The particle flow (PF) algorithm sequentially aggregates the informations of all stable particles (i.e., electrons, muons, photons, charged hadrons and neutral hadrons) from all the sub-detectors for a single collision to form a complete picture of the event. A particle expected to give rise to several PF elements in the various CMS sub-detectors like one charged particle track, and or several calorimeter clusters, and or one muon track. Hence, the signals from the sub-detectors are initially combined into "elements" as charged particle tracks, calorimeter clusters, and muon tracks. The elements are linked within and between sub-detectors into blocks with a linking algorithm as follows [20]:

- The link between a track and a calorimeter cluster is done by extrapolating the track from its last measured hit in the tracker to (i) the ECAL at a depth equals to the

maximum of a typical longitudinal electron shower profile and (ii) the HCAL at a depth equals to one interaction length, typical of a hadron shower. The track is linked to a cluster if the extrapolated position is within the cluster boundaries. Hence, the distance in the (η, ϕ) plane between the extrapolated track position and the cluster position is called the link distance.

- Link between the ECAL cluster and the HCAL cluster is possible if the ECAL cluster position is within the cluster envelop of the HCAL. The link distance in this case is defined in (η, ϕ) plane as the distance between these two cluster positions.

- Finally, a link between a charged particle track in the tracker and a muon track in the muon system is established (i.e; global muon) if a global fit between these two tracks returns an acceptable χ^2. This χ^2 defines the link distance.

Muon candidates are reconstructed first and their elements are removed from the blocks, electron reconstruction follows, and the remaining information is reconstructed into photons, hadrons [20]. These PF reconstructed particles are further combined to more complex object like jets and E_T^{miss}.

2.6 Jet reconstruction

Jets are relatively collimated streams of particles which are primarily composed of hadrons and other particles that originate from a single parton. In this analysis, jets are reconstructed by the particle flow constituent particles by anti-k$_T$ algorithm [21]. The anti-k_T algorithm is a combination of k_T and Cambridge/Aachen jet-finding algorithms. In general terms, the algorithm proceeds by building a cluster by comparing the distances d_{ij} between entities (two particles or clustered pseudo-jets) and d_{iB} corresponds to the distance between i-th entity and the beam. If d_{ij} is the smaller distance than d_{iB}, the two objects are clustered into the same jet and the algorithm continues to make comparisons between i-th entity and other nearby entities. If d_{iB} is the smaller distance than d_{ij}, i-th entity is considered a

complete jet and removed from the algorithm; this process is repeated until no objects are left to compare.

If the smallest distance is a d_{ij}, the corresponding particles are combined, otherwise particle i is defined as a jet. The distance between any two particles i and j and the distance of any particle i to the beam which are defined as:

$$d_{ij} = \min(k_{Ti}^{2p}, k_{Tj}^{2p})\Delta_{ij}^2/R^2; \qquad d_{iB} = k_{Ti}^{2p} \tag{2.3}$$

where $\Delta_{ij}^2 = (\eta_i - \eta_j)^2 + (\phi_i - \phi_j)^2$ and k_{Ti}, η_i and ϕ_i are the transverse momentum, rapidity, and the azimuthal angle of particle i respectively. R is the radius of the cone used in the clustering algorithm and the parameter p is the relative power of the energy geometry relationship. For p = 1, one recovers the inclusive k_T algorithm. For p = -1 refers to the anti-k_T jet clustring algorithm. The functionality of the anti-k_T algorithm can be understood by considering an event with a few well-separated high energetic particles with transverse momenta k_{T1}, k_{T2} and many low energetic particles. The distance $d_{1i} = \min(k_{T1}^{-2}, k_{Ti}^{-2})\Delta_{1i}^2/R^2$ between a high energetic particle 1 and a low energetic particle i is exclusively determined by the transverse momentum of the high energetic particle and Δ_{1i} separation. If d_{ij} between low energetic particles is much larger than d_{iB}, these less energetic particles tend to cluster with the more energetic ones before they cluster among themselves. If a high energetic particle has no other neighbors within a distance 2R, then it will simply accumulate all the less energetic particles within a circle of radius R, resulting in a perfectly conical jet [21]. There are three clustering scenarios which are as if a high energetic particle has no other similar energetic neighbors within a distance of $\Delta_{ij} = 2R$, a conical jet will be reconstructed; if two high energetic particles are within $R < \Delta_{ij} < 2R$, two jets will be reconstructed and one or both of them will be have a non-conical shape, with the separation determined by their relative k_T; if two high energetic particles are within $\Delta_{ij} < 2R$, they will cluster to form a single non-conical jet. In the end, the high energetic jets are reconstructed with a circular radius while low energetic jets have projection in complex cone. The value of R is 0.5 for the jets in $Z\gamma$ analysis.

2.7 Missing Transverse energy

The CMS detector is able to detect most of the particles which are produced in pp collisions. But, the neutrinos escape from the detector without leaving their traces. Their presence can be inferred as missing transverse momentum ($\overrightarrow{E}_T^{miss}$) and the magnitude of the missing transverse momentum is called missing transverse energy (E_T^{miss}) as shown in Figure 2.17. The incoming particles in a collision possess no component of momentum in the transverse plane. The conservation of momentum requires that vector sum of p_T of all the reconstructed particles after collision must vanish and any imbalance in the this sum may be contributed to particles which leave no signature in the detector. Hence, E_T^{miss}, which is the magnitude of this imbalance in transverse momentum, is represented as:

$$E_T^{miss} = | -\sum_{i}^{n} \overrightarrow{p_{Ti}} | \tag{2.4}$$

where i is the index of the reconstructed object.

The reconstruction of $\overrightarrow{E}_T^{miss}$ is very sensitive to particle momentum mismeasurements, particle misidentification, detector malfunctions, cosmic-ray particles, and beam halo particles which may result in artificial E_T^{miss} [22]. In this analysis, PF E_T^{miss} has been used. It is reconstructed from the particle flow candidates [23].

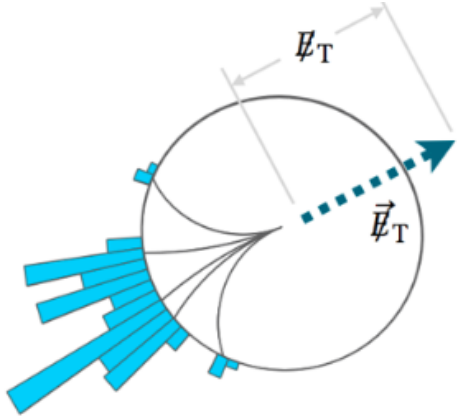

Figure 2.17: *An imbalance in transverse momenta of all reconstructed particles in an event.*

Chapter 3

Theoretical Motivation

3.1 The standard model

According to the SM, every matter is composed of particles called fermions and the forces between fermions are manifested as an exchange of bosons. Three generations quarks and leptons along with bosons are shown in Figure 3.1. Fermions are of two types commonly known as quarks and leptons. Quarks and leptons are spin-$\frac{1}{2}$ particles which are defined by their mass and quantum numbers. There are 24 elementary fermions: 6 quarks, 6 leptons as well as their respective antiparticles are characterized by the same mass but opposite quantum numbers. Both quarks and leptons can be organized by their mass into three generation pairs. The first lepton family includes the electron along with the electron neutrino. The second and third families contain the muon and the τ along with their neutrinos, respectively.

Each of the three families of the other fermion species, the quarks, consists of one $+\frac{2}{3}e$ and one $-\frac{1}{3}e$ charged quark, where e represents the elementary charge. The first family includes up (u) and down (d) quark. In the second family contains the strange (s) and charm quark (c), while the third family incorporates the bottom (b) and top quark (t).
Quarks are never observed alone but they form pairs and trios observed as mesons (quark-antiquark pair) and baryons (group of three quarks), respectively. The atomic nuclei is composed of protons and neutrons, which are bound states of uud, udd quarks, respectively.

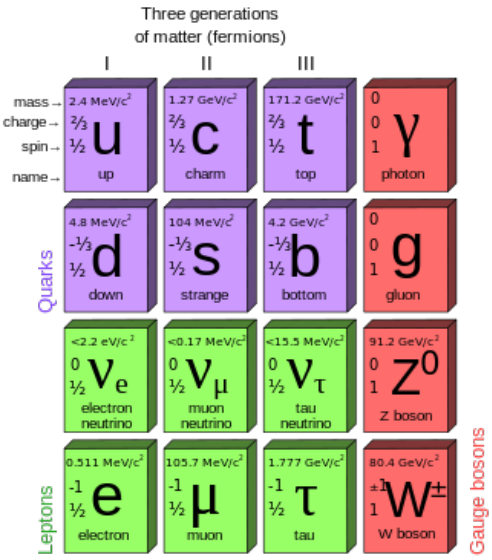

Figure 3.1: *The SM of elementary particles, with the gauge bosons in the right most column.*

All such observed bound states (baryons and mesons) can be accommodated within the quark model.

Three fundamental interactions (i.e., electromagnetic interaction, weak interaction, and strong interaction) are described by the SM, while the fourth interaction (i.e., the effect of gravitational interaction) is dominant at macroscopic distance only and hence is not integrated in the SM. Each interaction is mediated by spin-1 gauge particles. In the electromagnetic interaction, photons mediate the EM force between particles with charge. The massive gauge particles $W^{\pm}$ and Z bosons are exchanged among both leptons and quarks through the weak force which is the driving force in nuclear decays. The strong force, which binds the protons and neutrons in the atomic nucleus, couples to color and is mediated by 8 colored gauge bosons which are known as gluons. The full gauge group of the SM reads $SU(3)_C \times SU(2)_L \times U(1)_Y$ (C color, L weak isospin, Y weak hypercharge), $SU(2)_L \times U(1)_Y$ symmetry group that describes the unification of electromagnetic and weak force in the electroweak interaction. The mediators generated by this $SU(2)_L \times U(1)_Y$ symmetry are the vector bosons which are $W^{\pm}$, Z, and γ. The photon is massless while rest of the mediators

are massive. In order to produce a mass term for $W^{\pm}$, Z bosons that does not destroy the gauge invariance for SM Lagrangian, the spontaneous symmetry breaking mechanism is introduced. This mechanism predicts the presence of scalar particle known as the Higgs boson. The Higgs boson is a quanta of so-called Higgs field which has a non-zero expectation value at each point in space. The interaction of vector bosons with non-zero field results in the origin of mass in W and Z bosons while keeping the photons and gluons massless.

The fundamental interactions and their properties are summarized in Table 3.1.

Table 3.1: *The fundamental interactions and their properties.*

Symmetry	Interaction	gauge boson	mass [GeV]	range [m]
$SU(2)_L \times U(1)_Y$	electromagnetic	photon	0	∞
	weak	$W^{\pm}$	80.4	$\approx 10^{-18}$
		Z^0	91.2	
$SU(3)_C$	strong	eight gluons	0	$\approx 10^{-15}$
-	gravity	graviton	0	∞

3.1.1 Electroweak Theory

The electroweak interaction unifies electromagnetic and the weak interaction and is stated in previous section 3.1. The Lagrangian for the electroweak interactions are based on $SU(2)_L \times U(1)_Y$ symmetry group is described as:

$$L_{\text{EWK}} = L_{\text{gauge}} + L_{\phi} + L_{\text{fermi}} + L_{\text{Yukawa}} \tag{3.1}$$

The second term of equation 3.1 describes Higgs field of electroweak interactions, the third term corresponds to interaction of the fermions with the gauge boson, and the last term of this equation describes the Yukawa interaction which is the interaction between fermions and the scalar field and the first term represents the coupling among the gauge fields and is represented as :

$$L_{\text{gauge}} = -\frac{1}{4} B_{\mu\nu} B^{\mu\nu} - \sum_{i=1}^{n=3} \frac{1}{4} W^i_{\mu\nu} W^{i\mu\nu} \tag{3.2}$$

In this equation 3.2 [24], $W^i_{\mu\nu}$ and $B_{\mu\nu}$ can be expressed as:

$$W^i_{\mu\nu} = \partial_\mu W^i_\nu - \partial_\nu W^i_\mu - g\epsilon_{ijk} W^j_\mu W^k_\nu, \; B_{\mu\nu} = \partial_\mu B_\nu - \partial_\nu B_\mu \tag{3.3}$$

The W^i_μ and B_μ in equation 3.3 correspond to $SU(2)_L$ and $SU(1)_Y$ fields respectively, and g is coupling constant of $SU(2)_L$. The electroweak bosons are the combination of W^i_μ and B_μ fields and expressed as:

$$W^\pm_\mu = \frac{W^1_\mu \mp i W^2_\mu}{\sqrt{2}} \tag{3.4}$$

$$Z_\mu = W^3_\mu \cos\theta_W - B_\mu \sin\theta_W \tag{3.5}$$

$$A_\mu = W^3_\mu \sin\theta_W + B_\mu \cos\theta_W \tag{3.6}$$

Equation 3.4 refers to the charge bosons ($W^\pm_\mu$) which are the linear combinations of W^1_μ and W^2_μ fields. The rest of two equations 3.5, 3.6 correspond to neutral boson Z_μ (the Z^0) and A_μ (the photon) are mixtures of W^3_μ and B_μ fields. θ_W represents Weinberg angle which describes the relation between $SU(2)_L$ and $SU(1)_Y$ couplings, g and g' as $\tan\theta_W = \frac{g'}{g}$. The SM also allows for the self coupling of the gauge bosons through the L_{gauge} term in equation 3.1. This leads to trilinear gauge boson couplings ($WW(Z/\gamma)$) and quadratic gauge couplings with a requirement that at least two charged weak bosons are present. The $SU(2)_L$ symmetry group does not allow any neutral vertices with only Z bosons and photons [25]. The theory beyond the SM predicts the presence of such vertices with Z bosons and photons. It considers Z boson is composed of charged preons which are assumed to be point-like hypothetical particles. These charged preons couple to photons [26] as a result of which there is possibility of Z boson and a photon can self interact.

3.2 Theory of $Z\gamma$ Process

3.2.1 $Z\gamma$ production

The $W^\pm$ and Z bosons were first discovered in 1983 with UA1 and UA2 experiments at the CERN [27, 28] Super Proton Synchroton (SPS). The properties of these gauge bosons and

their decay modes have been studied in detailed. Z bosons decay hadronically 70% of time while 30% of time, they decay to leptonic modes. In leptonic mode, about 20% Z bosons decay by neutral leptonic mode while 10% times they decay in charged leptonic mode. This analysis involves a measurement of $Z\gamma$ production in neutral leptonic channel. Since the neutrinos do not carry the electric charge, they do not interact by means of electromagnetic force, only initial state radiation (ISR) contributes to $Z\gamma \to \nu\bar{\nu}\gamma$ final state. This ISR state is represented by Figure 3.2 (a). Since a Z boson and a photon do not self-interact at the tree level in the SM, the triple gauge $ZZ\gamma$ and $Z\gamma\gamma$ couplings are zero at the SM as previously mentioned in subsection 3.1.1. The tree level diagrams of $Z\gamma$ processes which are forbidden in SM are represented on Figure 3.2 (b) and (c). The most general parametrization of

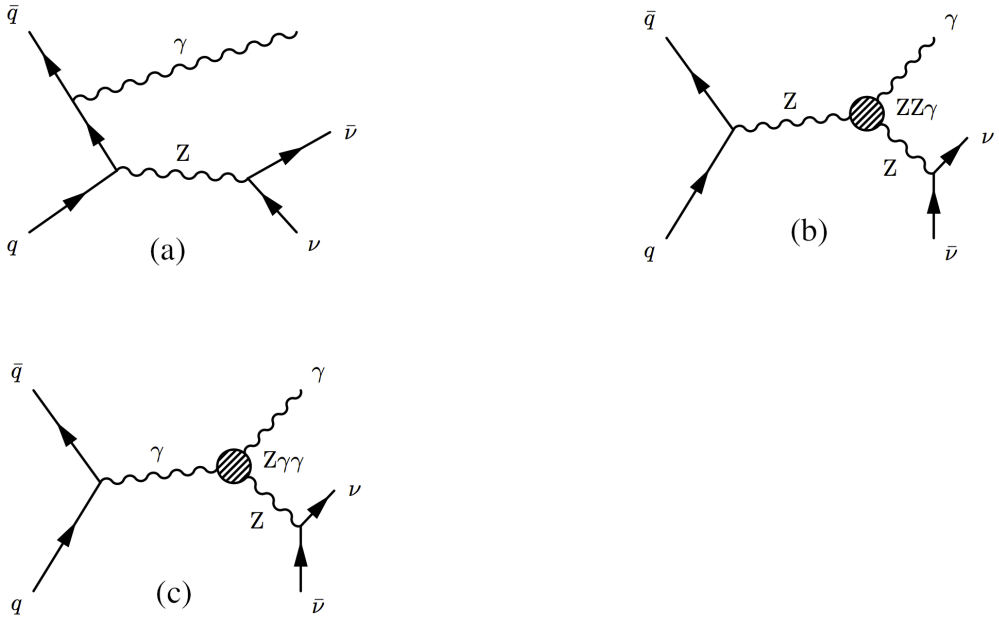

Figure 3.2: *Feynman diagrams of the $Z\gamma$ production at leading order via initial state radiation (a) and via the anomalous triple gauge coupling $ZZ\gamma$ (b) and $Z\gamma\gamma$ (c).*

interaction between a Z boson and a photon has been represented by constructing Lorentz and gauge invariant $ZV\gamma$ vertex as shown in Figure 3.3 where V represents a Z boson or a photon [29]. The $ZZ\gamma$ vertex function is Figure 3.3 is defined in equation 3.7.

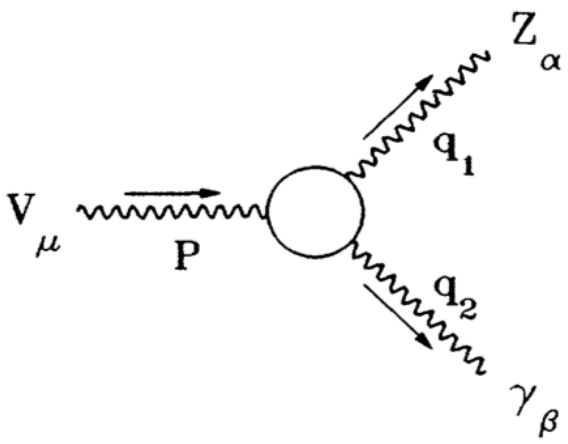

Figure 3.3: *Feynman diagram anomalous triple gauge coupling $ZV\gamma$*

$$\Gamma^{\alpha\beta\mu}_{Z\gamma Z} = \frac{P^2 - q_1^2}{m_Z^2}(h_1^Z(q_2^\mu g^{\alpha\beta} - q_2^\alpha g^{\mu\beta}) + \frac{h_2^Z}{m_Z^2}P^\alpha[(P\cdot q_2)g^{\mu\beta} - q_2^\mu P^\beta] + h_3^Z\epsilon^{\mu\alpha\beta\rho}q_{2\rho} + \frac{h_4^Z}{m_Z^2}P^\alpha\epsilon^{\mu\beta\rho\sigma}P_\rho q_{2\sigma}) \tag{3.7}$$

with $Z\gamma\gamma$ vertex obtained by the following replacements:

$$\frac{P^2 - q_1^2}{m_Z^2} \to \frac{P^2}{m_Z^2} \text{ and } h_i^Z \to h_i^\gamma,\ i = 1, ..., 4. \tag{3.8}$$

The couplings h_i^V where V = Z or γ, which represent the couplings between a Z boson and a photon, are dimensionless functions of the squared momenta of the bosons in the trilinear $ZV\gamma$ vertex (q_1^2, q_2^2 and P^2). The couplings h_1^V and h_2^V are CP-violating while h_3^V and h_4^V are CP-conserving. The combination of h_3^V (h_1^V) and $h_4^V(h_2^V)$ correspond to the electric (magnetic) dipole and magnetic (electric) quadrupole transition moment [29]. The couplings have to vanish at large value of q_1^2, q_2^2 and P^2. In $Z\gamma$ production, $q_2^2 = 0$ and $q_1^2 \approx m_z^2$. The large values of $P^2 = \hat{s}$[1] results the production of high transverse energy photon and enhancement of $Z\gamma$ cross section [30]. All these couplings are zero at tree level in the SM, and only CP-conserving ones receive a small contribution ($\approx 10^{-4}$) at the one loop level [31]. A crucial consideration while studying the aTGCs is a partial wave unitarity. A generalized dipole form factor is introduced to preserve the unitarity at high energies as

[1]where $\hat{s}$ square of center of mass energy value

represented by equation 3.9.

$$h_i^{Z,\gamma} = \frac{h_{i0}^{Z,\gamma}}{(1+\hat{s}/\Lambda^2)^n}. \tag{3.9}$$

Here, $h_{i0}^{Z,\gamma}$ is a low-energy approximation of the coupling $h_i^{Z,\gamma}$, $\hat{s}$ is the square of the invariant mass of the $Z\gamma$ system, and Λ is the form factor scale, an energy at which new physics cancels divergences in the TGC vertex [32]. In this analysis, the limit in CP-conserving parameters is set based on without form factor scale (i.e., $\Lambda \to \infty$) as it provides the results without any bias arising through the form-factor energy dependence.

3.2.2 Previous studies

The searches for anomalous $ZZ\gamma$ and $Z\gamma\gamma$ TGCs have been performed at LEP [33, 34], the Tevatron [35], [36], and the LHC [37]. No evidence for the anomalous TGCs was found and the most stringent limits on aTGCs at the highest energy are $|h_3^V| < 0.027$ and $|h_4^V| < 0.0002$ at 95% C.L measured with the ATLAS detector [38].

Chapter 4

Data, Background, Signals

4.1 Data Selection and Simulation

Events are selected from the AOD datasets reconstructed in CMSSW version 4_2. Furthermore, selections are based upon the deposition of energy in the ECAL and HCAL only[1]. The data sets skimmed for this analysis are listed in Table 4.1. At the skim level, the certified luminosity "JSON" files were applied to have only good quality events.

Data Samples
/Photon/Run2011A-May10Rerecord-v1/ADO
/Photon/Run2011A-Prompter-v4/ADO
/Photon/Run2011A-Prompter-v6/ADO
/Photon/Run2011A-05Aug2011-v1/ADO
/Photon/Run2011B-Prompter-v1/ADO

Table 4.1: *List of datasets used in this analysis.*

The trigger used for this analysis are single photon triggers, unprescaled, and are fully efficient with in the barrel region and photon p_T >145 GeV. The list of triggers applied in this analysis has been listed in Table 4.2, along with the corresponding integrated luminosity for each.

[1]Note that this skimming has been performed based on the reconstructed photons which had the ECAL anomalous signal cleaning reversed, thus giving a sample which contains both in-time and out-of-time events. These informations are required for background contamination estimates.

Trigger	Integrated Luminosity (pb^{-1})
HLT_Photon75_CaloIdVL_v1	5.962
HLT_Photon75_CaloIdVL_v2	40.69
HLT_Photon75_CaloIdVL_v3	168.2
HLT_Photon125_v1	120.1
HLT_Photon125_v2	535.3
HLT_Photon135_v1	1150.
HLT_Photon135_v2	2974.
Total	4994.

Table 4.2: *Integrated luminosity by trigger.*

4.1.1 Monte Carlo samples

This analysis requires simulated samples of not only the $Z\gamma \rightarrow \nu\bar{\nu}\gamma$ signal, but also of backgrounds from other SM processes.

The samples used are listed in Table 4.3 which has included total number of generated events and luminosity corresponding to these samples. These simulated backgrounds are from the Summer11 official production, the effect of out-of-time pileup has been included. Because the signal sample of $Z\gamma \rightarrow \nu\bar{\nu}\gamma$ events was not available in Summer11 production, this signal sample has been generated privately using official tools to maintain the consistency of the generated events. Similarly, the diboson backgrounds were generated privately by the $V\gamma$ analysis group. All these private samples are with pileup scenario since the increased instantaneous luminosity of the 2011 LHC data affects detector performance and background estimation. These samples have been reconstructed using CMSSW_4_2_3. The following parameters were used for these Monte Carlo (MC) samples:

- Center of mass energy 7 TeV
- Magnetic field 3.8 T
- Out-of-time pileup
- Detector calibration and alignment using START conditions
- Global Tag used for simulation: MC_42_V12

Process	DataSet Name	Events	Lumi. (pb^{-1})
$Z(\rightarrow \nu\bar{\nu}) + \gamma$	private production (Pythia)	100000	2630194
$Z(\rightarrow ll) + \gamma + Jets(ee$ and $\mu\mu)$	private production (Madgraph)	754839	54738.1
$W(\rightarrow l\nu) + \gamma + Jets$	private production (Madgraph)	1062987	49649.1
W$\rightarrow e\nu$	/WToENu_TuneZ2_7TeV-pythia6/ Summer11-PU_S3_START42_V11-v2/AODSIM	5304113	671
W$\rightarrow \mu\nu$	/WToMuNu_TuneZ2_7TeV-pythia6/ Summer11-PU_S3_START42_V11-v2/AODSIM	3954916	500
W$\rightarrow \tau\nu$	/WToTauNu_TuneZ2_7TeV-pythia6/ Summer11-PU_S3_START42_V11-v2/AODSIM	3999901	506
Photon+Jet	/G_Pt30to50_TuneZ2_7TeV_pythia6/ Summer11-PU_S3_START42_V11-v2/AODSIM	2177187	130.41
	/G_Pt-50to80_TuneZ2_7TeV_pythia6/ Summer11-PU_S3_START42_V11-v2/AODSIM	2016427	740.83
	/G_Pt-80to120_TuneZ2_7TeV_pythia6/ Summer11-PU_S4_START42_V11-v1/AODSIM	1625917	3635.80
	/G_Pt-120to170_TuneZ2_7TeV_pythia6/ Summer11-PU_S3_START42_V11-v2/AODSIM	2066070	24546.00
	/G_Pt-170to300_TuneZ2_7TeV_pythia6/ Summer11-PU_S4_START42_V11-v1/AODSIM	1496472	66098.20
	/G_Pt-300to470_TuneZ2_7TeV_pythia6/ Summer11-PU_S3_START42_V11-v2/AODSIM	2070808	$1.38715e06$
	/G_Pt-470to800_TuneZ2_7TeV_pythia6/ Summer11-PU_S3_START42_V11-v2/AODSIM	2050475	$1.55002e07$
Diphoton (Born)	/DiPhotonBorn_Pt-25To250_7TeV-pythia6/ Summer11-PU_S4_START42_V11-v2/AODSIM	532860	23820.3
	/DiPhotonBorn_Pt-250_7TeV-pythia6/ Summer11-PU_S4_START42_V11-v2/AODSIM	526156	$6.517478e+07$
Diphoton (Box)	/DiPhotonBox_Pt-25To250_7TeV-pythia6/ Summer11-PU_S4_START42_V11-v2/AODSIM	510284	41251.7
	/DiPhotonBox_Pt-250_7TeV-pythia6/ Summer11-PU_S4_START42_V11-v2/AODSIM	256518	$1.23325e+09$
QCD	/QCD_Pt-30to50_TuneZ2_7TeV_pythia6/ Summer11-PU_S3_START42_V11-v2/AODSIM	4919871	0.092
	/QCD_Pt-50to80_TuneZ2_7TeV_pythia6/ Summer11-PU_S3_START42_V11-v2/AODSIM	4907406	0.77
	/QCD_Pt-80to120_TuneZ2_7TeV_pythia6/ Summer11-PU_S3_START42_V11-v2/AODSIM	4827473	6.15
	/QCD_Pt-120to170_TuneZ2_7TeV_pythia6/ Summer11-PU_S3_START42_V11-v2/AODSIM	4872513	42.32
	/QCD_Pt-170to300_TuneZ2_7TeV_pythia6/ Summer11-PU_S3_START42_V11-v2/AODSIM	4953963	204.17
	/QCD_Pt-300to470_TuneZ2_7TeV_pythia6/ Summer11-PU_S3_START42_V11-v2/AODSIM	4938811	4226.65
	/QCD_Pt-470to600_TuneZ2_7TeV_pythia6/ Summer11-PU_S3_START42_V11-v2/AODSIM	3934921	56033.70

Table 4.3: *Details of the simulated samples used for signal/background analysis.*

- For Jet Energy Correction(JEC) *L1FastJet*, *L2Relative* and *L3Absolute* corrections are applied on particle flow jets.

The various backgrounds listed in Table 4.3 could mimic the γ and E_T^{miss} as final state in the following ways:

- $W(\rightarrow l\nu) + \gamma$ production is a background to $\gamma + E_T^{miss}$ when the charged lepton is lost.
- Inclusive $W(\rightarrow l\nu)$ production where the lepton fakes a photon.
- $Z(\rightarrow ll) + \gamma$ could also give a rise to a $\gamma + E_T^{miss}$ signature if one of lepton is lost, yielding E_T^{miss}.
- $\gamma +$ jet events will appear as $\gamma + E_T^{miss}$ events, if the jet is mismeasured or lost.
- Diphoton production, in which one photon is mismeasured or lost.

$Z\gamma \rightarrow \nu\bar{\nu}\gamma$ Signal Simulation

The $Z\gamma \rightarrow \nu\bar{\nu}\gamma$ signal events are simulated with a combination of the results from PYTHIA and BAUR MC event generators. The two event generators are combined to take advantage of their different strengths. MC generators can be divided into two categories which are full event generators and matrix element generators. BAUR performs an exact matrix element calculation for a simulated event and includes next-to-leading-order (NLO) contributions where as hadronization or underlying events are not included. While PYTHIA is used to simulate hadronization and underlying event information, but the interactions only include leading-order (LO) contributions to the cross section. This means PYTHIA is a full event generator and BAUR is a matrix element generator. The NLO contributions are expected to be important at the LHC energy scale. For this analysis, PYTHIA generated the full events including hadronization and underlying event information, but the contribution of NLO events compared to LO events (the k-factor) is computed with BAUR. The BAUR generator uses the parton distribution functions (PDFs) for NLO and LO simulation which

are CTEQ66, CTEQ6L1 respectively. The k-factor that scales the cross section is produced by generating NLO and LO-level $Z(\nu\bar{\nu})\gamma$ events using BAUR with the selection criteria to match with the PYTHIA samples: $p_T^{\gamma} > 130$ GeV and $|\eta^{\gamma}|$ <10 without E_T^{miss} requirement but the rest of the other generator-level informations are listed in Table 4.4. The resulting k-factor is 1.56 and nearly flat as shown in Figure 4.1. Hence, this k-factors has been implemented to scale the PYTHIA $Z(\nu\bar{\nu})\gamma$ cross section from LO to NLO as a cross check with respect to measured NLO cross section for $p_T^{\gamma} > 130$ GeV. Furthermore, the k-factor, the LO and NLO $Z(\nu\bar{\nu})\gamma$ sets are generated with BAUR and the event selection criteria is applied as in Table 4.4. The photon p_T spectra for 375295 LO events and 474507 NLO events with full η coverage for the final state particles is shown in Figure 4.2. No η cut was imposed so as to obtain the k-factor for the entire kinematic range. The k-factor is then calculated as the ratio of the p_T spectrum of the NLO simulated set to the p_T spectrum of the LO simulated set. The k-factor, averaged over the p_T range is 1.246.

The effect of restricting to the fiducial range $\eta < 1.4442$ with 262366 for LO events and 317253 NLO events, which results in a k-factor of 1.190 averaged over the p_T range is shown in Figure 4.3. Since the BAUR MC does not have hadronization, the correction on the k-factor due to the track and jet p_T cuts are estimated by using the $Z(ee)\gamma$ samples from both data and MC, as described in the subsection 4.2.5. The effect of imposing the track and jet vetoes reduces the efficiency by a factor of about 0.9, comparing data to MC. Using this ratio, the k-factor scales down from 1.19 to 1.08.

Parameter	**Cut**
Photon p_T	145 GeV
E_T^{miss}	130 GeV
Cluster(Z,γ) transverse mass	100 GeV
Soft divergence parameter	0.01
Collinear divergence parameter	0.001
Fraction of hadronic energy in a cone around γ	0.15
Factorization scale	$\sqrt{\hat{s}}$

Table 4.4: *Generator-level cuts in* BAUR *MC where the photon η is restricted and jet and track veto are used.*

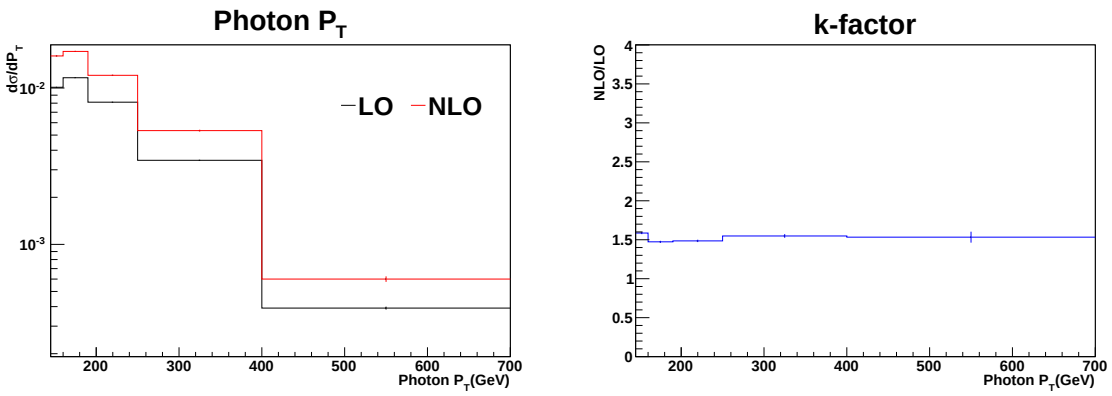

Figure 4.1: *On the left the generator level p_T spectrum for both LO and NLO events, scaled by event count and cross section. (Right) The k-factor produced by the two p_T spectra. The events were generated with $p_T > 130$ GeV to match the generator-level* PYTHIA *requirements. The k-factor is 1.56.*

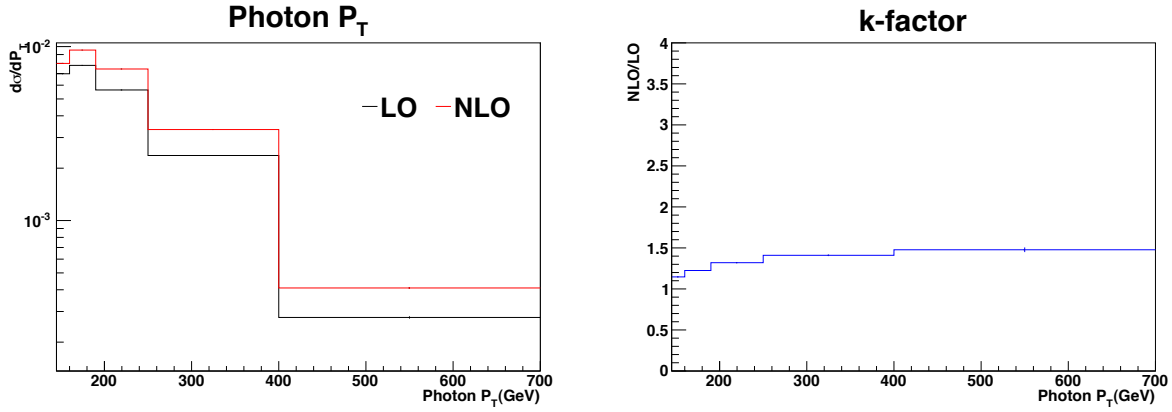

Figure 4.2: *On the left, the generator level p_T spectrum for both LO and NLO events, scaled by event count and cross section. On the right, the k-factor produced by the two p_T spectra. No η cut was imposed in the generation of these events. The k-factor is 1.26.*

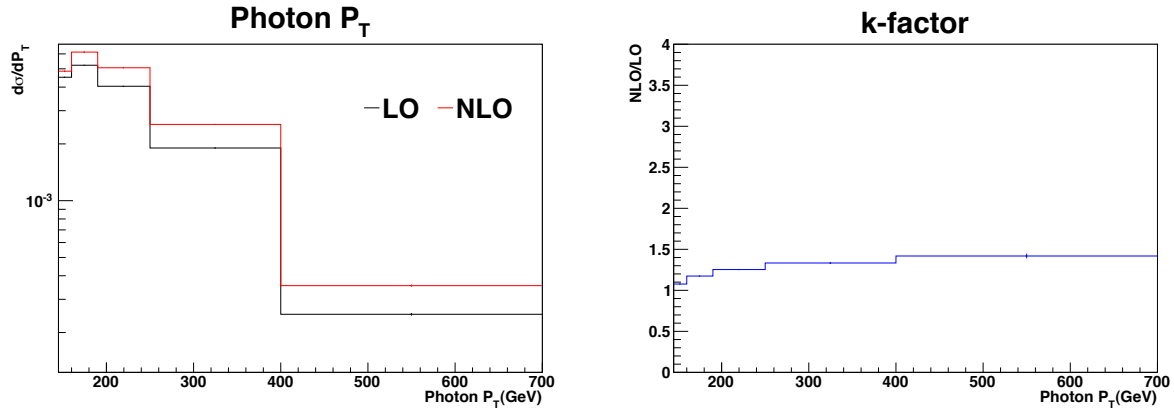

Figure 4.3: *On the left, the generator level p_T spectrum for both LO and NLO events, scaled by event count and cross section. On the right, the k-factor produced by the two p_T spectra. A cut of $|\eta(\gamma)| < 1.4442$ was imposed in the generation of these events. The k-factor is 1.19.*

The p_T and k-factor distributions from Figure 4.3 show how many $Z(\nu\bar{\nu})\gamma$ events are expected for NLO vs. LO. The k-factor is computed for each p_T bin and includes the uncertainty introduced by the PDF, as listed in Table 4.5. The last p_T bin suffers from poor statistics, so averaging over the first 4 bins provides an uncertainty of ± 0.2, which is by far the dominant error in the k-factor. The sensitivity of the k-factor to the factorization scale, set to $\hat{s}$ in this study, was tested. The factorization scale was changed to $\frac{1}{2}\hat{s}$ and $2\hat{p_T}$ producing k-factors of 1.10 and 1.15, respectively, which shows that the choice of factorization scale introduces an error of ~ 0.05 on the k-factor. Also, to test the sensitivity of the k-factor to the renormalization scale, α_S, is varied by 10%, the corresponding change in the k-factor is $\pm$ 0.02.

p_T bin (GeV)	k-factor	uncertainty from PDF
145 - 160	1.08	± 0.18
160 - 190	1.17	± 0.14
190 - 250	1.25	± 0.23
250 - 400	1.33	± 0.24
400 - 700	1.42	± 0.65

Table 4.5: *K-factors as a function of p_T. Also listed are uncertainties in these k-factors due to the uncertainty of the PDF.*

4.1.2 Monte Carlo samples with anomalous TGC

The SHERPA generator provides complete hadronic final states in the simulations of high-energy particle collision. It also covers particle production at tree level in the SM and in models beyond SM. Hence, it has been used to generate anomalous TGC (aTGC) signal for $Z\gamma + njets$ where $n \leq 1$. The generated signal is then passed through the simulation and reconstruction chain of CMSSW 4_2 (with SHERPA$-1.2.2 - cms6$) and is divided in two p_T bin - from 130 to 300 GeV/c and above 300 GeV/c. Fast simulation is used with FlatDist10_2011EarlyData_50ns pileup profile for several different values of aTGC parameters, including the SM parameters. The SM sample was compared to the one generated with $PYTHIA$ and processed with full simulation. The two samples were found to be identical for purpose of this study, which justifies the use of FastSim for the samples aTGC parameters [7]. The grid of the aTGC parameters corresponds to the nine possible combination of $h_3 = (-0.0025, 0.0, 0.0025)$ and $h_4 = (-0.000013, 0.0, 0.000013)$. The sample with $h_3 = h_4 = 0.0$ corresponds to the SM process. The cross section calculation is performed by SHERPA at LO and is corrected with k-factor from BAUR, namely 1.19, based on the complete analysis selection except jet and track veto as mentioned in subsection 4.1.1.

4.1.3 Photon identification

In order to separate real photons from jets, several discriminating variables are constructed by combining the information from the calorimeters and the inner tracking system. The calorimeter information is used to select events containing a high p_T EM shower. Track isolation is used to further reduce remaining fake photons from high p_T neutral particle like π^0. Hence, isolation and identification requirements are applied to enhance the purity of the photon sample. The selection criteria and the cut values have been adjusted on the basis of the MC simulation to maximize the background rejection by keeping the efficiency flat as a function of η and photon E_T. The following variables are used to identify the photon candidates.

- Pixel seed veto: The supercluster is required not to match pixel hits[2] consistent with a track from the interaction region.

- ECAL isolation: The sum of ECAL E_T around the photon candidate in an annular region of inner radius $\Delta R = \sqrt{(\Delta\eta)^2 + (\Delta\phi)^2} = 0.06$ and the outer radius 0.4, but excluding a strip of 0.05 extending in ϕ.

- HCAL isolation: The sum of HCAL E_T around the photon candidate in an annular region of inner radius $\Delta R = 0.15$ and the outer radius of 0.4.

- Track isolation: The scalar sum of tracks p_T which are consistent with the primary vertex in a hollow cone around the photon candidate in an annular region of inner radius of $\Delta R = 0.04$ and outer radius 0.4, but excluding a strip of 0.05 extending in ϕ.

- H/E: Ratio of hadronic energy within a cone of $\Delta R = 0.15$ behind the supercluster to the total supercluster energy.

- $\sigma_{i\eta i\eta}$: A log energy weighted measure of the spread in η of 5×5 array of crystal centered on the seed crystal is given as:

$$\sigma^2_{i\eta i\eta} = \frac{\sum_i^{5\times5} w_i (i\eta_i - i\eta_{seed})^2}{\sum_i^{5\times5} w_i}, \; w_i = max\left(0, 4.7 + ln\frac{E_i}{E_{5\times5}}\right). \tag{4.1}$$

  where i goes over each of the crystals within a 5×5 array of crystals centered on the seed, and E_i is the energy of the ith crystal. Hence, $\sigma_{i\eta i\eta}$ measures the transverse profile of the EM shower and its requirement to be less than 0.013 for central region of the ECAL ensures that the EM shower is consistent with the shape expected from a photon.

[2]To reconstruct an electron, the supercluster must be matched with the track. This is done by extrapolating the probable position of the tracker hits from supercluster's position.

Variables	Threshold
pixel seed	require none
ECAL Isolation	$< 4.2 + 0.006 * p_T^\gamma$
HCAL Isolation	$< 2.2 + 0.0025 * p_T^\gamma$
Track Isolation	$< 2.0 + 0.001 * p_T^\gamma$
H/E	< 0.05
$\sigma_{i\eta i\eta}$	< 0.013
t_{seed}	3 ns

Table 4.6: *Selection criteria for barrel photon identification.*

- Cluster seed time: The seed of the supercluster should be within a window of time consistent with the collision vertex. In other words, the timing of the photon as measured by seed of the supercluster in ECAL is required to be consistent with that of particles originating from a collision.

4.1.4 Event selection

The events in data, which have γ+E_T^{miss} as a final state, have to pass the unprescaled high E_T photon triggers listed in Table 4.2.

Further, each event is required to have at least 25% of the tracks should satisfy the good quality criteria; this selection removes "scraping" events[3]. Events are also need to have at least one good primary vertex with a number of degrees of freedom >4, $|z| < 24$ cm, and $\rho < 2$ cm of the center of the CMS detector. It is required to have one photon object with at least 145 GeV of transverse momentum and should lie in the barrel fiducial region of the detector($|\eta| < 1.4442$). High E_T photons are reconstructed based on the clusters (formed by the superclustering (SC) algorithm) of crystals within the ECAL, as mentioned in subsection 2.4.1, and Ref. [39],[17].

Backgrounds arising in the data are from misidentifying jets and electrons as photons. A jet can fake a photon if a neutral particle such as π^0 (or η) within the jet carries a significant fraction of the p_T and the photons from its subsequent decay are collimated so that they

[3]Events with fewer than 10 tracks are considered not-scraping as well.

appear as a single photon in ECAL. Because of inefficiency in the track reconstruction, electrons can be misreconstructed as photons. To reduce the effect due to jets and electrons misidentified as photons, there are additional requirements such as isolation variables, shower width, and pixel match seed match calculated for the photon as listed in subsection 4.1.3 have been implemented.

Usually, the isolation of the photon within the tracking volume is computed using tracks which originate from the primary vertex [40]. Due to the higher pileup scenario of existing dataset, an additional track isolation is computed with respect to each vertex in the event. The largest value of this isolation is then assigned and required to be smaller than the standard track isolation requirement, so as to ensure this electromagnetic object is indeed isolated from any charged hadron activity.

In this analysis, the PF E_T^{miss} [20] has been used. Since neutrinos do not deposit energy in the detector, resulting the momentum imbalance in the event. E_T^{miss} is defined as the magnitude of the vector sum of the transverse momentum of all of the reconstructed objects in the events as mentioned in section 2.7. Hence, events are required to have $E_T^{miss} > 130$ GeV to minimize the uncertainty due to modeling of E_T^{miss} in this analysis.

The beam halo muons or cosmic rays that can induce bremsstrahlung and produce showers in the ECAL. The photons emitted by such processes and anomalous signal, which has been discussed in the subsection 4.3.1, can be misidentified as the ISR photons which are produced during pp collisions. To minimize these contributions, the events are required to pass the following criteria:

- Non Spike[4]:
  - $\sigma_{i\eta i\eta} > 0.001$
  - $\sigma_{i\phi i\phi} > 0.001$
  - The largest intracluster time difference (LICTD) between crystals with more than 1 GeV deposited must have an absolute value less than 5 ns.

[4]Detail about spike is in subsection 4.3.1

- R9 < 1

- Beam Halo/non Cosmics:

  - Seed crystal time is required to be within 3 ns of prompt window (defined as 0 ns in the ECAL).

  - Events are rejected if a CosmicMuon[5] is reconstructed in the muon detectors. This criteria discriminates against both cosmic ray bremsstrahlung and beam halo muon bremsstrahlung.

The $Z\gamma$ and γ+jet events are vetoed to reduce the contribution from $W\gamma$. This is done by rejecting the event if there is a jet reconstructed with p_T above 40 GeV with in $|\eta| < 3.0$ and if there is a track with p_T above 20 GeV that is $\Delta R > 0.04$ away from the photon candidate. By plotting the distribution of all ΔR values between the tracks in a MC event and the photon candidate (Figure 4.4), it can be seen that the most of the tracks within ΔR of 0.04 are associated with the object itself; the spike in the $W(e\nu)$ sample is from the electrons and early conversions will produce tracks within ΔR of 0.04 of the $Z(\nu\bar{\nu}) + \gamma$ photon candidate. Conversely, events with tracks outside of this ΔR value are are likely to be extraneous to our signal and should be vetoed. Hence, ΔR within 0.04 leads with a clean signal sample.

4.2 Selection Efficiencies

4.2.1 Trigger Selection

The monophoton event has been selected from the unprescaled single photon triggers listed in Table 4.2. With the increase in instantaneous luminosity, the single photon trigger threshold also increases to control the trigger rate. Hence, an offline p_T threshold above the highest trigger threshold is used. The relative trigger efficiencies are calculated using

[5]CosmicMuon refers to the reconstructed muons in which the individual segments within the muon system are not required to be projective.

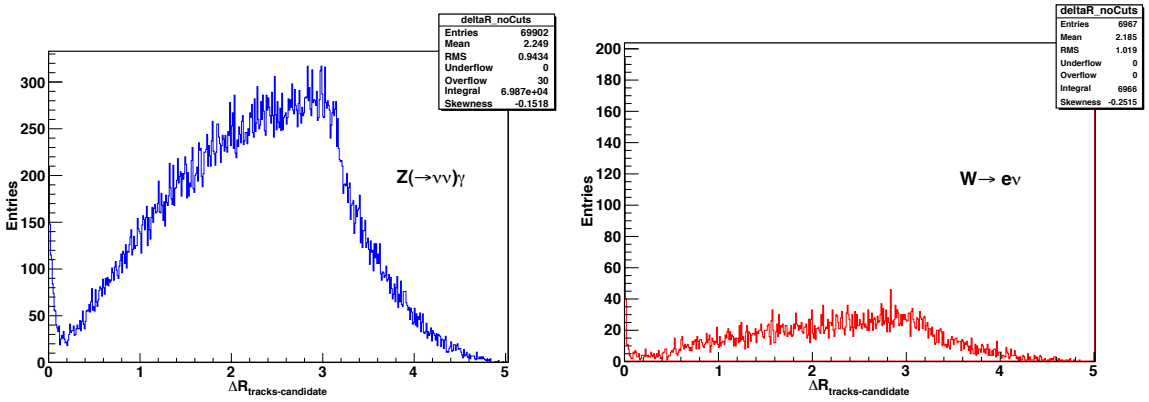

Figure 4.4: *The ΔR values between all the tracks and the candidate photon in the MC $Z(\nu\bar{\nu})$ (left) and $W(e\nu)$ (right) sample events. The bin size of ΔR is 0.01.*

backup triggers which are included at the HLT to assess the relative efficiency of the different components of triggers with respect to the offline selection criteria.

The trigger is composed of both an L1 component (L1SingleEG20) and HLT. Since the offline energy threshold is 145 GeV, it can be assumed that the full L1 efficiency is attained before the successive analysis cuts. Hence, only the turn-on curve of the HLTs with respect to offline selection need to be determined. At the HLT, three selections are used: a threshold (75, 125, and 135 GeV respectively for the used triggers), isolation cuts (looser than the used offline selection), and a very loose selection on shower shape[6]. The selection on shower shape "CaloIdVL" is very loose compared to the offline selection, and is also loose compared to the shape expected from electromagnetic objects. Also, it is even loose enough to include many of beam halo (showers which are typically twice as wide in η and can still pass this trigger). Hence, CaloIdVL portion is considered to fully efficient[7].

For the energy threshold, prescaled backup triggers which have the same selection criteria (CaloIdVL) are analyzed concurrently with the unprescaled triggers used for the signal selection. This allows to observe the turn on curve for the trigger at HLT by measuring the

[6]shower shape corresponds to transverse profile of the EM shower and is denoted by $\sigma_{i\eta i\eta}$.

[7]While some portions of the HLT reconstruction differ significantly from the offline reconstruction (i.e. regional calorimeter reconstruction, different track isolation, etc), the core of the shower used in the calculation of the shower shape must still be comparable to what is found offline, which gives further confidence in this statement.

efficiency with respect to the lower threshold trigger. Furthermore, the tight photon candidates[8] in the events are explicitly required to pass the lower threshold triggers with a E_T^{miss} requirement of p_T >130 GeV. Those tight photon candidates constitute the denominator. While in the numerator part, it also requires that those photons should pass the unprescaled single trigger. The "turn on curve" for the trigger at HLT can be formed, by measuring the efficiency of the unprescaled trigger with respect to the lower threshold trigger.

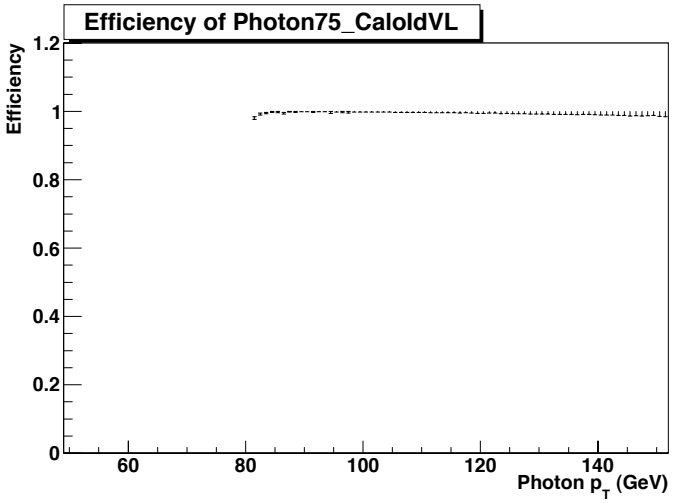

Figure 4.5: *Efficiency of single photon trigger HLT_Photon75.*

The unprescaled single triggers for selecting monophoton events are fully efficient with respect to the offline selection criteria p_T cut of 145 GeV as shown in Figure 4.6 and Figure 4.7. Hence, a conservative 2% uncertainty is assigned to trigger efficiency such that data vs. MC correction factor corresponding to trigger efficiency is 1.00 ± 0.02.

4.2.2 Photon Identification efficiency

The tag and probe (TP) method uses $Z \to ee$ events as a high-purity source of unbiased electron to extract efficiencies. This standard method was used to verify the photon identification (ID) efficiency in data. The detector requirements for photon ID were designed to be similar to those of electron ID with the exception of the pixel seed veto. An overview of

[8]Photon candidates need to satisfy the conditions in Table 4.6.

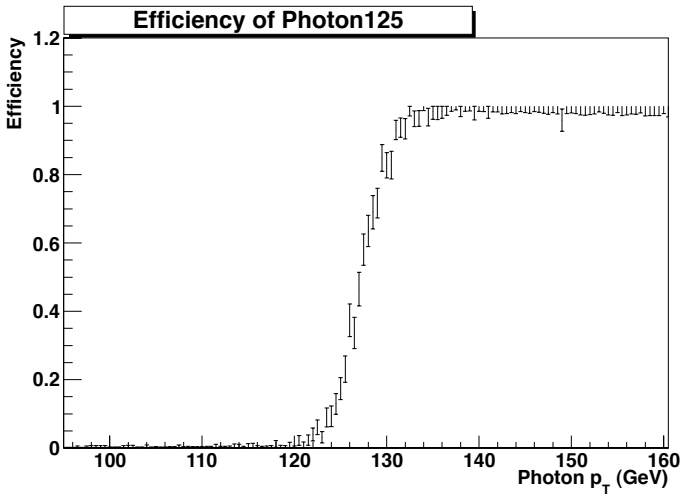

Figure 4.6: *Efficiency of single photon trigger HLT_Photon125.*

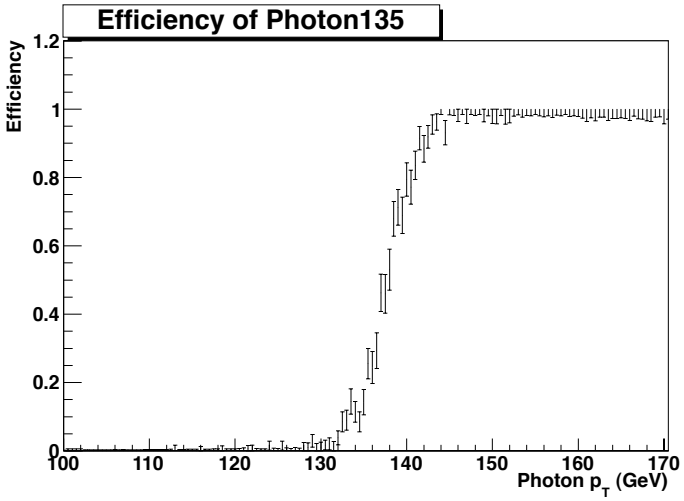

Figure 4.7: *Efficiency of single photon trigger HLT_Photon135.*

this method has been explained briefly, more detail is found in this link [41].

Tag and probe is a method of using the redundant identification of electrons (e.g. both tracker and ECAL information) to estimate the efficiency of photon selection criteria in data vs. MC. By placing stringent requirements on one "leg" of the Z decay, the efficiency has been measured. This electron, which is known as "tag", is required to pass the trigger and has a track associated with it, and be generally very high quality i.e.; should pass tight electron ID. The other "leg" of the Z is reconstructed as only a track or a supercluster (this is commonly called as the "probe"), and then the invariant Z mass is calculated taking these tag and probe pair. Two separate invariant mass distributions are made, one is for the condition (i) when the probe passes the identification criteria, the other is for the condition (ii) when the probe fails. Both distributions are fit to subtract the multijet QCD background. Finally, the efficiency is calculated, in the bins of either p_T or η. The same method has been repeated on MC as performed for the data. The fits for the sample of probes with $p_T > 145$ are shown in Figures 4.8 and 4.9.

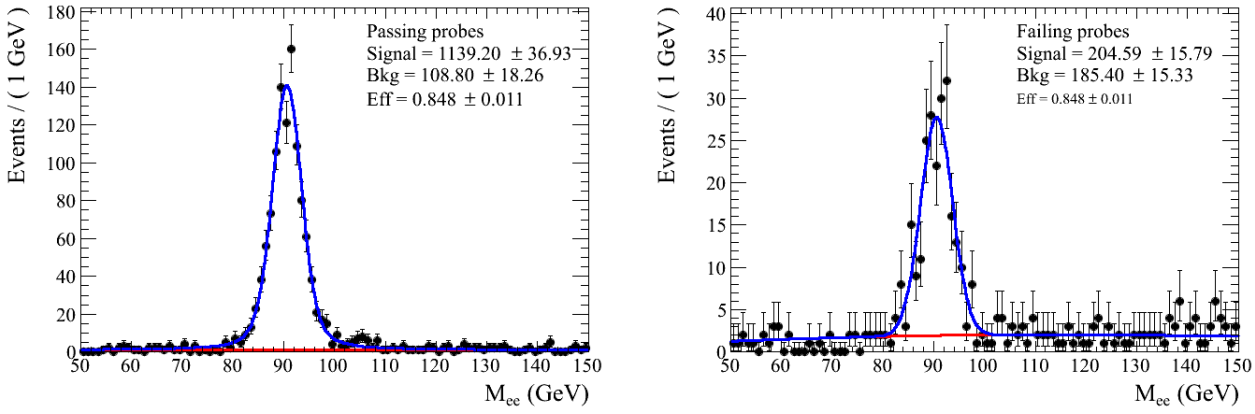

Figure 4.8: *Invariant mass and fits for tag and probe method applied to data.*

The correction factor corresponding to the photon ID efficiency has been measured to be 0.96 ± 0.02. This is correction factor has also included in the final systematic uncertainty of the efficiency.

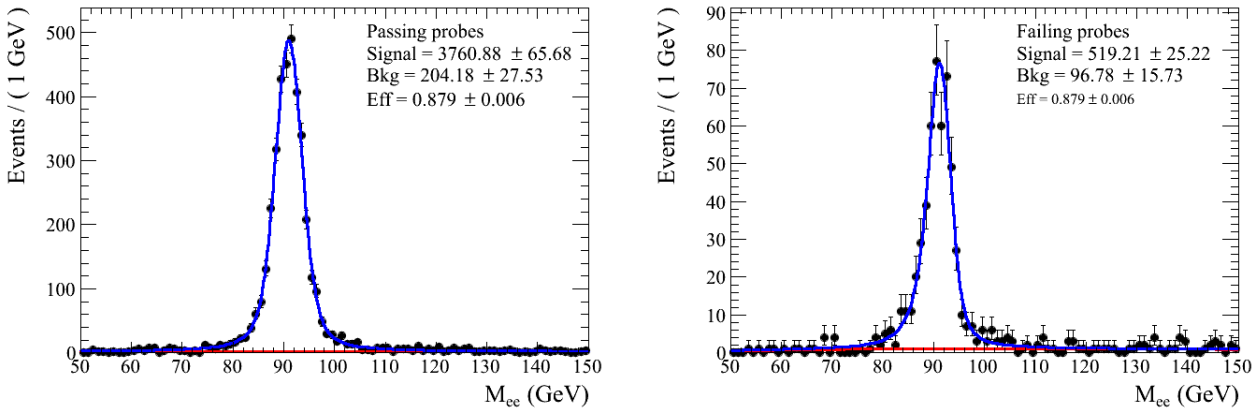

Figure 4.9: *Invariant mass and fits for tag and probe method applied on Monte Carlo.*

4.2.3 Embedded Spike Removal

Anomalous calorimeter signals (detail information is in subsection 4.3.1) may be "embedded" within prompt clusters of energy from collisions. The crystals with energy more than 1 GeV are clustered into a photon candidate and are also required to be within 5 ns of the seed crystal's time to remove such anomalous signal. This time difference between each crystal in the cluster and seed crystal's time is called as largest intra-cluster time difference (LICTD). This LICTD requirement ensures that the energy deposition is consistent both in the pattern of the energy deposition and in the timing with real photon candidates from collisions.

To calculate its efficiency on real photons, the combined anti-spike cuts (LICTD and R9) as mentioned in subsection 4.1.4 is implemented in data sample for $W(e\nu)$ candidates. The $W(e\nu)$ candidates are required to pass the regular candidate requirements beside a pixel seed requirement and no jet as well as track vetoes. Then impose $|LICTD| < 5$ ns as well as the $R9 < 1$ requirements, the ratio of events in the sample that pass either of these two requirements with respect to entire sample has been calculated. This gives the LICTD+R9 efficiency ϵ, and it has been mentioned in Table 4.7. Since the MC is fully efficient, ϵ is equal to the $\frac{\text{data}}{\text{MC}}$ scale factor (SF).

The efficiency of the LICTD requirement alone has also been calculated with a data sample of $Z \to ee$ candidates. The $Z \to ee$ candidates pass the regular candidate selection

and satisfy a pixel seed requirement. To calculate the efficiency for the LICTD requirement both electrons in the event are required to pass this LICTD criteria. The $Z \to ee$ candidate sample yields an efficiency of 98.3% per electron for the LICTD criteria. This result is also cross checked using $W(e\nu)$ data sample and found to be in complete agreement with the one done with $Z \to ee$ event. Hence the correction factor corresponding to LICTD requirement is 0.983 ± 0.009.

Cut Efficiency	$W(e\nu)$ MC	$W(e\nu)$ Data	$W(e\nu)$ MC (ignore jet+trk)	$W(e\nu)$ Data (ignore jet+trk)
LICTD	0.98 ± 0.19	0.94 ± 0.05	0.99 ± 0.13	0.94 ± 0.04
R9	1.00 ± 0.19	1.00 ± 0.06	1.00 ± 0.13	1.00 ± 0.04
LICTD+R9	0.98 ± 0.19	0.94 ± 0.05	0.99 ± 0.13	0.94 ± 0.04

Table 4.7: *Efficiency of R9 and LICTD cuts.*

4.2.4 Veto Efficiency

The requirement of vetoes on candidate events reduces the backgrounds such as $W\gamma$ which has a lepton in addition to a photon and E_T^{miss} and γ+jet which has a jet besides a photon and potentially mismeasured as E_T^{miss}. Furthermore, vetoing on reconstructed muons (CosmicMuons) can also reduce potential backgrounds from both beam halo and cosmic rays.

The three vetoes, which are vetoes on (i) reconstructed cosmic muons (ii) jets $p_T >$ 40 GeV within $|\eta| < 3.0$ (iii) tracks $p_T > 20$ GeV that are $\Delta R > 0.04$ away from the photon candidate object, are studied. The jet and track vetoes are considered to be correlated since both jet and track veto remove events with jet activity. Hence, the combined studies have been done on these vetoes. The efficiency of vetoing an event that has jets or tracks is computed along with the efficiency of vetoing events with cosmic muons.

Jet and track veto efficiency is measured from a $W \to e\nu$ sample both in data and MC. It is not necessary that the efficiency of $W \to e\nu$ and $Z\gamma \to \nu\bar{\nu}\gamma$ to be the same for the comparison between the data and the simulation to scale MC to better match the data. This is because the $W \to e\nu$ candidate data sample includes many backgrounds, these vetoes will eliminate a larger fraction of these events compared to the other two samples.

To select the events for this analysis, the selection mentioned in subsection 4.1.4 is used. For the MC, the beam scraping cleaning and trigger were not applied. Furthermore, the MC is re-weighted to account for pileup as described in section 5.3. No uncertainty has been assigned to the weight factors, so the uncertainties shown are only statistical. The $W \to e\nu$ MC and data event selection is identical to the monophoton sample with the exception that a pixel seed is required to identify the electron. The numerator and denominator for the computation of a particular veto efficiency has shown in Table 4.8, while the veto efficiency is shown in Table 4.9.

Cut Set	$W(e\nu)$ MC	$W(e\nu)$ Data	$Z(\nu\bar{\nu})\gamma$ MC	Cand Data
Numerator for N-1 Eff.	48	583	938	73
Denominator for Cosmic-Muon Eff.	54	653	995	121
Denominator for Trk+Jet Eff.	107	1198	1344	218

Table 4.8: *Number of candidates.*

Efficiency	$W(e\nu)$ MC	$W(e\nu)$ Data	$Z(\nu\bar{\nu})\gamma$ MC	Cand Data
CosmicMuon Eff.	0.90 ± 0.17	0.89 ± 0.05	0.94 ± 0.04	0.60 ± 0.09
Trk+Jet Eff.	0.45 ± 0.07	0.49 ± 0.02	0.70 ± 0.03	0.33 ± 0.05

Table 4.9: *N-1 efficiencies.*

There is the discrepancy between $W(e\nu)$ and $Z(\nu\bar{\nu})\gamma$ for jet and track efficiency since the topologies of jets are different for these two processes. The explanation for the difference in jet and track efficiency is as follows: The W boson is likely recoiling off of a jet, while the Z boson is recoiling against the photon as the result of which there is probability of more events get eliminated with a jet veto in W sample in compare to that in the Z sample. Taking this into account with the $W(e\nu)$ result, the final Jet and track data-to-MC factor is set to 1.0 ± 0.1. The conservative 10% uncertainty has been assigned to jet and track veto. A study has also performed where $Z(ee)\gamma$ sample from data is used to estimate the efficiency ratio since this sample is similar in topology to the $Z(\nu\bar{\nu})\gamma$. The detail study of jet veto from $Z(ee)\gamma$ sample is in subsection 4.2.5. The data-to-MC factor for the $Z(ee)\gamma$

is 0.91 ± 0.01. This efficiency is consistent with being flat and is well within the systematic uncertainty of 10% assigned to the veto efficiency in the MC.

However, cosmic muons are not simulated in the MC sample, the cosmic muon veto efficiency in $W(e\nu)$ MC and data match. This is because the requirement of the pixel seed helps to eliminate cosmic muon bremsstraughlung events that occur in data. It is also expected that the $Z(\nu\bar{\nu})\gamma$ MC and candidates in data do not match for the CosmicMuon efficiency because many cosmic muon bremsstrahlung events are thrown out by this veto in data. Also, the monophoton candidates are more likely to be contaminated by cosmic event than by the $W(e\nu)$ candidates as cosmic events do not have pixel seed.

The inefficiency of vetoing only on the cosmic muons is studied using data $Z \to ee$ sample with high statistics. The $Z \to ee$ candidates are selected in the photon dataset by requiring two tight photons $p_T > 30$ GeV with pixel seed matches along with the requirement of vetoes on the jets and tracks. The invariant mass of these $Z \to ee$ candidates is shown in black in Figure 4.10. In this same figure, the red peak represents the events which also pass the CosmicMuon veto beside jet and track veto. The veto efficiency is measured from this sample to be 89.9% in data and 94.3% in MC. Hence, data-to-MC efficiency scale of 0.95 ± 0.01 has been estimated.

The difference in the efficiencies between data and MC are summarized in Table 4.10. The scale factor ρ is later used to scale the MC simulated backgrounds to correct for the difference in efficiency between the simulated and real events due to trigger, photon reconstruction and the vetoes. The cumulative value of ρ is 0.90 ± 0.11.

Source	Estimate for ρ
Trigger	1.00 ± 0.02
LICTD	0.983 ± 0.009
Photon Efficiency	0.96 ± 0.02
Jet and track veto	1.00 ± 0.10
Cosmic muons veto	0.95 ± 0.01
Total	0.90 ± 0.11

Table 4.10: *The difference in the efficiencies for selection criteria in data and simulation.*

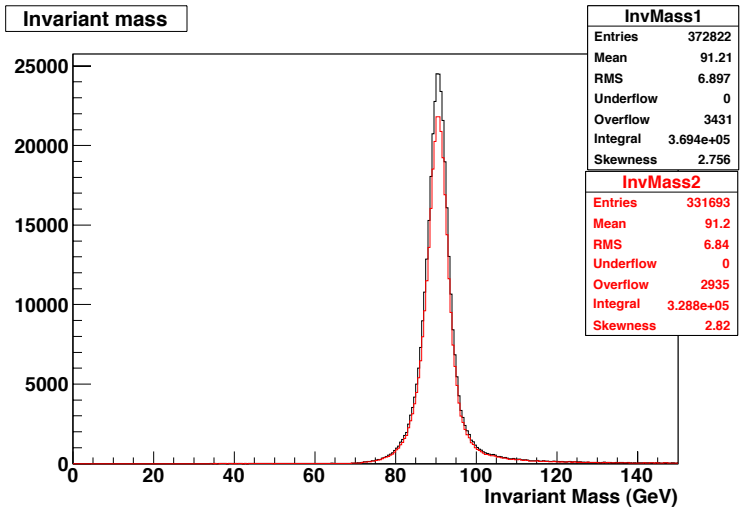

Figure 4.10: *Invariant mass for $Z \to ee$ events passing jet and track veto (black), and for those also passing CosmicMuon veto (red).*

4.2.5 Additional study for uncertainty in jet and track veto efficiency using $Z\gamma \to ee\gamma$ events

From the study of jet and track veto efficiency, this efficiency for $W \to e\nu$ in data compares well with the MC. But, these efficiencies are quite different from what is observed for $Z\gamma \to \nu\bar{\nu}\gamma$. Hence, an additional cross check has been performed between data and MC using a set of $Z\gamma \to ee\gamma$ events. The same selection criteria as mention below has been applied to both data and MC events:

- All events are required to have at least two photon-like objects, each with $E_T >$ 30 GeV, in either the barrel or endcap region, pass the same photon ID requirements of Table 4.6, except that an associated pixel match is required for the electron instead of veto the event.

- At least one photon object is required to be in the barrel of ECAL. This photon candidate is required to pass all of the photon selection requirements as that of candidate selection.

- All the electromagnetic objects have to be separated from each other by $\Delta R > 0.8$.

These events are then used to study the jet and track veto efficiency in bins of the photon E_T. The efficiency measured in data as a function of the photon E_T is shown in Figure 4.11. The corresponding efficiency for the same selection in MC is presented in Figure 4.12. The ratio of the data and MC efficiencies is shown in Figure 4.13. This efficiency, 0.91 ± 0.01, is consistent with being flat, and is well within the systematic uncertainty of 10% assigned to the veto efficiency in the MC.

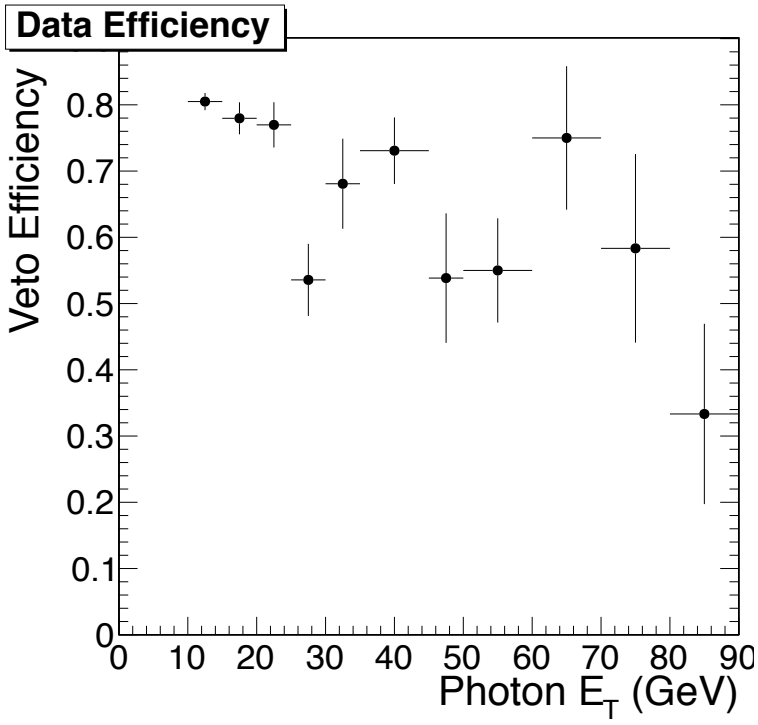

Figure 4.11: *Veto efficiency for $Z\gamma \to ee\gamma$ as measured in data events as a function of photon E_T.*

4.3 Background Estimates

The backgrounds for $Z(\nu\bar{\nu})\gamma$ signal can be separated into two categories: (i) From SM processes mimicking the monophoton signal arising from inefficiencies in detection or reconstruction. (ii) From non-collision sources such as anomalous ECAL deposits, cosmics, and beam halo. The non-collision backgrounds as well as two of the SM backgrounds (jets

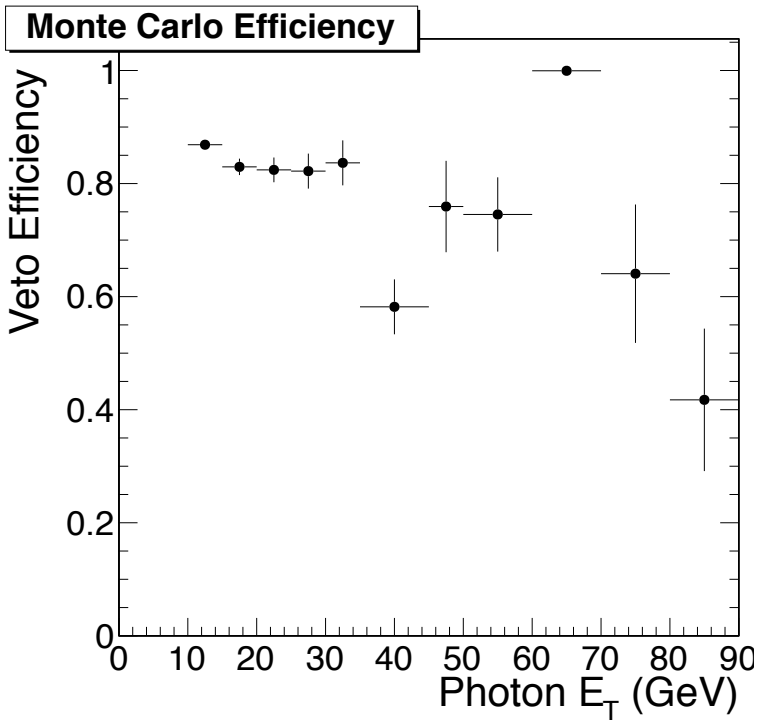

Figure 4.12: *Veto efficiency for $Z\gamma \rightarrow ee\gamma$ as measured in MC events as a function of photon E_T.*

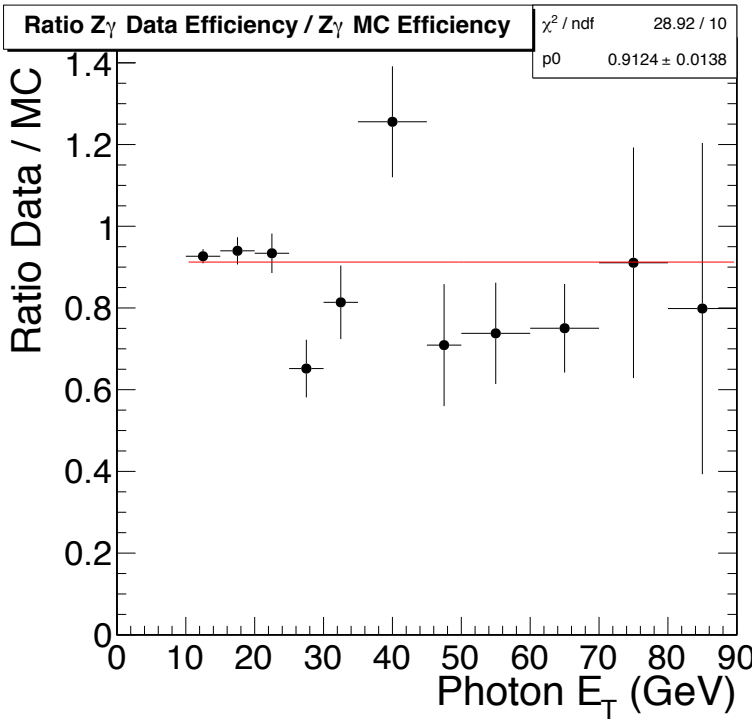

Figure 4.13: *Ratio of data efficiency for $Z\gamma \rightarrow ee\gamma$ to MC efficiency as a function of photon E_T.*

and electrons misidentify photons) are are estimated from the data. While the rest of MC backgrounds are estimated using MC.

4.3.1 Non-Collision Backgrounds

Anomalous ECAL signal and other two related to muon bremsstrahlung, which are cosmics and beam halo, are three non-collision backgrounds to the $Z\gamma \rightarrow \nu\bar{\nu}\gamma$ signal. These can be minimized by investigating their reconstruction and then making appropriate cuts. The rest of this chapter is related with the methods that have been implemented to reduce backgrounds and estimate the their contribution to $Z\gamma \rightarrow \nu\bar{\nu}\gamma$ signal.

Anomalous ECAL Signals

Anomalous signals in the barrel part of the ECAL are one of the backgrounds for detecting and measuring particles from a *pp* collisions event. Studies based on MC simulation indicate that anomalous signals originate from direct ionization of the silicon in avalanche photo-diodes from heavily ionizing particles mainly protons and heavy ions which are produced in *pp* collisions. They deposit energy in a single crystal and is often termed as "spike" [42]. This phenomenon can misidentified as a high E_T^{miss} and single photon event. Since the spikes are isolated with all energy reconstructed in a single crystal, they can be partially removed by taking the topological variable $1 - E_4/E_{seed}$. Here E_4 represents the sum of energy in 4 adjacent crystals to the seed crystal E_{seed} is the seed crystal. This topological variable is called as "swiss cross" [43]. This variable approaches unity for spike indicating a deposit of energy is localized almost entirely within a single crystal. For the true photon shower, this variable approaches to 0.8 as shown in Figure 4.14 (a). Hence, shower with "Swiss cross" greater than 0.95 are removed from photon reconstruction sequence.

The spikes are due to the particles interacting with the APD directly, not through the crystal scintillation. Also, the spikes has unusual pulse shape biases the reconstructed time to be ~ -10 ns before a typical real photon arrival as shown in Figure 4.14 (b). A timing requirement can be imposed to reduce the effect of spike. Furthermore, to remove these

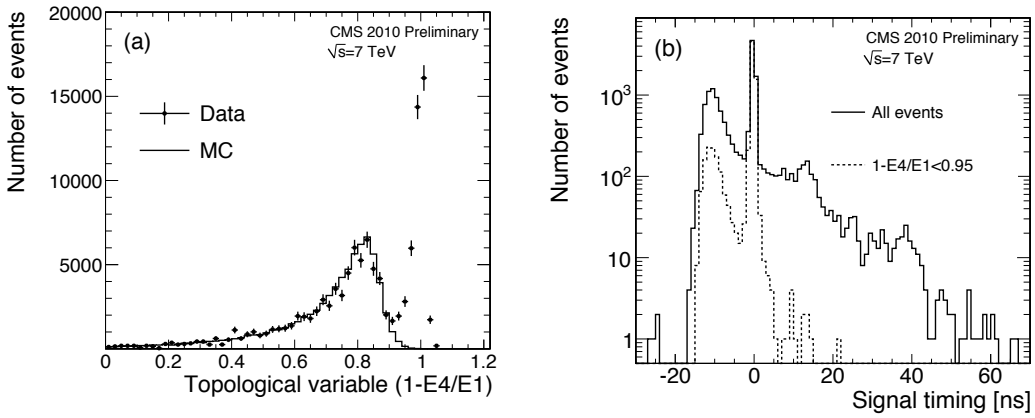

Figure 4.14: *Distribution of swiss cross variable for the highest energy deposit in each event(for the original MC photons (line) and 2010 data (points)) and reconstructed time for the seed crystal in each event. The dashed histogram is non-isolated energy deposits which pass the swiss cross cleaning,* $(1 - E4/E1) < 0.95$.

isolated spikes, the shower is required to be larger than one width of the crystal in η and ϕ direction. In order to minimize this contribution of such spikes in photon and E_T^{miss} analysis, the shower shape requirement for $\sigma_{i\eta i\eta}$ and $\sigma_{i\phi i\phi}$ should be greater than 0.001. The shower width $\sigma_{i\eta i\eta}$, which is energy weighted width, has been described by equation 4.1 and it represents the spread of shower in $i\eta$ direction. In the same way $\sigma_{i\phi i\phi}$ represents the spread of shower in $i\phi$ direction.

There may be also presence of embedded spike which occurs when the spike overlaps with a true EM shower. The embedded spikes are identified by examining the relative timing between two crystal hits. This is because spike tends to be out of time compared to the shower in which it is embedded. The largest time difference between the seed crystal and each crystal belongs to the same photon should be within the 5 ns. In other words, LICTD should be less than 5 ns. There is another discriminating parameter to reduce spike which is known as R9. This R9 parameter, whose detail information is in subsection 2.4.1, should be less than 1.

Muon Bremsstrahlung: Muon bremsstrahlung can be misidentified as a photon and missing energy event if there are no the tracks associated with the EM object. Sometime,

if a muon produces from the point of interaction and on the way of its traveling, it can deposit energy in the ECAL. In this case, photon ID criteria may remove such event from the photon and E_T^{miss} event. The photon ID requirements allow low level of track activity near the EM shower. While the cosmic ray muons can pass through the CMS detector and can undergo bremsstrahlung in the ECAL resulting faking a photon and large E_T^{miss} event because energy deposited in ECAL does not have track associated with a collision vertex.

Beam halo refers to a cloud of secondary particles traveling along with the beam bunches. This beam halo consists of muons, mesons, and baryons. These secondary particles come from collisions of beam protons with residual gas in the beam pipe and scraping the beam pipe walls. Among these halo particles, the long-lived muon is able to traverse throughout CMS [44]. Any muons in the beam halo will likely to penetrate through the layers of end cap return yoke and muon sub-detectors, thus introducing backgrounds to the most physics analyses. This analysis considers the effect of halo muon bremsstrahlung in the barrel ECAL. Such an effect could misidentify a photon originating from the interaction point. It is important to estimate this contamination as it may create fake events for searches of new physics involving rare high E_T photons.

Estimating Non-Collision Backgrounds

To estimate the monophoton events contamination due to spike, cosmic, and beam halo, their timing distributions have been studied. A special collection of photons has been created without the timing restriction of 3 ns. Monophoton candidates from this special collection are required to pass all the criteria in Table 4.6 except $\sigma_{i\eta i\eta} < 0.013$, no jet veto and CosmicMuon vetoes, and no timing requirement. that The prompt, anomalous signal, and beam halo templates are selected separately.

The prompt template is constructed in the same way as the monophoton selection as mentioned in Table 4.6 except invert the track isolation criteria to ensure that the EM objects which deposit energy in ECAL indeed are originated from the collision vertex [6]. The time template for prompt event is shown in Figure 4.15 (a).

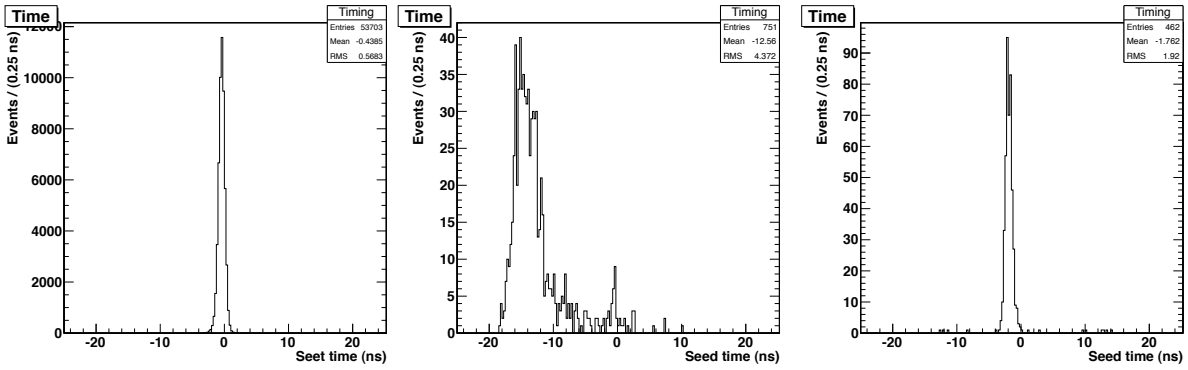

Figure 4.15: *Time templates of (a) prompt events, (b) anomalous signals, and (c) beam halo*

The anomalous signal template is created by reversing the topological shower shape requirements that ensure the showers have a spatial extent similar to a regular photon shower. In this case, $\sigma_{i\eta i\eta}$ and $\sigma_{i\phi i\phi}$ requirements have been ignored. Furthermore, reverse the swiss cross cleaning (E4/E1 < 0.05) has been implemented. This timing template for anomalous signal is shown in Figure 4.15 (b).

The beam halo template is created by requiring "taggers" which are currently used for cleaning E_T^{miss}. The tagger uses a hits in the hadronic endcap (HE) which lines up along ϕ with a supercluster in the barrel ECAL [6]. For an event to satisfy the HE tag requires:

- CaloTower HE energy > 1 GeV.
- CaloTower must be $\Delta\phi < 0.2$ from the cluster in the ECAL barrel.
- Radial position of the hadronic energy deposition must be 100 $cm < r < 140$ cm.
- CaloTower must be tracker isolated, and contain no more than a sum of 2 GeV of transverse momentum with in a cone of $\Delta R < 0.4$.

Also, the same track and jet veto requirements as for the candidate selection have been applied to produce a pure sample of beam halo events. The timing template for beam halo is shown in Figure 4.15 (c).

ROOT TFractionFitter algorithm has been used to fit the prompt, anomalous signal, and beam halo templates to the candidates sample with no shower shape[9] and timing requirements. It has been found that the contribution of majority of background is from beam halo which can be seen in Figure 4.16. Within the 3 ns timing window, there were 1287 ± 65 halo events. After applying candidate shower shape requirement to the halo subset, $0.87 \pm 0.43\%$ of these survived. The halo contribution to the candidates was 11.1 ± 5.6 events.

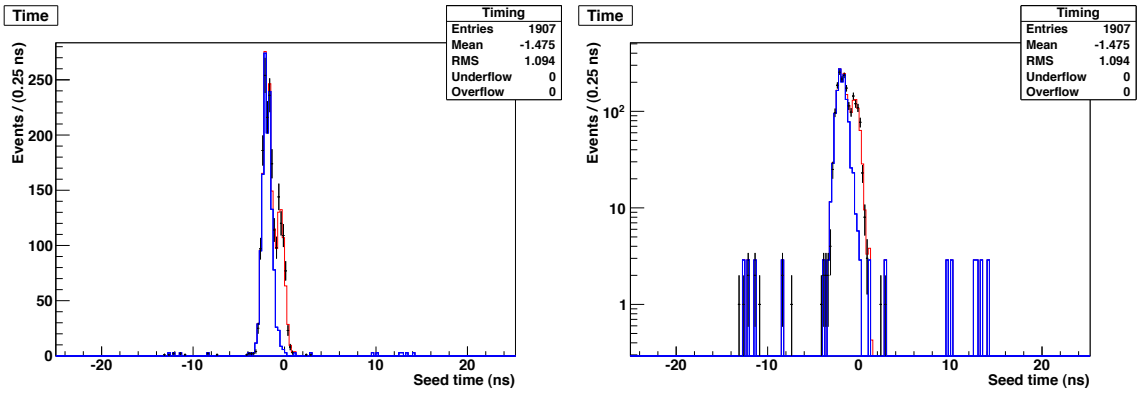

Figure 4.16: *Fit of template shapes to candidate timing distribution, shown in both linear and log scales. The contribution in blue is from beam halo and red corresponds to prompt candidates. A contribution due to anomalous signals would have been purple, but the fitter rejected this hypothesis.*

4.3.2 Jet fakes photon background

Analyses which involve the photons in the final state are always subject to "fakes" from QCD multijet and dijet events. These "fakes" occur if one of the high E_T jets fragments into isolated neutral π^0s or ηs which are sufficiently collimated to appear as a single electromagnetic shower in the ECAL.

The rate at which hadronic activity from QCD will pass the tight photon selection criteria is approximately $10^{-3} - 10^{-4}$. However, this rate seems to be small, the QCD production cross section is large enough compared to $Z(\nu\bar{\nu}) + \gamma$ production to make it an important background. The estimation of jets faking photon is done by initially constructing the fake

[9]shower shape requirement $\sigma_{i\eta i\eta} < 0.013$.

ratio from a control sample of data which is formed by requiring at least one HLT trigger used in the event selection listed in Table 4.2, the selected event contains a good vertex and it should pass the scraping event veto. Furthermore, it is required to match between the photon candidate and HLT object should be within $\Delta R < 0.2$, the photon object should be similar in energy to the objects that pass candidate selection requirements which ≈145 GeV but with $E_T^{miss} < 20$ GeV and no jet or track vetoes. The fake ratio (f) is defined as the number of events with an object passing the tight photon selection criteria compared to the number of events containing a jet which can give rise to a fake photon object. The numerator in this ratio is the number of events which satisfies the following selections:

- Ecal Iso $< 4.2 + 0.006 \times p_T^{\gamma}$
- Hcal Iso $< 2.2 + 0.0025 \times p_T^{\gamma}$
- Track Iso $< 2.0 + 0.001 \times p_T^{\gamma}$
- $H/E < 0.05$
- $\sigma_{i\eta i\eta} < 0.013$
- No pixel seed

The denominator constitutes the events with "fake" objects which pass at least one of the following selections:

- Ecal Iso $> 4.2 + 0.006 \times p_T^{\gamma}$
- Hcal Iso $> 2.2 + 0.0025 \times p_T^{\gamma}$
- Track Iso $> 3.5 + 0.001 \times p_T^{\gamma}$

as well as very loose photon selection requirements:

- Ecal Iso $<$ min $[5.0^*(4.2 + 0.006 \times p_{\mathrm{T}}), 0.2 \times p_T^{\gamma}]$

- Hcal Iso $<$ min $[5.0^{*}(2.2 + 0.0025 \times p_{\mathrm{T}}), 0.2 \times p_T^{\gamma}]$
- Track Iso $<$ min $[5.0^{*}(3.5 + 0.001 \times p_{\mathrm{T}}), 0.2 \times p_T^{\gamma}]$
- $H/E < 0.05$
- $\sigma_{i\eta i\eta} < 0.013$
- No pixel seed

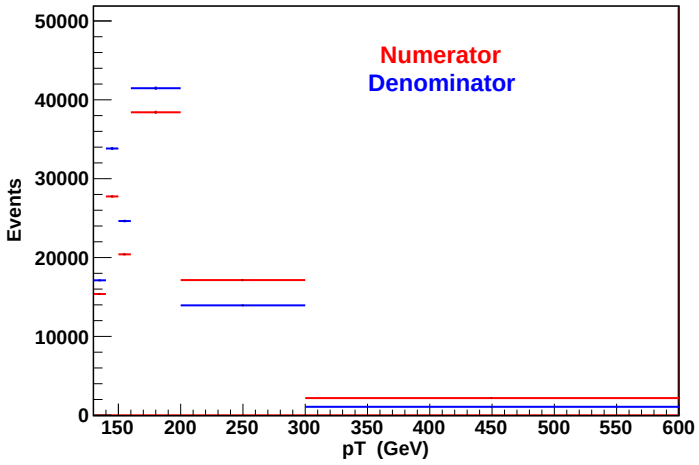

Figure 4.17: *Events selected in numerator (red) and denominator (blue) for the fake ratio.*

The events selected in the numerator and denominator as a function of p_T is shown in Figure 4.17. The numerator can have fraction of true isolated photons from inclusive QCD direct photon production. This contribution from true isolated photons has to be estimated and then subtracted to identify the true QCD fake rate. This fake ratio, f is represented by equation 4.2. Templates of $\sigma_{i\eta i\eta}$ from $\gamma + jet$ MC are used to calculate the fraction of real photons using the fraction fitting method in ROOT. The QCD templates are taken from data by choosing events within a side-band of track isolation which is expressed as: $(2.0 + 0.001 \times p_T) <$ track Iso $<$ $(4.0 + 0.001 \times p_T)$.

The results of the template fitting in various p_T bins for data are shown in Figure 4.18. The estimated fractions, which are evaluated using fraction fitting method, are calculated

within $\sigma_{i\eta i\eta} < 0.013$ to match the requirements on the numerator and the final candidate selection criteria.

$$f = \frac{\mathrm{N}_{\text{QCD events}} - \mathrm{N}_{\text{True photon}}}{\mathrm{N}_{\text{EM-like jet}}} \tag{4.2}$$

where $\mathrm{N}_{\text{QCD events}}$: QCD events passing tight photon selection criteria, $\mathrm{N}_{\text{True photon}}$: Estimated true photons from template fitting and $\mathrm{N}_{\text{EM-like jet}}$: QCD events passing very loose photon selection (jets)

The corrected fake ratio, whose numerator constitutes QCD events passing tight photon selection, is shown in Figure 4.19. This fake ratio, f, is parametrized as a function of p_T is represented by the following equation:

$$f_{p_T^\gamma} = 0.2551 - 2.406 \times 10^{-3} p_T^\gamma + 1.323 \times 10^{-5} {p_T^\gamma}^2. \tag{4.3}$$

The fake ratio in equation 4.3 is used to scale the QCD sample which is identical in character to the candidate event sample instead the tight photon identification condition has been replaced by the criteria from the denominator sample of f with requirement of $\sigma_{i\eta i\eta} < 0.013$ in order to minimize the beam halo contamination. The QCD multijet events faking single photon event is expressed as:

$$\mathrm{N}_{\text{Fake photon} + \not{E}_T^{miss}} = \mathrm{N}_{\text{EM-like jet}} \times f_{p_T^\gamma} \tag{4.4}$$

Referring to equation 4.4 the estimated total number of QCD multijet event is 11.15 ± 2.76. The error on the estimate is calculated by measuring the the uncertainty due to 1σ variation in several sources and adding them in quadrature. The sources of uncertainty include the fit parameters in the fake ratio, the systematics due to the different choices of sideband selection, the bins size of the shower shape templates and the statistical uncertainty from the normalization of the data sample. Among these, the statistical uncertainty from the

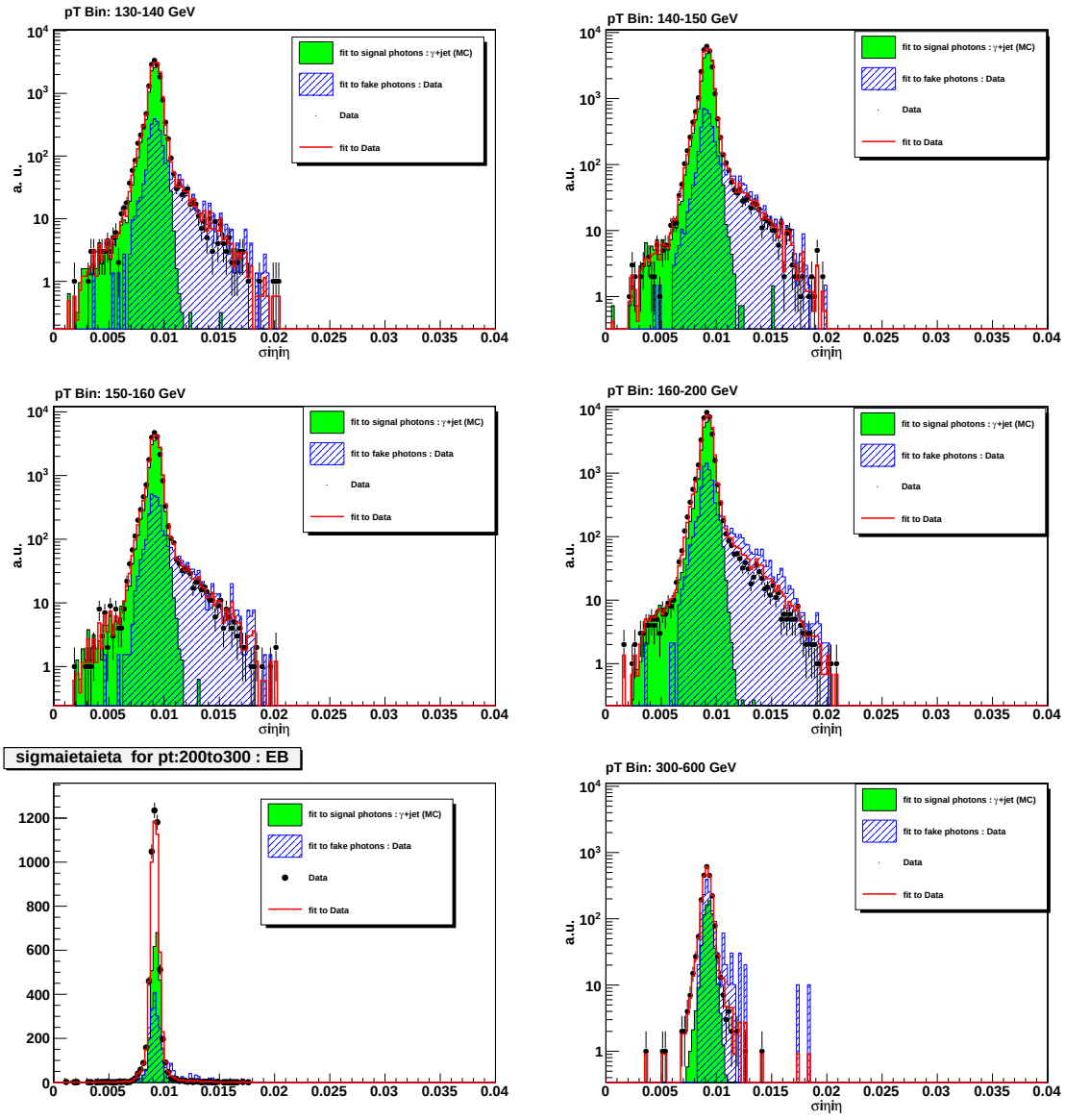

Figure 4.18: *Template ($\sigma_{i\eta i\eta}$) distributions and fits to QCD and true photon components for different p_T bins.*

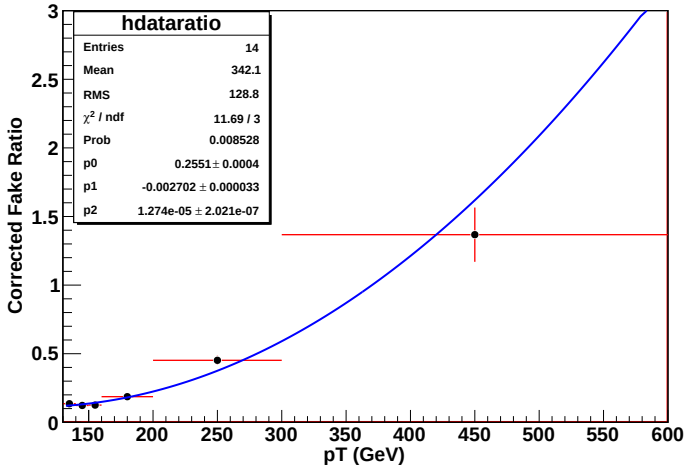

Figure 4.19: *The fake ratio as a function* $f_{p_T^\gamma} = p0 + p1 \times p_T + p2 \times p_T^2$

data sample normalization is the dominant source of uncertainty is this calculation. To evaluate the additional uncertainty on QCD multijet events, the selection of sideband and bin size of the templates is varied. These variations are summarized in Table 4.11 and Table 4.12 in detail for fitted QCD fractions. They include changing the sideband width, using the constant term of the track isolation in the sideband fit, requiring ECAL and HCAL isolation to fail for the QCD templates. Also, by changing the bins size by a factor of 0.5 and 2.0. The largest variation have been observed on inverting the ECAL and HCAL isolation criteria along with track isolation for the QCD templates and also when using MC for the shower shape background template instead of data within the same sideband region. The latter test has been performed on the first two bins and noticed the difference of 20% while by varying the sideband, the maximum difference of 18% in a given p_T bin. To account of these effects, a conservative systematic uncertainty of 20% has been assigned.

4.3.3 Electron Fakes Photon

Electrons can be misidentified and reconstructed as photons since both these objects deposit similar EM showers in the ECAL. Further, an electron is misreconstructed as a photon when there is no pixel seed reconstructed that is associated with the supercluster in the ECAL.

p_T^γ−Bins (GeV)	f_{qcd} $2.0 + 0.001p_T^\gamma >$ track Iso. $< 4.0 + 0.001p_T^\gamma$	f_{qcd} $2.0 >$trk Iso < 4.0	f_{qcd} $2.0 + 0.001p_T^\gamma >$ track Iso. $< 5.0 + 0.001p_T^\gamma$
130-140	0.151±0.013	0.168±0.014	0.120±0.009
140-150	0.150±0.010	0.169±0.012	0.117±0.007
150-160	0.151±0.013	0.169±0.014	0.117±0.008
160-200	0.202±0.014	0.218±0.014	0.126±0.007
200-300	0.367±0.027	0.406±0.028	0.221±0.024
300-600	0.673±0.094	0.645±0.0957	0.617±0.079

Table 4.11: *QCD fraction from template fits with different widths of the side-band of track isolation.*

p_T^γ−Bins (GeV)	f_{qcd} bin size increased by a factor of 2.0	f_{qcd} bin size reduced by a factor of 0.5	f_{qcd} ECAL and HCAL Iso also flipped for QCD template
130-140	0.144±0.012	0.157±0.013	0.079±0.012
140-150	0.141±0.009	0.154±0.011	0.067±0.006
150-160	0.144±0.012	0.157±0.013	0.062±0.007
160-200	0.162±0.011	0.207±0.014	0.084±0.014
200-300	0.324±0.028	0.397±0.028	0.289±0.028
300-600	0.684±0.097	0.745±0.105	0.489±0.125

Table 4.12: *QCD fraction from template fits for different bin sizes for the $\sigma_{i\eta i\eta}$ template distributions. The variation is also estimated when ECAL and HCAL isolations are also flipped for QCD templates.*

Most of the electrons misidentified as photons from $W \rightarrow e\nu$ resulting an event with an electron misidentified as a photon and E_T^{miss}. This background has been estimated from data. The pixel seed match efficiency, ϵ, has been studied extensively, initially estimated with MC simulated events and later measured as well as confirmed using $Z \rightarrow ee$ events in data [45] to be 0.9940 $\pm$ 0.0025. This value of ϵ has been estimated as function of p_T as shown in Figure 4.20. A control sample of electron candidate events $W(e\nu)$ in the data has been created with an event selection identical to the one used in this analysis but requiring a pixel seed and E_T^{miss} that are kinematically similar to the candidate events. Then, this number is divided by the pixel match efficiency to get total the number of electron events in the data. This total number of electron events is again weighted by the pixel match inefficiency $(1 - \epsilon)$ to get an estimate of the number of these electron events which could leak into the candidate sample.

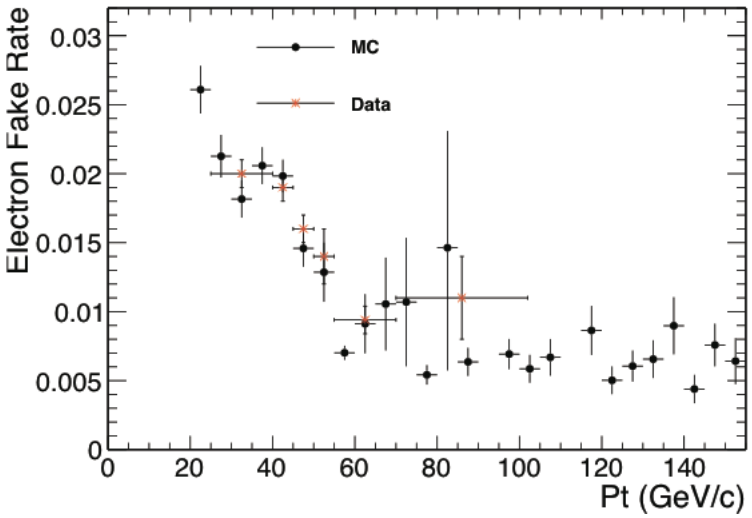

Figure 4.20: *Electron misidentification rate as a function of p_T comparing data and MC.*

$$N_e = N_{\text{pix-match}} \times \frac{(1-\epsilon)}{\epsilon} \tag{4.5}$$

The total number of $W(e\nu)$ candidate with pixel seed is 583 $\pm$ 24. After scaling this number using the equation 4.5, this gives an estimated 3.53 $\pm$ 1.48 events. The electron p_T

distribution, prior to being scaled by the pixel match inefficiency is shown in Figure 4.21. The estimation of this uncertainty has been mentioned in the appendix B.

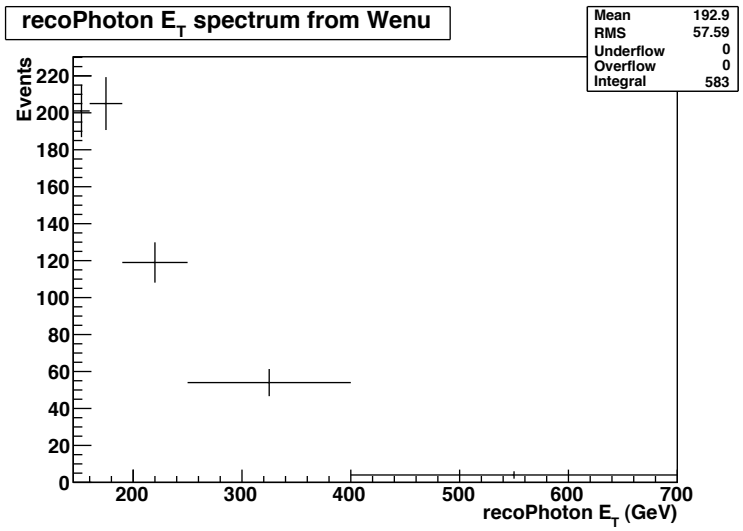

Figure 4.21: *Electron p_T distribution before weighting by pixel match inefficiency.*

4.3.4 Monte Carlo Based Estimation

Three the sources of background are estimated from MC simulated samples. Those backgrounds are from $W(l\nu)\gamma$, γ + jet, and diphoton events. With a cross section of 7.9 nb at the LHC from 7 TeV pp collisions, $W(l\nu)$ has the potential to be one of the largest background in this analysis. The $W \to e\nu$ has a real E_T^{miss} while $W\gamma$ event can have real photon from ISR, Final State Radiation (FSR) off the final state lepton and also a real photon emission from the W. Since $W \to e\nu$ where the electron can be misidentified as a photon (i.e. track reconstruction inefficiency) has been derived from data as mentioned in the subsection 4.3.3, MC based estimation has not been implemented in this analysis.

Most of the background estimated with MC is due to ISR. This ISR contribution has been estimated using a sample of $W(\to l\nu)\gamma$ events, which includes real photon from the W boson. There is small FSR contribution from W boson. This FSR contribution is estimated with a high mass $\hat{m}$ sample ($\hat{m} > 200$ GeV) of $W(\to l\nu)\gamma$ events from PYTHIA, it has been found to be very small and comes from very high-mass, off-shell W boson decay while

the radiated photon takes away most of the energy. To differentiate this FSR photon and the electrons faking photons and also to avoid the double counting from the later case, the electron in FSR event is required to have $p_T < 50$ GeV after they radiate the photon. An estimated $W(l\nu)\gamma$ event is 3.3 ± 1.1 events.

Diphoton events can be misidentified as a signal event if one of the photons escapes detection which leads to fake E_T^{miss} and a real photon. Based on a MC simulated sample, the contribution of diphoton event is 0.6 ± 0.3 in the signal sample.

At the LHC both photon production from QCD multijets, the γ + jet process can have large cross section and fake the signal event due to these following cases:

1. When the jet is misreconstructed, as a result of which there is fake E_T^{miss} with real photon.

2. When the real photon escapes the detector, giving rise to a fake E_T^{miss}, and jet fakes a photon.

The contribution from the latter case is estimated from data where a jet is misidentified as a photon while the contribution from the former one is estimated using MC sample which has been generated by PYTHIA generator. The double counting with the jet faking photon background from data is avoided by rejecting event if the photon candidate does not originate from the hard scattering. Hence the prediction from the simulated sample of the γ + jet is 0.5 ± 0.2 events which is the background to the signal.

The total estimated number of events originated from the electron, muon and τ final states of W decays as well as those from the diphoton and γ + jet channels which pass all cuts are listed in Table 4.13.

The total estimated events in Table 4.13 are events without pileup correction as well as no scale factor has been applied to correct MC events.

	Vertex	Scraping	Cosmic Veto	MET	γ-ID & p_T^{γ}&$\lvert\eta^{\gamma}\rvert$	Track Iso	Jet Veto	Track Veto	HLT	Events in 5.0 fb^{-1}
W+γ	0.999	0.999	0.591	0.002	8.19e-05	7.62e-05	1.41e-05	1.22e-05	1.22e-05	$4.27^{+1.74}_{-1.16}$
W$\rightarrow e\nu$	0.998	0.998	0.992	0.236	0.0085	0.0069	0.0048	0.0032	0.0032	$0.36^{+0.13}_{-0.10}$
W$\rightarrow \mu\nu$	0.997	0.997	0.116	0.014	0.000	0.000	0.000	0.000	0.000	$0.00^{+0.05}_{-0.0}$
W$\rightarrow \tau\nu$	0.999	0.999	0.780	0.124	0.018	0.015	0.0092	0.0083	0.0083	$0.26^{+0.12}_{-0.08}$
$\gamma\gamma$	0.999	0.999	0.923	0.010	0.0069	0.0066	0.0017	0.0012	0.0012	$0.54^{+0.60}_{-0.27}$
γ+Jet	0.998	0.998	0.750	0.012	0.0060	0.0058	6.20e-07	3.38e-07	3.38e-07	$0.63^{+0.58}_{-0.29}$

Table 4.13: *Cumulative efficiencies of the background processes after successive analysis cuts. The last column shows the total number of events from each background at 5.0 fb^{-1}.*

Chapter 5

Analysis

5.1 Cross section measurement

The measurement of the cross section for $Z(\nu\bar{\nu})\gamma$ events is calculated as:

$$\sigma \times \mathrm{BR} = \frac{N_{\mathrm{data}} - N_{\mathrm{bkg}}}{A \times \epsilon \times \mathcal{L}} \tag{5.1}$$

where N_{data} is the number of events found in data, N_{bkg} is the predicted number of background events, A is the geometric and kinematic acceptance of the selection criteria, ϵ is the selection efficiency for the signal and $\mathcal{L}$ is the integrated luminosity. The term $A \times \epsilon$ can be further written as : $A \times \epsilon_{MC}$ from simulated events and then multiplying it by a scale factor, ρ as mentioned in Table 4.10, to correct for the difference in efficiency between the simulated and real events. The systematic uncertainty that contribute to $A \times \epsilon_{MC}$ are from the choice of PDF [46–48], the selection of the primary vertex for the photon, how the pileup has been modeled and the energy calibration and resolution for photon [49], jets [23], and E_T^{miss} [22]. These are described in the subsequent sections in details.

5.2 Vertex uncertainty

In the higher pileup scenario of the current dataset, the assigned vertex may not have been the origin of the photon which has been described in subsection 4.1.4. Hence, there is possibility that the photon candidate may be assigned the wrong vertex, which can affect

the calculation of E_T^γ and corresponding E_T^{miss} in an event. For this study, a control sample of $W \to e\nu$ event in data is used. Then identify the track associated to the electron and exclude it. The next step is to form the sum of the squares of the track p_T for each of the vertices identified in the event (this is the procedure implemented for the identification of the primary vertex as Ref [50]) and find the primary vertex without the electron track. It has been found that 38% of events which has the newly chosen vertex is not the one associated with the electron.

In this 38% of the events, after recalculating transverse energy E_T^γ and find the percentage difference between the true E_T^γ with the vertex reassigned as shown in Figure 5.1 [6]. From this study an additional 2% uncertainty has been assigned to the photon transverse energy resolution, which is included in the overall calculation of the acceptance.

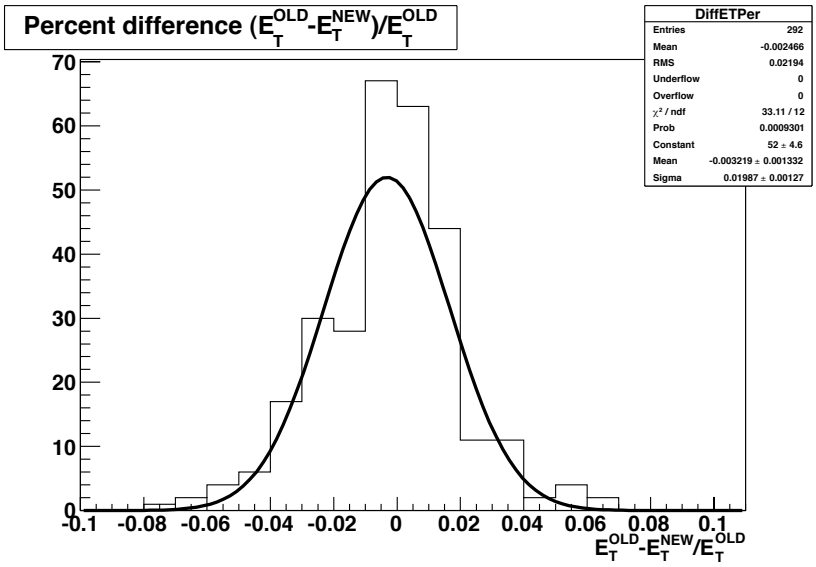

Figure 5.1: *Event selection showing data points along with the contributions from various processes in photon p_T for the full data set 5 fb^{-1}.*

5.3 Pileup modeling

In high luminosity colliders, one single bunch crossing may produce several separate inelastic interactions. Hence, the additional proton proton interactions which result in multiple pos-

sible events per collisions are known as pileup or pileup interactions. The number of pileup interactions depends on the instantaneous luminosity of the collider. Also, the presence of pileup results the excess information in the event causing affect on the reconstruction efficiency. In the MC simulation, the hard scattered interactions are overlaid with a number of minimum bias interactions (events collected by a scaled inclusive trigger, largely comprising of low p_T , soft events); this simulates the presence of pileup. However, this is not sufficient to construct a complete model of the effects of pileup. Further, signal integration time in some of the CMS sub-detector system is long enough to include those out-of-time pileup interactions. In order to take this into account, 3D pile up re-weighting procedure has been implemented. This process takes into account of the presence of pileup interactions in bunch-crossing spaced within $\pm$ 50 ns of each interaction of interest. The official re-weighting method for 2011 for MC has been used [51]. By using the Deterministic Annealing primary vertex reconstruction algorithm to reconstruct primary vertices, there is a good overall agreement between data and MC simulation as shown in Figure 5.2. The systematic error of $\pm$ 2.4% that contributes to the acceptance uncertainty is due to pileup modeling.

5.4 PDF uncertainty

The event generated by MC generated uses parton distribution function (PDF) which can introduce theoretical uncertainty in the cross section estimation. The MC samples are produced with PYTHIA using the LO with PDF as CTEQ6L1 [46] and then $Z(\nu\bar{\nu})\gamma$ LO cross section is then scaled to reflect NLO effects by a k-factor obtained from BAUR MC, which uses the CTEQ61 CTEQ66 as PDF for LO and NLO respectively. This calculation procedure for k-factor has been described in subsection 4.1.1. The uncertainty due to the choice of PDF is calculated according to the PDF4LHC guidelines [47], and the technique established by the CMS EWK group [52], where the simulations are rerun with different PDFs produced by varying the defining eigenvectors, and the results are compared. The

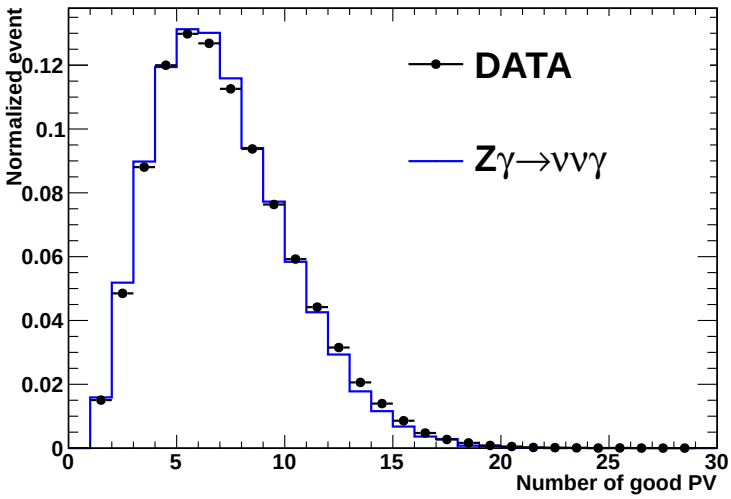

Figure 5.2: *Distribution for number of good primary vertices (PV) for the 3D pile up reweighted $Z(\nu\bar{\nu})\gamma$ MC sample and full data set 5 fb^{-1}.*

observed error on the acceptance due to the choice of PDF is ± 2.4% for $Z(\nu\bar{\nu})\gamma$.

5.5 Energy scale of physics objects

The sources of the systematics uncertainty, the contributions to the uncertainty on the acceptance calculation are the photon, jet and E_T^{miss} scale and resolution, PDF and pileup modeling. These sources of uncertainty are as follows: The uncertainty on the photon scale is estimated to be 1.5% based on the FSR measurement with Z [41]. The E_T^{miss} scale uncertainty is taken as a conservative 5%, based on the estimate derived from the 2010 data [22]. The uncertainty on the E_T^{miss} resolution is taken as the difference between the MC prediction and the measured resolution in the data, which corresponds to approximately 10%. Uncertainties on the E_T^{miss} scale and resolution are conservative, but even so have only minor contributions to the overall systematic uncertainty on the acceptance. Jet energy scale uncertainties version 2011V2 are used [23]. The jet energy resolution is scaled up by 10% based on the stretching method [53].

PDF uncertainties are accounted as described in the previous section 5.4. The uncer-

tainties due to the pile-up modeling are evaluated using MC and assuming 8% uncertainty of the average number of pile-up interaction. A summary of the systematic uncertainties in $A \times \epsilon_{MC}$ for $Z(\nu\bar{\nu})\gamma$ is presented in the Table 5.1.

Source	Sys error in $A \times \epsilon_{MC}$ [%]
Photon scale	+4.2 -4.3
E_T^{miss} scale	+1.6 -3.1
E_T^{miss} resolution	± 0.03
jet energy scale	+0.85 -0.79
jet resolution	±0.2
Photon vertex	± 0.3
Pile-up	± 2.4
PDFs	± 2.4
Total	+5.7 -6.3

Table 5.1: *Systematic uncertainties on $A \times \epsilon_{MC}$ calculated for $Z(\nu\bar{\nu})\gamma$.*

5.6 Scale factor

For the MC based SM backgrounds and signal, $A \times \epsilon_{MC}$ term is multiplied by a scale factor (ρ) in order to take into account for the difference in the efficiency between data and MC simulation. The calculated ρ as mentioned in Table 4.10 is 0.90 ± 0.11. This takes into account the studies of the trigger, photon reconstruction, cluster timing, and vetoes which have been applied in this analysis.

5.7 Acceptance calculation for $Z(\nu\bar{\nu})\gamma$

The product of $A \times \epsilon_{MC}$ in the cross section calculation is determined from the MC simulation PYTHIA LO sample with p_T cutoff at 145 GeV/c with in the rapidity range $| \eta | < 1.44$. The events are re-weighted to match the pileup profile predicted for the data using 3D pileup re-weighting as mentioned in the section 5.3. The $A \times \epsilon_{MC}$ is 0.452 ± 0.003, where the uncertainty is statistical. The $A \times \epsilon$ is estimated to be 0.407 ± 0.055 based on the LO simulation and includes the difference in efficiency between data and MC simulation for

the trigger, photon reconstruction, consistency of cluster timing, jet and track vetoes [5], also systematic uncertainty in $A \times \epsilon_{MC}$. The photon, jet and E_T^{miss} scale and resolution and PDF as well as pileup modeling are the sources of systematic uncertainties in $A \times \epsilon_{MC}$ calculation as mentioned in Table 5.1. Additional uncertainty of 2% has been included for the acceptance due to the requirement in the generated $p_T > 145$ GeV in the rapidity range of 1.44. The systematic uncertainty on the measured integrated luminosity is 2.2% [54].

5.8 Standard Model Results

Applying the selection criteria as mentioned in Chapter 4 for this analysis for the data collected with pp collisions at center of mass energy of $\sqrt{s} = 7$ TeV, 73 events are observed in 5 fb^{-1} data. The list of backgrounds, expected signals are summarized in the Table 5.2. The p_T and E_T^{miss} spectrum of the full combination of the candidate events and selected backgrounds can be seen in Figure 5.3. The corresponding ratio of photon p_T over E_T^{miss} is represented by Figure 5.4 (a). This ratio plot shows most of the candidate events are photon p_T balancing E_T^{miss}. The selected candidate events, whose photon p_T and E_T^{miss} are separated by an angle 2π radian, are shown in Figure 5.4 (b). An event display of the highest photon p_T event in 5 fb^{-1} data is shown in Figure 5.5.

Source	Estimate
Jet Fakes Photon (data)	11.2 ± 2.8
Beam Halo (data)	11.1 ± 5.6
Electron Fakes Photon (data)	3.5 ± 1.5
Wγ (MC)	3.3 ± 1.1
Diphoton (MC)	0.6 ± 0.3
γ+jet (MC)	0.5 ± 0.2
Total Background	30.2 ± 6.5
data	73
$Z(\nu\bar{\nu})\gamma$ (NLO)	45.3 ± 6.9

Table 5.2: *Summary of estimated backgrounds for full data 5.0 fb^{-1}.*

Using the equation 5.1, taking into account of systematic uncertainty on the integrated luminosity as 2.2% [54]. The resulting cross section for $Z(\nu\bar{\nu})\gamma$ for photon $p_T > 145$ GeV

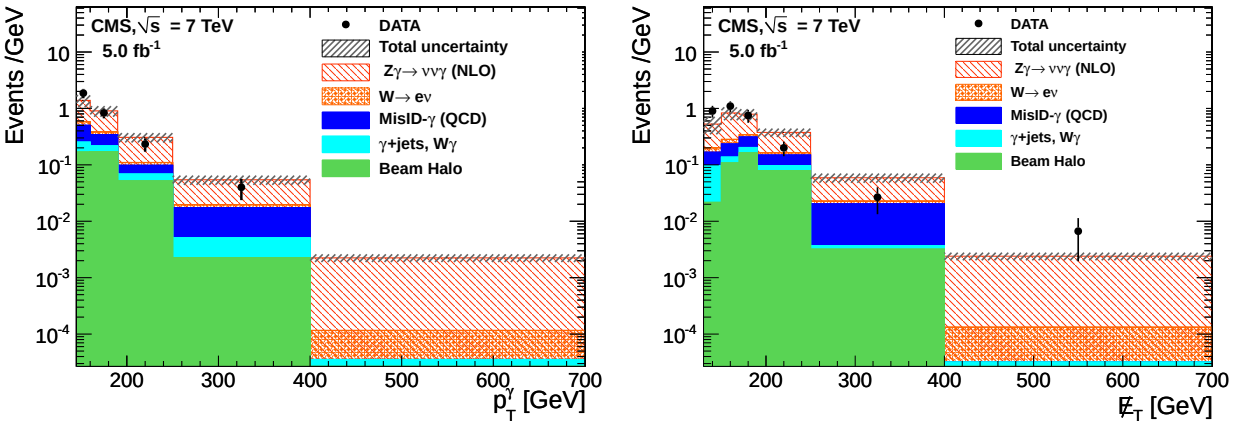

Figure 5.3: *Final event selection showing data points along with the contributions from various processes in terms of photon p_T (a) and E_T^{miss} (b). The shaded bands denote the background uncertainty.*

with in the rapidity of 1.44 is 21.3 ± 4.2 (stat.) ± 4.3 (sys.) ± 0.5 (lumi.) fb, which is in good agreement with the theoretical prediction[1] at NLO of 21.9 ± 1.1 fb with respect to BAUR MC. The uncertainty in the theoretical prediction at NLO takes into account of PDF and scale error. The uncertainties on measured cross section is using the formula given in B.4.

5.9 Statistical significance of the $Z\gamma \to \nu\bar{\nu}\gamma$ measurement

The evidence of $Z\gamma \to \nu\bar{\nu}\gamma$ production is estimated by running 10^8 pseudo experiments on the a background only hypothesis. This estimation is done in two steps:

- Throw a pseudo experiment. Using Gaussian statistics, obtain new background for each background which is considered in this analysis. Then for each value of new background, obtain an observed number of events using Poisson statistics. For each throw, count total observed number of events. The distribution observed events is

[1] σ_{145} has been calculated based on generated events at p_T >145 in barrel region, number of generated events in signal sample $PYTHIA$, and its cross section. k-factor from $BAUR$ MC has been applied to get the theoretical prediction at NLO.

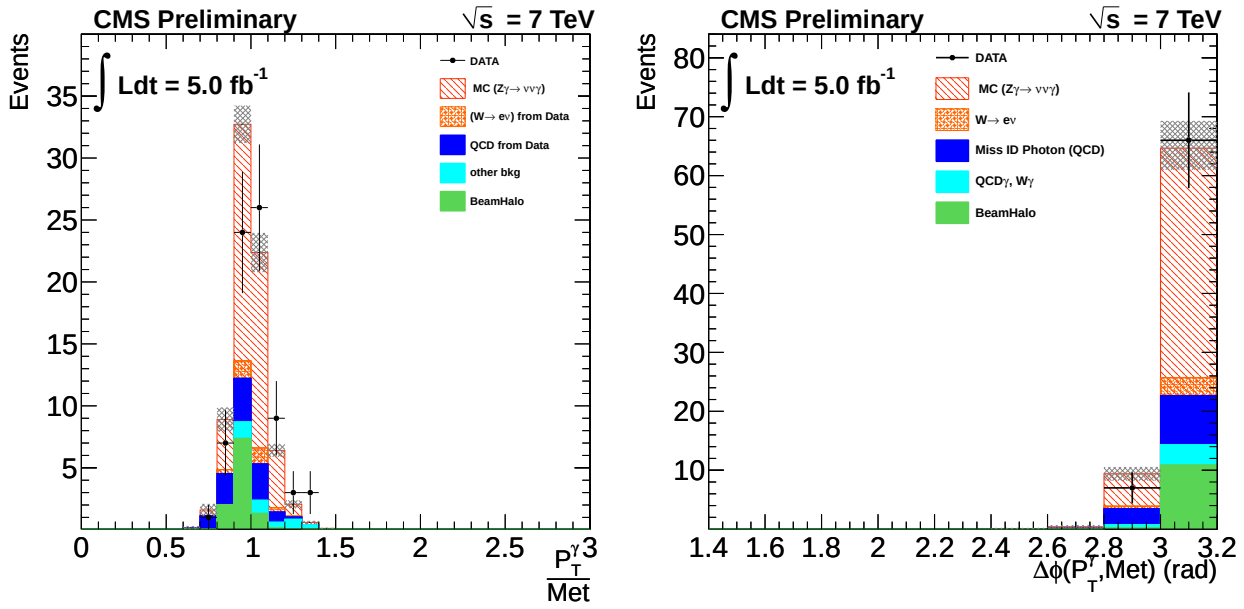

Figure 5.4: *Final event selection showing data points along with the contributions from various processes in terms of photon p_T/E_T^{miss} (a) and angle between p_T and E_T^{miss} (b). The shaded bands denote the background uncertainty.*

given in Figure 5.6.

- Find the probability of observed number of events (background) to fluctuate into the number of events that has been observed in data (73).

It has been found that the probability of the background to fluctuate to observed number of events in data is 9.11×10^{-6}. This corresponds to an observed significance of 4.2σ. Hence from this analysis, there is an evidence of $Z\gamma \to \nu\bar{\nu}\gamma$ production with significance of about 4.2σ.

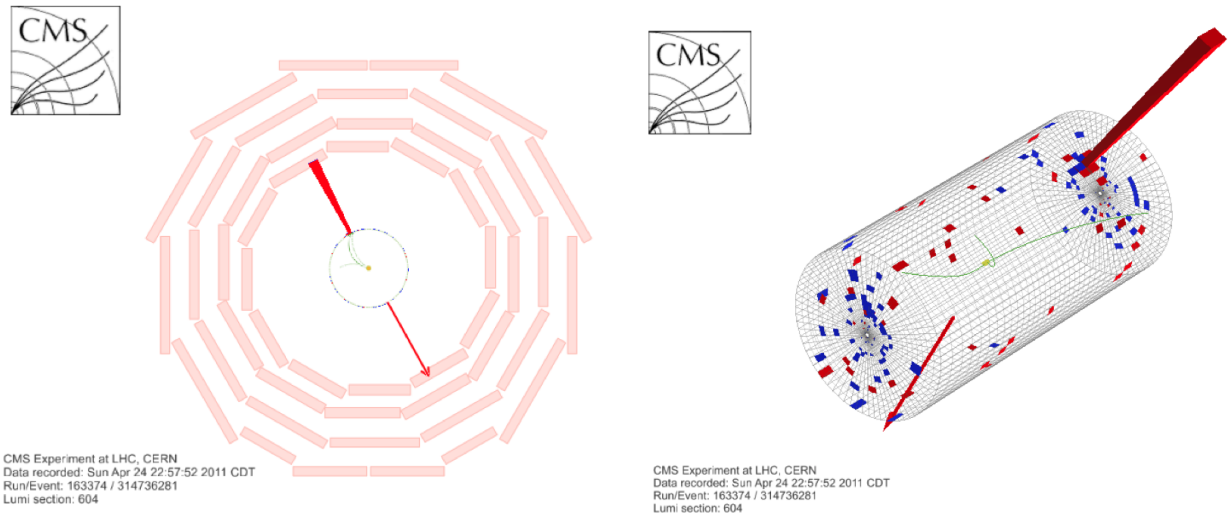

Figure 5.5: *X-Y view of of highest p_T signal photon and E_T^{miss} event in data (a) and Cylindrical view of the same event (b).*

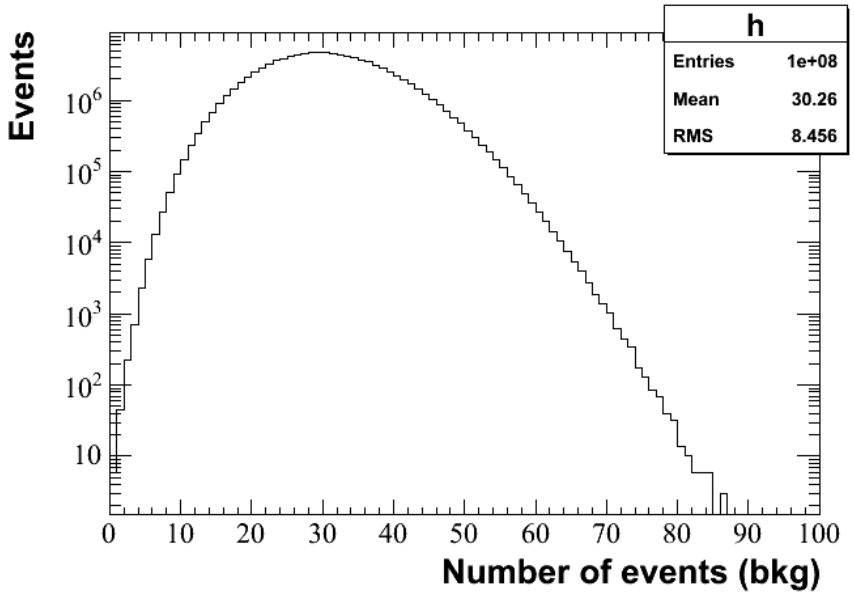

Figure 5.6: *Distribution of Background fluctuation from pseudo experiment by running 10^8 times.*

Chapter 6

Anomalous Triple Gauge Coupling Limits

6.1 Anomalous Triple Gauge Coupling $Z\gamma$

Anomalous Triple Gauge Couplings are the result of non-Abelian[1] nature of the SM electroweak sector $SU(2)_L \times U(1)_Y$ which has been discussed in subsection 3.1.1. The efforts have been made to search for evidence of non-zero $ZZ\gamma$ and $Z\gamma\gamma$ couplings in $Z(\rightarrow l^+l^-)\gamma$ ($l = e, \mu$) and $Z(\rightarrow \nu\bar{\nu})\gamma$ production. These couplings vanish in the SM at the tree level. However, if new interactions beyond the SM are responsible for nonzero $ZZ\gamma$ and $Z\gamma\gamma$ couplings, then $Z\gamma$ production might indicate a clean signal for new physics. Hence, an experimental measurement of TGCs can be a sensitive place to probe new phenomena at high energies which require more energy or luminosity to be observed directly. In this analysis, the $ZZ\gamma$ and $Z\gamma\gamma$ couplings are measured without form-factor scaling since this provides a result without any particular bias which may arise due to choice of the form factor energy dependence as mention in subsection 3.2.1. This translates $n = 0$ in equation 3.9 for both h_3^V and h_4^V where V = Z or γ.

[1] Non-commutative, AB $\neq$ BA

6.2 $ZZ\gamma$ and $Z\gamma\gamma$ couplings

The most general vertex function for $ZZ\gamma$, which has been mentioned in section 3.2, is expressed briefly as:

$$\begin{aligned}\Gamma^{\alpha\beta\mu}_{\mathrm{Z}\gamma\mathrm{Z}}(q_1,q_2,P) &= \frac{P^2-q_1^2}{m_{\mathrm{Z}}^2}\Bigg[\; h_1^{\mathrm{Z}}(q_2^\mu g^{\alpha\beta}-q_2^\alpha g^{\mu\beta}) \\ &\quad + \frac{h_2^{\mathrm{Z}}}{m_{\mathrm{Z}}^2}P^\alpha\Big[(P\cdot q_2)g^{\mu\beta}-q_2^\mu P^\beta\Big] \\ &\quad + h_3^{\mathrm{Z}}\epsilon^{\mu\alpha\beta\rho}q_{2\rho} \\ &\quad + \frac{h_4^{\mathrm{Z}}}{m_{\mathrm{Z}}^2}P^\alpha\epsilon^{\mu\beta\rho\sigma}P_\rho q_{2\sigma}\Bigg]\end{aligned}$$

with $Z\gamma\gamma$ vertex obtained by the following replacements:

$$\frac{P^2-q_1^2}{m_Z^2}\to\frac{P^2}{m_Z^2}\text{ and }h_i^Z\to h_i^\gamma,\ i=1,...,4. \tag{6.1}$$

The couplings h_i^V with $V=Z,\gamma$ and $i=1,2$ violate CP symmetry, while those with $i=3,4$ are CP-even. The CP-conserving couplings h_3^V, h_4^V lead to amplitudes which interfere the SM ones resulting in the total cross section of the $Z\gamma$ process is enhanced while CP-violating couplings h_1^V, h_2^V do not interfere with the SM ones [55]. In this analysis, the results have been interpreted in terms of h_i^V with $i=3,4$.

6.3 Statistical Tool

To calculate the compatibility of the expected number of "anomalous" events with the measured number of events in the CMS experiment, and to set the sensitivity limits on the presence of anomalous couplings, Poisson probability distribution has been assumed. anomalous TGC results have been interpreted by setting bounds on the ratio of the observed signal to that of the expected anomalous TGC yield using the likelihood formalism which has been described below. For a specific values of photon transverse momentum p_T, the probability of observing the actual number of events $\mathbf{X}$ for the specific value of p_T for a

given expectation value d in the data is represented by the Poisson distribution as :

$$p(\mathbf{X}; d) = \frac{d^{\mathbf{X}} e^{-d}}{\mathbf{X}!} \quad , \quad d = \mu \cdot \mathbf{s}(\vec{\alpha}, \vec{\theta_s}) + \mathbf{b}(\vec{\theta_b}), \tag{6.2}$$

Where d consists of signal and background predictions which are modeled separately, the signal $\mathbf{s}(\vec{\alpha}, \vec{\theta_s})$ and background $\mathbf{b}(\vec{\theta_b})$ expectations are described in terms of the TGC values $\vec{\alpha}$ and nuisance parameters $\vec{\theta_s}$ and $\vec{\theta_b}$. The parameter μ is the signal strength modifier which is usually be taken as 1. The nuisance parameters are divided into three components: Increase and decrease of the expectation values given a fractional change in the following parameters:

- integrated luminosity $f_{\mathcal{L}}$.
- signal selection systematic uncertainties $f_{Sig.}^{\text{Syst.}}$.
- background selection systematic uncertainties $f_{Bkg.}^{\text{Syst.}}$.

Hence the signal expectation $\mathbf{s}(\vec{\alpha}, \vec{\theta_s})$ and background expectation $\mathbf{b}(\vec{\theta_b})$ can be expressed as:

$$\mathbf{s}(\vec{\alpha}, \vec{\theta_s}) = f_{\mathcal{L}} \cdot f_{Sig.}^{\text{Syst.}} \cdot N^{\text{Sig.}}(\vec{\alpha}) \qquad \mathbf{b}(\vec{\theta_b}) = f_{bkg}^{\text{Syst.}} \cdot N^{\text{bkg}}. \tag{6.3}$$

Here, N_{sig} and N_{bkg} are the predicted signal and background event yields.

The likelihood is constructed from the product of $p(N; d)$ over all photon p_T bins with the data event yield N_i and d_i as defined in equation. 6.2.

$$\mathrm{L}(\mu, \vec{\alpha}, \vec{\theta}) = \prod_i Poisson(N_i, d_i(\mu, \vec{\alpha}, \vec{\theta})) \quad , \text{ where } \quad \vec{\theta} = (\vec{\theta_s}, \vec{\theta_b}) \tag{6.4}$$

The errors on the quoted luminosity, signal selection, and background fraction are considered to be log-normally distributed and reflect this in the nuisance parameters by requiring log-normal constraints.

The upper limits on TGCs is determined by using the following test statistics:

$$t_{\mu,\vec{\alpha}} = -2 \ln \lambda(\mu, \vec{\alpha}) \quad , \text{ where } \qquad \lambda(\mu, \vec{\alpha}) = \frac{\mathrm{L}(\mu, \vec{\alpha}, \hat{\hat{\vec{\theta}}})}{\mathrm{L}(\hat{\mu}, \vec{\alpha}, \hat{\vec{\theta}})} \tag{6.5}$$

with $\hat{\hat{\vec{\theta}}}$ being the conditional maximum-likelihood estimator of $\vec{\theta}$ and $\hat{\mu}$ and $\vec{\theta}$ being their maximum-likelihood estimators. The hypothesized values of TGCs is being excluded based on whether the ratio of p-values:

$$CL_s = \frac{p_{s+b}}{1 - p_b} \tag{6.6}$$

is less than a given threshold (α) which has been considered 0.05 for 95% Confidence Level (CL). The detail information can be found in likelihood-based tests [56]. This formalism is implemented using the RooStats package [57]. In equation 6.3, background yield and signal, which is the difference between anomalous TGC yield and SM yield, are calculated for each photon p_T used for each grid point. The anomalous TGC yield is obtained based on following principle. Since the vertex amplitude is linear in the anomalous couplings as mentioned in equation 6.7, the most general form for the cross section as well as the function giving the number of events has quadratic dependence on the couplings. In the specific case of the non-zero CP-conserving couplings, the number of predicted events in an elliptical paraboloid function of h_3 and h_4 for given photon p_T is given as:

$$n_{ac}(h_3, h_4) = N^{SM} + A.h_3 + B.h_4 + C.h_3.h_3 + D.h_4.h_4 + E.h_3.h_4 \tag{6.7}$$

N^{SM}: number of SM events and A,..,E are coefficients. The paraboloid function is obtained for each photon p_T bin, by fitting a two dimensional surface over the grid of event yield of the nine samples against h_3 and h_4. With the use of the resulting functions, it is possible to extrapolate the prediction of event yield for any value of the h_3 and h_4 couplings within the fitting range.

The predicted rate for events with high p_T photon as well as E_T^{miss} are in good agreement with the observed rate in data as shown in Figure 5.3. Thus, we proceed with limits setting on the CP-conserving parameters. The photon p_T spectrum with anomalous TGC signal is shown in Figure 6.1, 6.2, 6.3. We present the limits as two dimensional contours in h_3 and h_4 space for $ZZ\gamma$ and $Z\gamma\gamma$ couplings. We also quote one dimensional limit on one of the anomalous TGC parameter in the pair, when the other parameter is fixed to zero.

95% CLs limits on the CP-conserving parameters of $ZZ\gamma$ and $Z\gamma\gamma$ couplings are shown in Figure 6.4 and Figure 6.5 and corresponding one-dimensional 95% CLs limits are mentioned in Table 6.1. Because of the large $Z \to \nu\bar{\nu}$ branching ratio i.e., $Z(\to \nu\bar{\nu})\gamma$ cross section is about a factor of 3 times larger than the combined $Z(\to e^+e^-)\gamma$ and $Z(\to \mu^+\mu^-)\gamma$ rate [30], the limits in CP-conserving parameters of neutral anomalous TGC have better sensitivity from $Z(\to \nu\bar{\nu})\gamma$ channel compared to that from $Z(\to ll)\gamma$ channels [41].

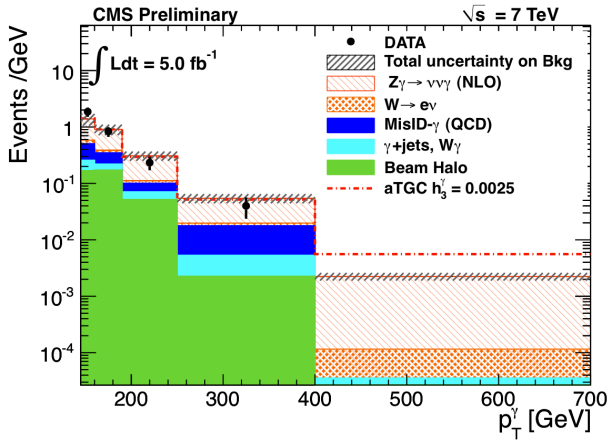

Figure 6.1: *The photon p_T distribution in data (dots) compared with estimated contribution from SM backgrounds (filled histograms) with a typical anomalous TGC signal is shown as dot-and-line histogram. The last bin also includes overflows.*

Coupling	Upper limit on $\|h_3\|$, 10^{-3}	Upper limit on $\|h_4\|$, 10^{-5}
$Z\gamma\gamma$	3.2	1.6
$ZZ\gamma$	3.1	1.4

Table 6.1: *One-dimensional limits on $Z\gamma$ anomalous triple gauge couplings from Z boson decays to a pair of neutrinos in CMS.*

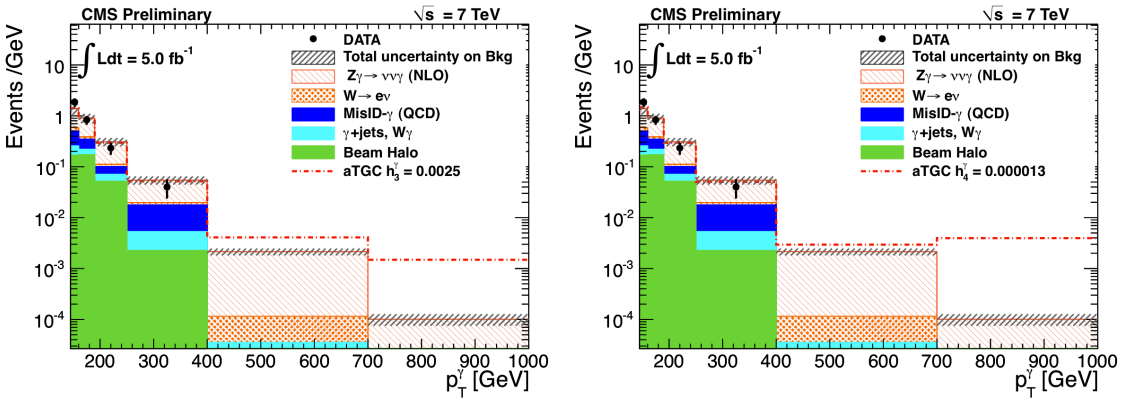

Figure 6.2: *The photon p_T distribution in data (dots) compared with estimated contribution from SM backgrounds (filled histograms) with a typical anomalous TGC signal with $Z\gamma\gamma$ vertex for the extended range to 1000 GeV is shown as dot-and-line histogram. The last bin also includes overflows.*

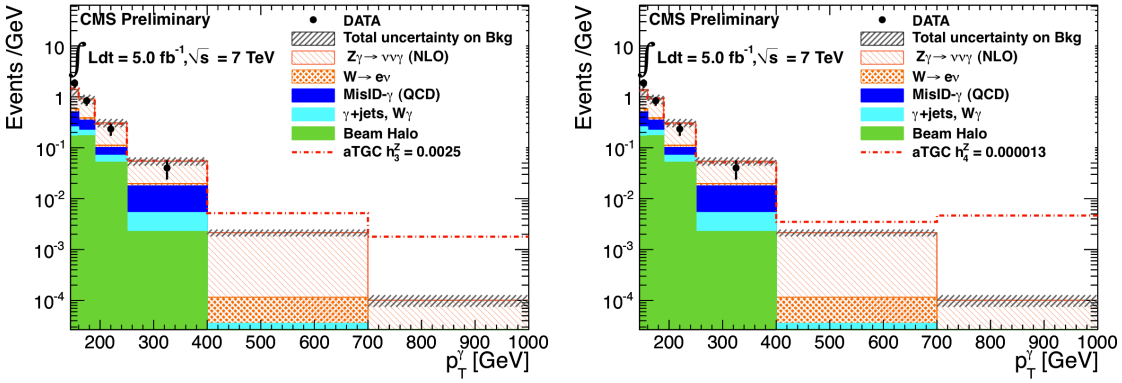

Figure 6.3: *The photon p_T distribution in data (dots) compared with estimated contribution from SM backgrounds (filled histograms) with a typical anomalous TGC signal with $ZZ\gamma$ vertex for the extended range to 1000 GeV is shown as dot-and-line histogram. The last bin also includes overflows.*

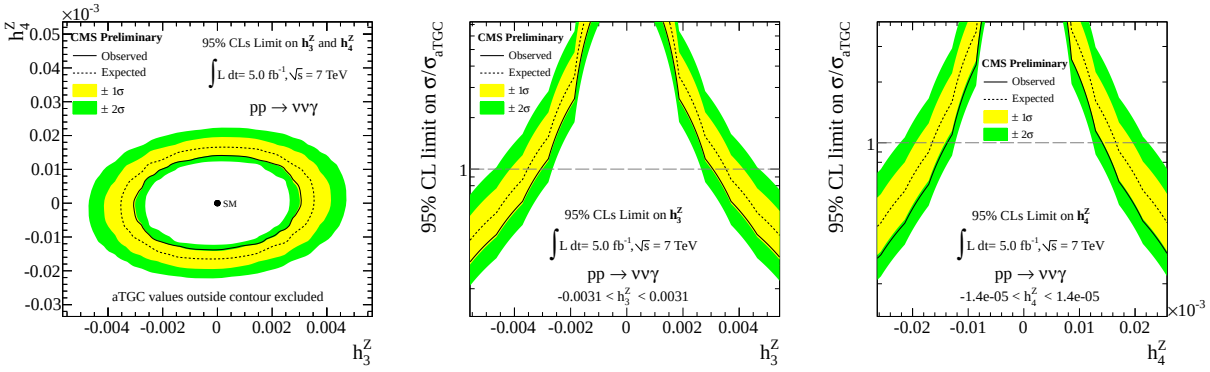

Figure 6.4: *Two-dimensional and One-dimensional 95% CLs limit for $ZZ\gamma$ couplings.*

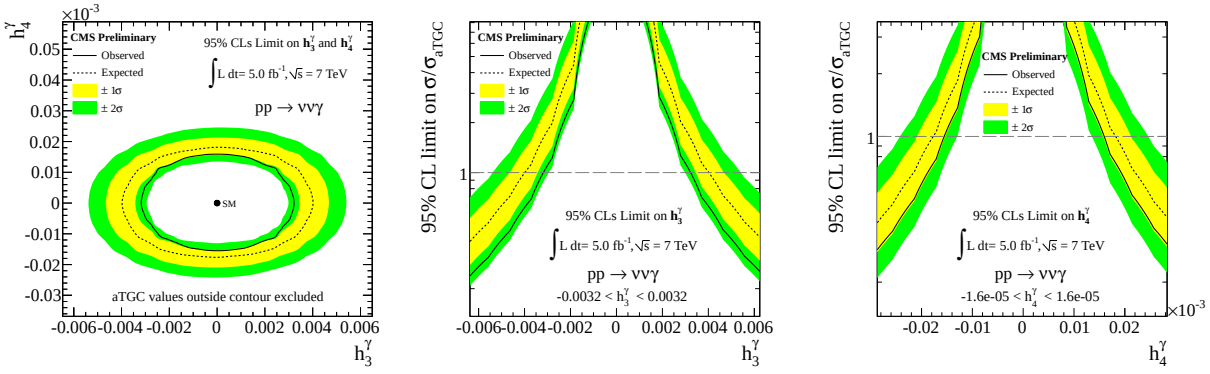

Figure 6.5: *Two-dimensional and One-dimensional 95% CLs limit for $Z\gamma\gamma$ couplings.*

Chapter 7

Conclusion

In conclusion, the complete methodology for performing the measurement of $Z\gamma \to \nu\bar{\nu}\gamma$ production cross section and limits on anomalous triple gauge couplings in pp collisions at $\sqrt{s} = 7$ TeV in 5 fb^{-1} of CMS data has been presented. With respect to the regime of photon $p_T > 145$ GeV in the rapidity $|\eta| < 1.44$, the measured cross section is 21.3 $\pm$ 4.2 (stat.) $\pm$ 4.3 (syst.) $\pm$ 0.5 (lumi.) fb which is in good agreement with the theoretical prediction of 21.9 $\pm$ 1.1 fb at next to leading order precision from BAUR. Although there was no indication of phenomena beyond the SM, CMS was able to offer a very precise analysis which means the obtained experimental limits on the values of the couplings are even more stringent than the ones previously achieved. Indeed, limits on h_3^V and h_4^V where V is either Z or γ are the the most stringent limits on the anomalous triple gauge couplings as of today.

Bibliography

[1] M. Glashow. Partial symmetries of weak interactions. *Nucl. Phys.*, 22:579–588, 1961.

[2] S. Weiberg. A model of leptons. *Phys. Rev. Lett.*, 19:1264–1266, 1967.

[3] A. Salam and N. Svartholm (ed.). Elementary particle theory, relativistic groups, and analyticity. *Stockholm, Sweden*, 8th Nobel Symposium:367–377, 1968.

[4] The CMS Collaboration. Measurement of the production crosss section for $Z\gamma \to \nu\bar{\nu}\gamma$ in pp collisions at $\sqrt{s} = 7$ TeV and limits on $ZZ\gamma$ and $Z\gamma\gamma$ triple gauge couplings. *SMP-12-020*, 2012.

[5] CMS Collaboration. Search for Dark Matter and Large Extra Dimensions in pp Collisions Yielding a Photon and Missing Transverse Energy. *Phys. Rev. Lett.*, 108:261803, 2012.

[6] The CMS Collaboration. $Z\gamma$ at $\sqrt{s} = 7$ TeV where Z Decays Invisibly. *CMS-AN-11-108*, 2011.

[7] The CMS Collaboration. Limits on the Anomalous $ZZ\gamma$ and $Z\gamma\gamma$ couplings at $\sqrt{s} =$ 7 TeV where Z decays invisibly. *CMS-AN-12-093*, 2012.

[8] O. E. Bruning et al. LHC design report. Vol. I: The LHC main ring. CERN-2004-003-V-1, 2004.

[9] L. Evans and P. Bryant (editors). LHC Machine. *JINST*, 3, 2008.

[10] ATLAS Collaboration. Detector and physics performance technical design report. *CERN-LHCC-99-14*, 1, 1991.

[11] CMS Collaboration. The CMS experiment at the CERN LHC. *JINST*, 3:S08004, 2008.

[12] LHCb Collaboration. LHCb technical proposal. *CERN-LHCC-98-04*, 1998.

[13] ALICE Collaboration. Technical proposal for a large ion collider experiment at the CERN LHC. *CERN-LHCC-95-71*, 1995.

[14] R. Fruhwirth. Application of Kalman filtering to track and vertex fitting. *Nucl. Instrum. Meth.*, A262:444–450, 1987.

[15] CMS Collaboration. Track reconstruction in the CMS tracker. *CMS Note 2006/041*, 2006.

[16] CMS Collaboration. The CMS muon project : Technical Design Report. *CERN/LHCC 97-32*, 1997.

[17] M. Anderson et al. Review of clustering algorithm and energy corrections in ECAL. *CMS IN-2010/008*, 2008.

[18] CMS Collaboration. Photon reconstruction and identification at $\sqrt{s} = 7$ TeV. *CMS-PAS-EGM-10-004*, 2010.

[19] CMS Collaboration. Time Reconstruction and Performance of the CMS Electromagnetic Calorimeter. *JINST*, 5:T03011, 2010.

[20] CMS Collaboration. Particle-Flow Event Reconstruction in CMS and Performance for Jets, Taus, and MET. *CMS-PAS-EGM-10-003*, 2009.

[21] M. Cacciari, G. P. Salam, and G. Soyez. The anti-k_t jet clustering algorithm. *JHEP*, 4:63, 2008.

[22] CMS Collaboration. Missing transverse energy performance of the CMS detector. *JINST*, 06:9001, 2011.

[23] CMS Collaboration. Determination of Jet Energy Calibration and Transverse Momentum Resolution in CMS. *JINST*, 06:11002, 2011.

[24] W. N. Cottingham and D. A. Greenwood. *An introduction to standard model of particle physics*, volume Second Edition. Cambridge University Press, 2003.

[25] A. Pich. The Standard Model of Electroweak Interactions. *ArXiv:1201.0537[hep-ph]*, January 2012.

[26] S. Fredriksson. Preon Prophecies by the Standard Model. *ArXiv:hep-ph/0309213v2*, 2003.

[27] G. Arnison et al. Experimental observation of lepton pairs of invariant mass around 95 GeV/c^2 at the CERN SPS collider. *Phys. Lett. B*, 126:398410, 1983.

[28] G. Arnison et al. Experimental observation of isolated large transverse energy electrons with associated missing energy at $\sqrt{s} = 540$ GeV. *Phys. Lett. B*, 122:103–116, 1983.

[29] U. Baur and E. Berger. Probing the weak-boson sector in Zγ production at hadron colliders. *Phys. Rev. D*, 47:4889, 1993.

[30] T.Han U. Baur and J. Ohnemus. QCD corrections and anomalous couplings in Zγ production at hadron colliders. *Phys. Rev. D*, 57:2823, 1998.

[31] L3 Collaboration. Search for Anomalous $ZZ\gamma$ and $Z\gamma\gamma$ couplings in the process $e^+e^- \rightarrow Z\gamma$ at LEP. *Phys. Lett. B*, 489:55–64, 2000.

[32] CMS Collaboration. Measurement of inclusive $W\gamma$ and $Z\gamma$ cross sections and limits on anomalous trilinear gauge boson couplings at 7 TeV. *CMS AN-10-279*, 2010.

[33] DELPHI Collaboration. Study of Triple-Gauge-Boson Couplings ZZZ, $ZZ\gamma$, $Z\gamma\gamma$ at LEP. *Eur. Phys. J. C*, 51:525–542, 2007.

[34] P. Achard et al. (L3 Collaboration). Study of $e^+e^- \rightarrow Z\gamma$ process at LEP and limits on triple neutral-gauge-boson couplings. *Phys. Lett. B*, 597:119–130, 2004.

[35] V. Abazov et al. $Z\gamma$ production and limits on anomalous $ZZ\gamma$ and $Z\gamma\gamma$ couplings in $p\bar{p}$ collisions at $\sqrt{s} = 1.96$ TeV. *Phys. Rev. D*, 85:052001, 2012.

[36] T. Aaltonen et al (CDF Collaboration). Limits on Anomalous Trilinear Gauge Couplings in $Z\gamma$ Events from the $p\bar{p}$ collisions at $\sqrt{s}$ =1.96 TeV. *Phys. Rev. Lett.*, 107:051802, 2011.

[37] CMS Collaboration. Measurement of Wγ and Zγ production in pp collisions $\sqrt{s} = 7$ TeV. *Phys. Lett. B*, 701:535–555, 2011.

[38] ATLAS Collaboration. Measurement of $W\gamma$ and $Z\gamma$ production cross sections in pp collisions at $\sqrt{s} = 7$ TeV and limits on anomalous triple gauge couplings with the ATLAS detector. *Phys. Lett. B*, 717:49–69, 2012.

[39] E. Meschi et al. Electron Reconstruction in the CMS Electromagnetic Calorimeter. *CMS AN 2001/034*, 2001.

[40] CMS Collaboration. Isolated Photon Reconstruction and Identification at $\sqrt{s} = 7$ TeV. *CERN Document Server*, 2010.

[41] CMS Collaboration. Measurement of Wγ and Zγ Cross Section and Limits on Anomalous Triple Gauge Couplings at $\sqrt{s} = 7$ TeV. *CMS EWK-11-009*, 2012.

[42] CMS Collaboration. Electromagnetic calorimeter commissioning and first results with 7 TeV data. *CMS Information Server*, 2, 2010.

[43] The CMS Collaboration. Electromagnetic calorimeter commissioning and first results with 7 TeV data. *CMS-PAS-EGM-10-012*, 2010.

[44] The CMS Collaboration. Data-Driven Determination of Beam Halo Contamination in Photon Candidates. *CMS AN-2010/115*, 2010.

[45] CMS Collaboration. Search for Gauge Mediated Supersymmertry Breaking Using Two Photons and Missing Transverse Energy. *CMS-AN-11-515*, 2012.

[46] J. Pumplin, D.R. Stump, J. Huston, H. Lai, P. Nadolsky, and W. Tung. New generation of parton distributions with uncertainties from global QCD analysis. *JHEP*, 07:012, 2002.

[47] Michiel Botje, Jon Butterworth, Amanda Cooper-Sarkar, Albert de Roeck, Joel Feltesse, et al. The PDF4LHC Working Group Interim Recommendations. arXiv:1101.0538[hep-ph], 2011.

[48] A.D. Martin, W.J. Stirling, R.S. Thorne, and G. Watt. Parton distributions for the LHC. *Eur. Phys. J.*, C63:189–285, 2009.

[49] CMS Collaboration. Isolated Photon Reconstruction and Identification at $\sqrt{s} = 7$ TeV. *CMS-PAS-EGM-10-006*, 2011.

[50] CMS Collaboration. Vertex reconstruction at the CMS experiment. *J. Phys. Conf. Ser.*, 110:092009, 2008.

[51] https://twiki.cern.ch/twiki/bin/view/CMS/Pileup_2011_Reweighting.

[52] CMS Collaboration. Electroweak Utilities for MC corrections and systematic evaluation. *CMS*, 2010.

[53] The CMS Collaboration. Jet Resolution Determination at $\sqrt{s}$ =7 TeV. *JME-10-009*, 2010.

[54] The CMS Collaboration. Absolute Calibration of the Luminosity Measurement at CMS: Winter 2012 Update. *SMP-12-008*, 2012.

[55] R. Ofierzynski. Neutral Triple and Quartic Gauge Couplings at LEP. *Nucl. Phys. B*, 109 Proceedings supplement:57–62, 2002.

[56] G. Cowan, K. Cranmer, E. Gross, O. Vitells. Asymptotic formulae for likelihood-based tests of new physics. *Eur.Phys.J.*, C71:1554, 2011.

[57] Moneta, Lorenzo and Belasco, Kevin and Cranmer, Kyle S. and Kreiss, S. and Lazzaro, Alfio and others. The RooStats Project. *PoS*, ACAT201:057, 2010.

[58] Yuri Gershtein, Frank Petriello, Seth Quackenbush, and Kathryn M. Zurek. Discovering hidden sectors with monophoton $Z^{'}$ searches. *Phys. Rev.*, D78:095002, 2008.

[59] Y. Bai, P. J. Fox, and R. Harnik. The Tevatron at the Frontier of Dark Matter Direct Detection. *JHEP*, 1012:048, 2010.

[60] The CMS Collaboration. Search for Dark Matter and Large Extra Dimension in Monojet Events in pp collisions at $\sqrt{s} = 7$ TeV. *EXO-11-059*, 2011.

Appendix A

Dark Matter Searches

The astronomical evidences indicate that dark matter (DM) makes up 25% of the mass-energy content in the universe. The strongest arguments come from studies of the rotational curves of spiral galaxies. Spiral galaxies are characterized by a central bulge and a disk of stars rotating together around an axis. To make a rotation curve, one needs to calculate the rotational velocity of the of stars along the length of a galaxy by measuring their Doppler shifts and then plot this quantity with respect to the distance away from the center. When studying other galaxies, it is invariably found that the stellar rotational velocity remains constant with increasing the distance away from the galactic center. This result is highly counterintutive since based on Newton's law of gravity, the rotational velocity should steadily decrease from stars further way from the galactic center. Basically, inner planets within the Solar System travel more quickly about the Sun than do the outer planets. One way to speed up the outer planets might be to add more mass to the solar system between the planets. By the same phenomenon the flat galactic rotational curve seems to suggest that each galaxy may be surrounded by significant amounts of DM. It has been postulated and has been accepted that the DM would have to be located in a massive roughly spherical halo surrounding each galaxy.

There are three types of DM searches: direct, indirect, and collider searches. Direct searches for a DM candidate (χ) (from Xenon, CDMAS experiments) look for evidence of elastic $\chi-$nucleon scattering in detectors that are usually kept deep underground to

reduce background interactions. Indirect searches (from ICE CUBE experiment) look for the cosmos for photons or neutrinos produced in $\chi\bar{\chi}$ annihilation's. Collider searches at the LHC, where DM $\chi\bar{\chi}$ pairs may be produced in high energy collisions. Studies of the $Z\gamma$ channel would be sensitive to new physics like DM production at the LHC [58] since DM particles are escaped undetected representing a large Missing transverse energy similar to Z decays to neutral leptons. $Z\gamma$ signal in this case acts as one of the irreducible background. The DM pair can be produced in the reaction $q\bar{q} \rightarrow \chi\bar{\chi}\gamma$, where the photon is radiated by one of the incoming quarks, which would look like an excess of $Z(\nu\bar{\nu})\gamma$ events.

The results in this analysis described here are interpreted in terms of recent theoretical work [59] has cast this process in terms of a massive mediate particle whose mass is greater than 100 GeV in the s-channel which is represented by equation A.2. This process is contracted into an effective theory with a contact interaction scale λ which depends on the mediator mass and its couplings with quarks. Furthermore, the effective operator can be chosen to be a vector or axial vector which leads to spin independent or spin dependent operators respectively. The contact interaction operators are written as :

$$\mathcal{O}_V = \frac{(\bar{\chi}\gamma_\mu\chi)(\bar{q}\gamma^\mu q)}{\Lambda^2} \text{ , vector, } s\text{-channel} \tag{A.1}$$

$$\mathcal{O}_A = \frac{(\bar{\chi}\gamma_\mu\gamma_5\chi)(\bar{q}\gamma^\mu\gamma_5 q)}{\Lambda^2}, \text{axial vector, } s\text{-channel} \tag{A.2}$$

The DM candidate is represented by χ, q is a SM quark field. The contact interaction scale Λ^{-2} is given by $g_\chi g_q M^{-2}$, where M is the mass of the SM-DM mediator and g_χ and g_q are its couplings to DM and quarks, respectively. These effective operators are built with the assumption that χ is a Dirac fermion. If χ is a Dirac fermion, both SI and SD interactions will contribute to $\chi\bar{\chi}$ production at colliders.

The pair production of DM is simulated with MADGRAPH 4 where the hard initial state radiation of the photon has been included in the matrix-element level. The value of λ is to be 10 TeV during the generation and production cross section is assumed to scale with $1/\lambda^4$.

The good agreement between the signal sample and the SM prediction is used to set limits on the DM production cross sections. The limits on DM production are set as a function of the DM candidate mass, M_χ, for the scenarios with SI and SD interaction terms [5]. These limits are converted into lower limits on the cutoff scale Λ, which are used to also derive upper limits on the $\chi-$nucleon cross sections using equation A.3.

Dark Matter Mass [GeV]	90% CL Upper Limits Vector σ [fb]	Vector Λ [GeV]	Axial-Vector σ [fb]	Axial-Vector Λ [GeV]
1	14.3 (14.7)	572 (568)	14.9 (15.4)	565 (561)
10	14.3 (14.7)	571 (567)	14.1 (14.5)	573 (569)
100	15.4 (15.3)	558 (558)	13.9 (14.3)	554 (550)
200	14.3 (14.7)	549 (545)	14.0 (14.5)	508 (504)
500	13.6 (14.0)	442 (439)	13.7 (14.1)	358 (356)
1000	14.1 (14.5)	246 (244)	13.9 (14.3)	172 (171)

Table A.1: *Observed (expected) 90% CL upper limits on the DM production cross section and 90% CL lower limits on the cutoff scale Λ for the vector and axial-vector operators as a function of the DM matter mass M_χ.*

$$\sigma_{\mathrm{SI}} = \frac{9}{\pi}\left(\frac{\mu}{\Lambda^2}\right)^2 \qquad \text{and} \qquad \sigma_{\mathrm{SD}} = \frac{0.33}{\pi}\left(\frac{\mu}{\Lambda^2}\right)^2 \tag{A.3}$$

where σ_{SI} and σ_{SD} correspond to DM nucleon scattering cross section for SI and SD interaction, respectively while μ is the reduced mass which is represented in terms of the DM candidate mass m_{DM} and the mass of a proton m_{p}. This reduced mass is represented as equation A.4:

$$\mu = \frac{m_{\mathrm{DM}} m_{\mathrm{p}}}{m_{\mathrm{DM}} + m_{\mathrm{p}}} \tag{A.4}$$

By substituting in the upper limits for the interaction parameter Λ, the relationship as mentioned in equation A.3 produces lower limits on the $\chi-$nucleon cross section, which allows comparisons to be drawn between the CMS results and direct detection experiments. The results presented here are valid for mediator masses larger than the limits on Λ, assuming unity for the couplings g_χ and g_q. The CMS monophoton limits are displayed in

Figure A.1 [60] as a function of the DM candidate mass, along with the results from several contemporary experiments.

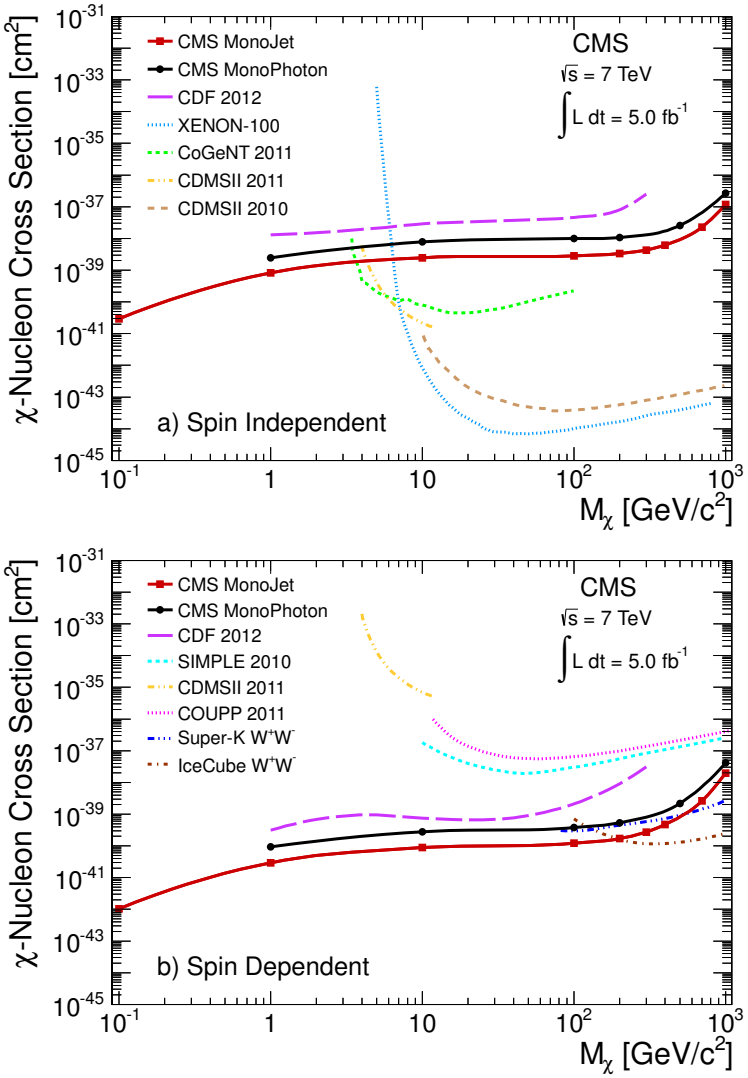

Figure A.1: *The 90% upper limits on the $\chi-$nucleon cross section as a function of M_χ for spin-independent (top) and spin-dependent (bottom) scattering.*

Figure A.1 shows that the most sensitive upper limits for spin-dependent $\chi-$nucleon scattering for χ masses between 1 and 100 GeV. For the spin-dependent case, the best limit for the low mass DM has been achieved below 3.5 GeV which is a region as yet unexplored by the direct detection experiments.

Appendix B

Error estimation

B.1 $W(e\nu)$ error estimation

$$N_{\text{est}} = \frac{1-\epsilon}{\epsilon} \times N_{\text{Wdata}} \tag{B.1}$$

In the equation B.1 there are two variables both of which have uncertainties associated with them $\epsilon \pm \Delta\epsilon$ and $N_{\text{data}} \pm \Delta N_{\text{data}}$. Hence, the uncertainties for W(eν) estimation after scaling with $(1-\epsilon)/\epsilon$ to the one obtained from data N_{Wdata} is given as:

$$\Delta N_{\text{est}} = \sqrt{\left(\frac{1-\epsilon}{\epsilon} \times \Delta N_{\text{Wdata}}\right)^2 + \left(-\Delta\epsilon\left(\frac{1}{\epsilon} + \frac{1-\epsilon}{\epsilon^2}\right) \times N_{\text{Wdata}}\right)^2} \tag{B.2}$$

B.2 Error estimation in measured cross section of $Z\gamma \to \nu\bar{\nu}\gamma$

The cross section is calculated using the formula given by:

$$\sigma = \frac{N-B}{A \times \epsilon \times \text{L}} \tag{B.3}$$

where σ is the cross section, N is the number of observed events in the signal region, B is the expected background in the signal region, A is the geometrical and kinematical acceptance for the signal, ϵ is the event selection efficiency and L is the integrated luminosity. The uncertainty on this cross section is given by:

$$\left(\frac{\Delta\sigma}{\sigma}\right)^2 = \left(\frac{\sqrt{N}}{N-B}\right)^2 + \left(\frac{\Delta B}{N-B}\right)^2 + \left(\frac{\Delta(A\times\epsilon)}{A\times\epsilon}\right)^2 + \left(\frac{\Delta\text{L}}{\text{L}}\right)^2 \tag{B.4}$$